


12-2018

Growth and Behaviors of InN/GaN Multiple Quantum Wells by Plasma-Assisted Molecular Beam Epitaxy

Chen Li

University of Arkansas, Fayetteville

Follow this and additional works at: <https://scholarworks.uark.edu/etd>

 Part of the [Electromagnetics and Photonics Commons](#), [Electronic Devices and Semiconductor Manufacturing Commons](#), and the [Semiconductor and Optical Materials Commons](#)

Recommended Citation

Li, Chen, "Growth and Behaviors of InN/GaN Multiple Quantum Wells by Plasma-Assisted Molecular Beam Epitaxy" (2018). *Theses and Dissertations*. 3115.
<https://scholarworks.uark.edu/etd/3115>

This Dissertation is brought to you for free and open access by ScholarWorks@UARK. It has been accepted for inclusion in Theses and Dissertations by an authorized administrator of ScholarWorks@UARK. For more information, please contact scholar@uark.edu, ccmiddle@uark.edu.

Growth and Behaviors of InN/GaN Multiple Quantum Wells by Plasma-Assisted Molecular
Beam Epitaxy

A dissertation submitted in partial fulfillment
of the requirements for the degree of
Doctor of Philosophy in Microelectronics-Photonics

by

Chen Li

University of Electronic Science and Technology of China
Bachelor of Engineering in Electronic Science and Technology, 2005
University of Electronic Science and Technology of China
Master of Engineering in Optics Engineering, 2008

December 2018
University of Arkansas

This dissertation is approved for recommendation to the Graduate Council.

Gregory J. Salamo, Ph.D.
Dissertation Director

Morgan Ware, Ph.D.
Committee Member

Shui-Qing Yu, Ph.D.
Committee Member

Laurent Bellaiche, Ph.D.
Committee Member

Rick L. Wise, Ph.D.
Ex-Officio Member

The following signatories attest that all software used in this dissertation was legally licensed for use by Mr. Chen Li for research purposes and publication.

Mr. Chen Li, Student

Dr. Gregory J. Salamo, Dissertation Director

This dissertation was submitted to <http://www.turnitin.com> for plagiarism review by the TurnItIn company's software. The signatories have examined the report on this dissertation that was returned by TurnItIn and attest that, in their opinion, the items highlighted by the software are incidental to common usage and are not plagiarized material.

Dr. Rick L. Wise, Program director

Dr. Gregory J. Salamo, Dissertation Director

Abstract

Fully realizing the potential of InGaN semiconductors requires high quality materials with arbitrary In-content. To this date the growth of In-rich InGaN films is still challenging since it suffers from the low growth temperatures and many detrimental alloying problems. InN/GaN multiple quantum wells (MQWs) and superlattices (SLs) are expected to be promising alternatives to random InGaN alloys since in principle they can achieve the equivalent band gap of InGaN random alloys with arbitrarily high In-content and at the same time bypass many growth difficulties.

This dissertation focuses on studying the growth mechanisms, structural properties and energy structures of InN/GaN MQWs. Molecular beam epitaxy (MBE) growth of InN/GaN MQWs were carried out at 550 °C and 680 °C, which are close to the low and high ends of the allowed growth temperature window. Reflection high energy electron diffraction (RHEED) was demonstrated to be a valuable tool for understanding the MQW growth. By associating the RHEED intensity transient features with surface atomic processes such as the adsorption/desorption of metal species, the growth process was successfully monitored in situ. Also, at the high growth temperature, RHEED was successfully used to study the adsorption/desorption kinetics of indium surface coverage to gain knowledge of how to control InN deposition. The MQW growth at 680 °C show that indium surface coverage over 2 MLs before GaN capping is a key factor for consistent quantum well formation. The consistent PL emissions at ~375 nm were attributed to the insertion of 1-ML thick QWs. At 550 °C, both PL emission and QW thickness showed a self-regulating behavior. The redshift of PL emissions with the InN deposition saturated at ~423 nm while the QW apparent thickness were no more than 2 MLs. The residual indium accumulation identified by RHEED suggests that QWs are generally InGaN layers instead of coherent InN layers,

which is supported by **k.p** calculations. Finally, a growth mechanism was proposed to explain the preservation, structural and optical properties of the quantum wells.

Acknowledgements

First and foremost, I would like to thank my Ph.D. advisor, Dr. Salamo, for accepting me in his amazing research group and supporting my study for all these years. He is a knowledgeable scientist, great team leader, and fantastic educator. Working with him made the long hard Ph.D. journey much less painful. His passion for science and professional attitude set a high bar for being a scientist and inspired me in many ways.

I would like to thank Dr. Morgan Ware for being a great mentor and friend. He taught me how to play with the nitride MBE machine. This dissertation would be impossible without his help and encouragement. I am always impressed by how he handles instruments with confidence. I am also impressed by his willingness to help and his patience to listen.

I am deeply grateful to my comrade, Dr. Yuriy Mazur. He is the kind of person who makes things happen, in a lot of cases by pushing others. Without him this dissertation would take much longer to finish. I would also like to thank him for caring about my future career.

I would like to thank Dr. Andrian Kuchuk for the XRD measurements of my samples, his “secret list” of useful publications, and many fruitful discussions.

I would like to thank Yurii for his quality work of PL and TEM investigations on my samples. I would also like to thank him for the discussion of \mathbf{k}, \mathbf{p} calculations.

I would like to thank Dr. Zhiming Wang for his trust and mentoring. He introduced me into Dr. Salamo’s group and guided me into research quickly. I would like to thank Dr. Zhaoquan Zeng for taking care of me in my early years of Ph.D. study. He is a good friend and mentor of me. I would like to thank Dr. Vasyl Kunets for his coaching in the electrical characterization lab. I would like to thank Dr. Mourad Benamara for his technical support of TEM measurements and also for keeping the coffee club running. I would like to thank David Monk for keeping the MBE lab

running smoothly.

I like to thank Rick, Ken, Renee for running the amazing graduate program, MicroEP.

I would like to thank the current and former colleagues in our research groups, Tim, Xian, Yang, Thomas, Paul, Sabina, Pijush, Satish, Paul, Rob, Collin, Mike, Yusuke, Chris, Vitaliy, Jiang, Mohammad, Qigeng, Najala, Samir, Hryhorii, and Samir for their help during my Ph.D. study.

This work was supported by the USA National Science Foundation Engineering Research Center for Power Optimization of Electro Thermal Systems (POETS) with cooperative agreement EEC-1449548.

Finally, my deepest thanks go to my family. I would like to thank my parents for their unconditional love and support. I would like to thank my wife, a beautiful woman who has always been loving me and supporting me. She brought my sons Matthew and Isaac to this world and makes our tiny rented apartment look like a home through tireless work. This work could not have been done without you.

Table of contents

Chapter 1: Introduction	1
1.1. Background	1
1.2. Basic material properties.....	2
1.3. The historical development of nitride materials.....	8
1.4. Growth of InN and InGaN	13
1.5. The InN/GaN quantum wells	19
Chapter 2: Research methodology	23
2.1. Background of MBE	23
2.2. MBE system.....	24
2.3. RHEED fundamentals	27
2.4. III-nitride growth by PAMBE	30
2.5. The eight-band k.p method	35
2.5.1. Bulk materials	35
2.5.2. Heterostructures	39
Chapter 3: InN/GaN MQW growth at 680 °C.....	44
3.1. Introduction	44
3.2. Growth	46
3.3. The existence of dynamically stable indium coverage	47
3.4. Quantitative determination of the dynamically stable coverage	49
3.5. Sample growth	57
3.6. Photoluminescence.....	63

3.7. X-ray diffraction.....	64
3.8. Discussion	65
3.9. Summary	69
Chapter 4: InN/GaN MQW growth at 550 °C.....	70
4.1. Introduction	70
4.2. Growth	71
4.3. RHEED intensity.....	72
4.4. RHEED pattern	76
4.5. Photoluminescence.....	84
4.6. X-ray diffraction.....	86
4.7. Transmission electron microscopy.....	87
4.8. Theoretical calculation of band structures	87
4.9. Discussions.....	91
4.10. Summary	97
Chapter 5: Conclusions and future work	98
5.1. Conclusions	98
5.2. Future work	100
References	101
Appendix A: Parameters for the eight-band k.p method.....	119
Appendix B: Description of research for popular publication.....	122
Appendix C: Executive summary of newly created intellectual property	124

Appendix D: Potential patent and commercialization aspects of listed intellectual property items.....	125
Appendix E: Broader impact of research.....	126
Appendix F: Microsoft project for Ph.D. microEP degree plan	127
Appendix G: Identification of all software used in research and dissertation generation	130
Appendix H: All publications published, submitted, and planned	131
Appendix I: Publishing agreements/permissions.....	134

List of figures

Figure 1-1. The crystal structure of wurtzite GaN.....	3
Figure 1-2. Band gap (a) and polarization (b) of nitride materials. The piezoelectric polarization, $P_{pz,z}$, in (b) is calculated assuming the materials are strained on GaN.	5
Figure 1-3. Dipole representation of the (a) 2D and (b) 3D bound charges.	6
Figure 1-4. GaN growth regimes (a); the AFM images of surface morphology for samples grown in Ga-stable, intermediate, and N-stable regimes (b)-(d).	12
Figure 1-5. Dislocations in GaN revealed by H_3PO_4 etching at 200 °C. (a) and (b) are AFM images of a depth profile and a phase contrast profile, respectively.	15
Figure 1-6. Maximum In content of InGaN films as a function of MBE growth temperature.....	16
Figure 1-7. Theoretical spinodal and binodal curves of fully relaxed InGaN materials (a); theoretical spinodal curves with different strain states (b).	17
Figure 1-8. TEM images of spontaneously formed superlattice during InGaN growth in ref. 134.....	18
Figure 1-9. The conduction and valence band edge profiles of a 1-ML-InN/9-ML-GaN superlattice.	20
Figure 2-1. Unit conversions in vacuum technology.	25
Figure 2-2. Schematic of nitride MBE system.....	26
Figure 2-3. Electron beams scattered by a 2D lattice. (a) Ewald construction of 2D scattering; (b) the RHEED pattern on the phosphor screen corresponding to (a).	28
Figure 2-4. Layer-by-layer (a) and step-flow (c) growth mode and their RHEED intensity evolution during growth [(b) and (d)].	30
Figure 2-5. N diffusion channel between a GaN(0001) substrate and an indium adlayer. The diffusion path is indicated by yellow arrows. The blue, gray and red colors denote nitrogen, gallium and indium atoms respectively. The inset is the side view of the GaN substrate and In adlayer.....	31
Figure 2-6. RHEED intensity evolution of Ga-rich GaN growth (a); Ga cell temperature as a function of droplets desorption time $t_3 - t_2$ (b).	33
Figure 2-7. GaN growth diagram.....	35

Figure 3-1. The 1×1 (a) and $(\sqrt{3} \times \sqrt{3})R30^\circ$ (b) RHEED patterns viewed along the $[1 \bar{1}00]$ azimuth.....	46
Figure 3-2. The schematics of the $(\sqrt{3} \times \sqrt{3})R30^\circ$ (a) and the $(2\sqrt{3} \times 2\sqrt{3})R30^\circ$ (b) surface reconstructions. The unit cells are indicated by blue lines; the Bravais lattice of GaN(0001) planes is indicated by the black dots; and the arrangement of In atoms is labeled by red circles.	46
Figure 3-3. (a) The full RHEED intensity evolution corresponding to deposition time of 100 s on the $(\sqrt{3} \times \sqrt{3})R30^\circ$ surface; RHEED intensity transients after In deposition with various deposition times on the (b) GaN 1×1 surface and (c) $(\sqrt{3} \times \sqrt{3})R30^\circ$ surface. The substrate temperature was 710°C and the In flux was 0.28 ML/s. The dotted line indicates 80% of fully recovered intensity.	48
Figure 3-4. Schematic of the decay of indium surface coverage due to desorption.	49
Figure 3-5. The RHEED intensity recorded during the desorption of dynamically stable indium coverages stabilized under various fluxes on a (a) GaN 1×1 surface and (b) $(\sqrt{3} \times \sqrt{3})R30^\circ$ surface. The desorption times of flux windows with nearly constant desorption time are labeled by black dotted lines.....	52
Figure 3-6. (a) Indium surface coverage at 680°C as a function of impinging indium flux on a GaN 1×1 surface and $(\sqrt{3} \times \sqrt{3})R30^\circ$ surface. (b) The decay of indium surface coverage due to desorption on a GaN 1×1 surface and $(\sqrt{3} \times \sqrt{3})R30^\circ$ surface.....	53
Figure 3-7. (a) Normalized specular spot/streak RHEED intensity transients caused by the desorption of two In adlayers on a GaN 1×1 surface at 650°C , 680°C and 700°C . (b) Normalized RHEED intensity transients of 1/3 order streak caused by the desorption of two In adlayers and the decay of the $(\sqrt{3} \times \sqrt{3})R30^\circ$ reconstruction at 650°C , 680°C and 700°C . The Arrhenius plots of the inverse desorption times $1/t_d$ of indium adlayers and the inverse of decaying life time $1/\tau$ of the $(\sqrt{3} \times \sqrt{3})R30^\circ$ reconstruction are plotted in the insets in (a) and (b).	56
Figure 3-8. (a) The shutter sequence of one InN/GaN growth cycle. The transition of RHEED patterns during different growth stages are labeled on the top. (b) Sample structure of MQWs grown at 680°C	58
Figure 3-9. Specular spot RHEED intensity evolutions of the first few InN/GaN growth cycles viewed along the $[1 \bar{1}00]$ azimuth at 680°C . The shutter events of opening In shutter, opening Ga shutter and closing Ga shutter in the first growth cycle are labeled as A, B and C.	60
Figure 3-10. Magnified view of the (a) InN deposition stage and (b) GaN capping stage of the RHEED intensity evolutions in Figure 3-9. In (a), all the curves are aligned according to the In shutter opening time (A); in (b) all curves are aligned according to the Ga shutter opening time (B). The definition of shutter events are the same as that in Figure 3-9.....	61

Figure 3-11. Normalized PL intensity of InN/GaN MQWs measured at 10 K.	63
Figure 3-12. ω - 2θ scans of the (0002) reflection of samples II, IV and V.	65
Figure 3-13. The $(2\sqrt{3} \times 2\sqrt{3})R30^\circ$ reconstruction proposed in ref. 188.	67
Figure 4-1. InN/GaN quantum wells from ref. 150 with apparent thickness of 1 ML (a) and 2 MLs (b). The top images are noise averaged high resolution scanning transmission electron microscopy (HRSTEM) images. The bottom images are profiles of indium content.	71
Figure 4-2. (a) Shutter sequence for one InN/GaN bilayer growth. (b) Sample structure.....	72
Figure 4-3. (a) RHEED intensity evolution of 1-ML-InN/GaN MQW growth; the inset is the zoomed view of the hollow rectangular area. (b) Zoomed view of RHEED intensity evolution of one InN/GaN bilayer growth cycle (shaded area in (a)). The gray and red dotted lines in (a) and (b) are eye-guides for the evolution of level A and level B.	73
Figure 4-4. RHEED intensity evolution of n-ML-InN/GaN MQWs growth for n = 0.5 and n = 3. The gray and red dotted lines are eye-guides for the evolution of level A and level B.....	76
Figure 4-5. RHEED patterns viewed along $[1\bar{1}20]$ azimuth during different InN/GaN growth cycles when level B is reached. The positions of side streaks are labeled by white arrows. The top, middle, and bottom row correspond to nominal InN depositions of 0.5, 1, and 2 MLs.	78
Figure 4-6. The “1+1/6” RHEED pattern (a) and LEED pattern (b) caused by Ga adsorption on a GaN(0001) surface at low temperature ($< 350^\circ\text{C}$). The “1+1/6” LEED pattern obtained by annealing a InGaN sample under nitrogen plasma at 710°C (c).	79
Figure 4-7. The schematic of double scattering process between 2D lattices. (side view)	80
Figure 4-8. (a) and (d): GaN 1×1 RHEED pattern viewed along $[1\bar{1}20]$ and $[1\bar{1}00]$ azimuth after high temperature GaN buffer growth. (b) and (e): The “1+1/6” RHEED pattern obtained at 520°C viewed along $[1\bar{1}20]$ and $[1\bar{1}00]$ azimuth with identifiable streaks not belonging to the 1×1 pattern labeled by white arrows. (c) and (f): Simulated electron beam maximas caused by GaN 1×1 surface (dots), and by double scattering between the GaN 1×1 surface and an overlayer with the same in-plane symmetry as GaN and a lattice constant 1/6 larger (crosses). The blue arrows in (c) and (f) correspond to the white arrows in (b) and (e).	82
Figure 4-9. (a) Summary of PL emission peaks of MQWs with different combinations of nominal InN thickness (n-ML) and numbers of QWs (m). (b) Representative PL curves for samples with various nominal thickness (n-ML).	85
Figure 4-10. ω - 2θ scans of the (0002) reflection of samples grown at 550°C with nominal thickness of n-ML and total QW number (m) of 7.	86
Figure 4-11. Cross-sectional high resolution TEM images of MQWs with nominal InN	

deposition of (a) 1 ML and (b) 3 MLs.	87
Figure 4-12. The band gap of 1-ML and 2-ML thick InGaN/GaN QWs as a function of In content.	88
Figure 4-13. The energy dispersion of 1-ML (a) and 2-ML (b) thick $\text{In}_{0.43}\text{Ga}_{0.57}\text{N}/\text{GaN}$ QWs. ...	89
Figure 4-14. The comparison between the strained and unstrained valence band structure of $\text{In}_{0.43}\text{Ga}_{0.57}\text{N}$ bulk.	89
Figure 4-15. The probability densities of band edge states for 1-ML thick $\text{In}_{0.43}\text{Ga}_{0.57}\text{N}/\text{GaN}$ QWs. (a) and (b) are the two degenerate conduction band edge states. (c) and (d) are the two degenerate valence band edge states.	90
Figure 4-16. The probability densities of band edge states for 2-ML thick $\text{In}_{0.43}\text{Ga}_{0.57}\text{N}/\text{GaN}$ QWs. (a) and (b) are the two degenerate conduction band edge states. (c) and (d) are the two degenerate valence band edge states.	91
Figure 4-17. Schematic of the formation of the first two monolayers of InGaN film.	92

List of tables

Table 1-1. Key material properties for major semiconductors.	2
Table 1-2. Bowing parameters for band gap and spontaneous polarization.	4
Table 1-3. Polarization related parameters.	4
Table 3-1. Summary of growth parameters of InN/GaN MQWs.	59

List of published papers used in this dissertation

Part of chapter 3 was originally published as

C. Li, Y. Maidaniuk, A. V. Kuchuk, S. Shetty, P. Ghosh, T. P. White, T. A. Morgan, X. Hu, Y. Wu, M. E. Ware, Y. I. Mazur, and G. J. Salamo, “*Kinetically controlled indium surface coverage effects on PAMBE-growth of InN/GaN(0001) quantum well structures*,” J. Appl. Phys., 123, 195302, (2018)

Chapter 1: Introduction

1.1. Background

III-nitride semiconductors, including the binary GaN, AlN, and InN and their alloys, have been under intensive investigation for more than three decades and are still gaining more and more research attention. One of the primary reasons that III-nitrides are so attractive is their exceptionally wide direct band gap coverage. The band gap values of 6.2 eV (AlN), 3.4 eV (GaN), and 0.64 eV (InN)¹ indicate an engineering possibility of optoelectronic devices working in a continuous electromagnetic spectral range from near infrared, through the whole visible range, to deep ultraviolet. After major technological breakthroughs in the early 1990s, especially the high quality InGaN film growth² and the identification of hole compensation mechanism,^{3–5} InGaN-based blue light emitting diodes⁶ (LEDs) and laser diodes⁷ (LDs) were soon demonstrated, and quickly lead to a huge global market. It should be noted that these blue light emitters had long been desired by industry because they could be used to produce white light sources if coupled with luminescent phosphor materials. Today, InGaN based light emitters are used in enormous applications in our everyday life. For example, InGaN-based white LEDs are now widely used in high efficiency car lights and display panels of TVs and cell phones as white backlight sources. Also, InGaN based LDs are used in high definition DVD players.

Compared to conventional semiconductors such as silicon and III-arsenide materials, the large band gap, high breakdown field, high electron saturation velocity, and large current density make III-nitrides good candidates for high power, high frequency applications such as RF power amplifiers.⁸ These applications are often based on the high electron mobility transistor (HEMT) structure, which typically involve an AlGaN/GaN^{8,9} or InAlN/GaN¹⁰ heterostructure that can be conveniently grown using both MBE and MOCVD. This should be compared to SiC, another

promising wide band gap material for high power and high frequency applications, which can only be fabricated into the metal semiconductor field effect transistors (MESFETs) and thus cannot benefit from the high electron density and velocity brought by the HEMT structure.^{8,11,12}

Table 1-1. Key material properties for major semiconductors.^{8,13–18}

	GaN	AlN	InN	SiC (4H)	SiC (6H)	GaAs	Si
Band gap (eV)	3.39	6.2	0.64	3.26	3.03	1.42	1.12
Electron mobility (10³ cm²/(V·s))	1.2	1.1	3	0.7	0.37	8.5	1.35
Breakdown field (MV/cm)	3.3	11.7	1.0	3.0	2.4	0.4	0.3
Saturated electron drift velocity (10⁷ cm/s)	2.5	1.8	2.5	2.0	2.0	1.0	1.0
Thermal conductivity (W/(cm·K))	1.3	2.7	1.8	3.7	3.87	0.43	1.5
Thermal expansion coefficient (10⁻⁶/ K)	5.59	4.2	3.8	3.7	4.3	5.73	2.6

Further, due to the small band gap of 1.12 eV, working in high temperature over 300 °C would lead to failure of silicon-based devices since excessive carriers would be thermally generated. The large band gap of 3.4 eV is expected to expand the working temperature of GaN-based devices up to 1000 °C.^{10,19} In addition, since nitride materials, especially GaN and AlGaIn, have good thermal stability, high chemical resistance and high radiation resistance, nitride-based devices are particularly suitable to be used in harsh environments, such as the environments often encountered in oil, automobile, and aerospace industries. The demonstrated devices include but are not limited to mechanical sensors,^{19,20} α -particle detectors,²¹ and Hall effect sensors.²²

1.2. Basic material properties

III-nitrides can be found in both the thermodynamically stable wurtzite phase (α -phase)

and metastable zinc-blende phase (β -phase). Since most of the III-nitride devices are based on wurtzite structure GaN, only the properties of wurtzite nitride materials are introduced in this section. As is shown in Figure 1-1, GaN in wurtzite structure is a periodic stacking of hexagonal close-packed Ga-N bilayers (space group $p6_3mc$). The lack of an inversion symmetry makes the two orientations of the c-planes essentially different. Depending on if the growth is along the $[0001]$ or $[000\bar{1}]$, the surfaces that the epilayers are grown on are conventionally referred as (0001) surface (Ga-face) or $(000\bar{1})$ surface (N-face). Also, the lack of an overall inversion center leads to a non-vanishing polarization field along the c direction even without an external electric field.

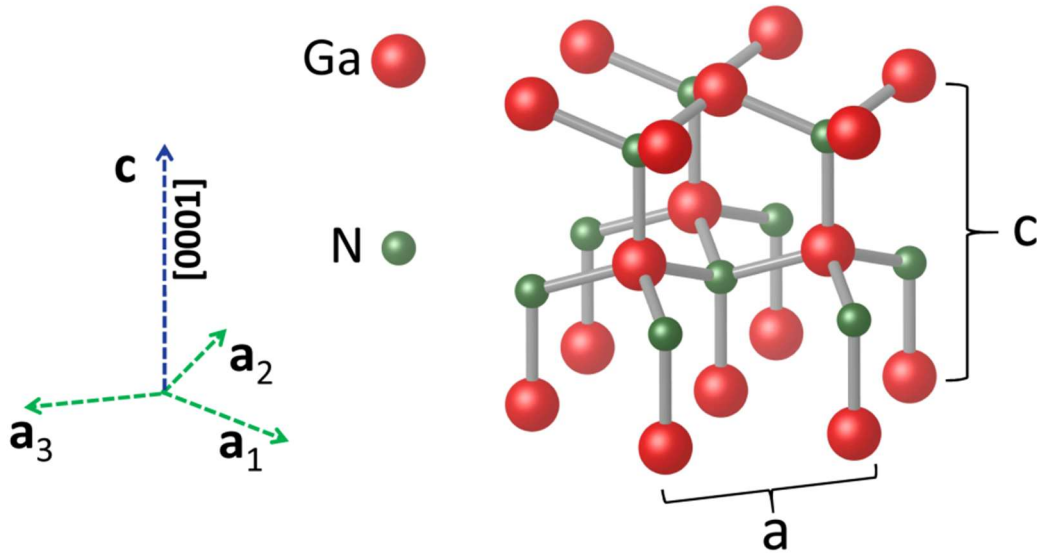


Figure 1-1. The crystal structure of wurtzite GaN.

The polarization of a crystal in its equilibrium shape is called the spontaneous polarization, \mathbf{P}_{sp} . When the crystal is strained an additional polarization component, the piezoelectric polarization, \mathbf{P}_{pz} , is generated.²³ So, the total polarization field, \mathbf{P} , is

$$\mathbf{P} = \mathbf{P}_{sp} + \mathbf{P}_{pz} \quad (\text{Equation 1.1})$$

In the case of small lattice deformation, the piezoelectric polarization along the [0001] direction (z-direction) can be related to the c-plane strain, $\varepsilon = (a - a_0) / a_0$, as^{24,25}

$$P_{pz,z} = 2\varepsilon(e_{31} - e_{33} \frac{C_{13}}{C_{33}}) \quad (\text{Equation 1.2})$$

where a and a_0 are the strained and equilibrium value of the c-plane lattice constants; C_{13} and C_{33} are elastic constants; and e_{31} and e_{33} are piezoelectric coefficients.²⁶ The polarization and band gap of III-nitride materials as a function of lattice constant are plotted in Figure 1-2, where the piezoelectric polarization is calculated assuming the material is strained on a GaN substrate. The bowing of material properties F , such as the polarization and band gap, are calculated as

$$F(A_x B_{1-x} N) = xF(A) + (1-x)F(B) - x(1-x)b \quad (\text{Equation 1.3})$$

where bowing parameters, b , are summarized in Table 1-2, and the polarization related parameters are listed in Table 1-3.

Table 1-2. Bowing parameters for band gap and spontaneous polarization.²⁷⁻²⁹

	AlGaN	InGaN	AlInN
Band gap (eV)	1.0	1.4	3.4
Spontaneous polarization (C/m²)	-0.0191	-0.0378	-0.0709

Table 1-3. Polarization related parameters.^{30,31}

	$P_{sp,z}$ (C/m ²)	e_{33} (C/m ²)	e_{31} (C/m ²)	C_{13} (GPa)	C_{33} (GPa)
AlN	-0.090	1.505	-0.533	100	390
GaN	-0.034	0.667	-0.338	110	390
InN	-0.042	0.815	-0.412	121	182

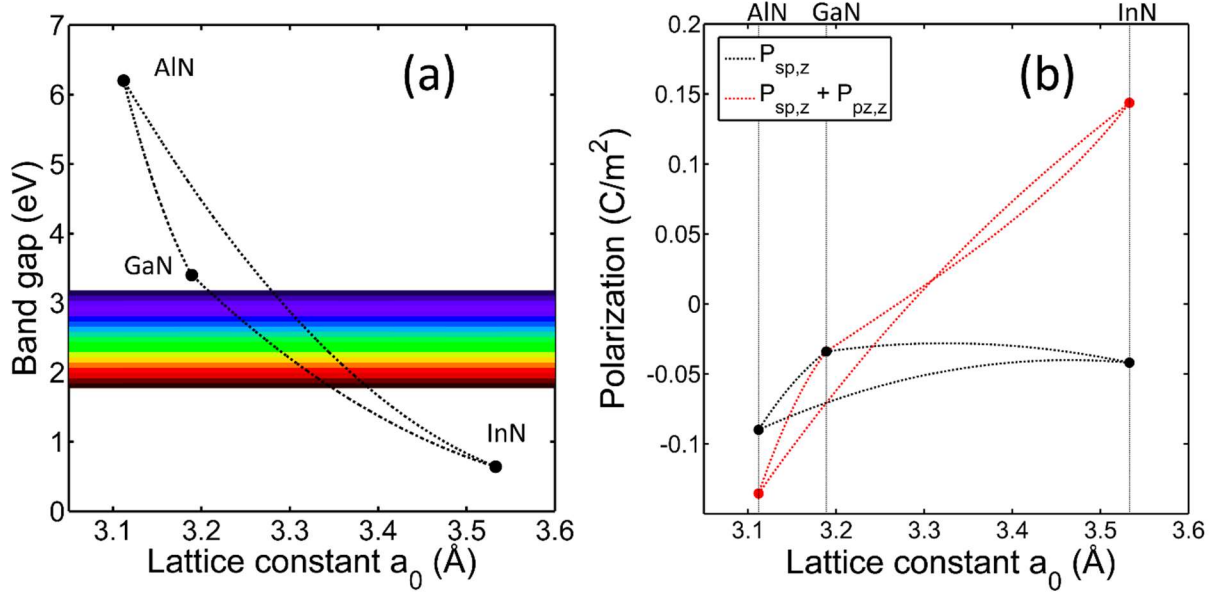


Figure 1-2. Band gap (a) and polarization (b) of nitride materials. The piezoelectric polarization, $P_{pz,z}$, in (b) is calculated assuming the materials are strained on GaN.

At the interfaces between epi-layers, the discontinuity of the polarization field gives rise to a 2D bound charge density, σ , given by

$$\sigma = (\mathbf{P}_1 - \mathbf{P}_2) \cdot \mathbf{n} \quad (\text{Equation 1.4})$$

where \mathbf{P}_1 and \mathbf{P}_2 represent the polarization field on different sides of an interface, and \mathbf{n} is the unit normal vector from side 1 to side 2. As shown in Figure 1-3, if the polarization is gradually changed, a bound charge density ρ in 3D space will be created according to Eq. 1.5

$$\rho = -\nabla \cdot \mathbf{P} \quad (\text{Equation 1.5})$$

The magnitude of both spontaneous and piezoelectric polarization in III-nitrides appeared to be very large³² as seen in Figure 1-2(b), which often gives a non-trivial influence to device performance. As an example, the quantum confined stark effects (QCSEs) are frequently presented in III-nitride light emitting devices.³³ A red shift of emission peak is observed for devices grown along the polar \mathbf{c} axis. This is understood as the charge bounded at the interfaces of the active

region, resulting from polarization discontinuity, cause a strong electrostatic field across the active region which in turn reduces the effective band gap. This phenomenon is commonly regarded as detrimental for light emitting devices since the electric field gives rise to a spatial separation of electron and hole wave functions and, therefore, reduces the possibility of radiative recombination.

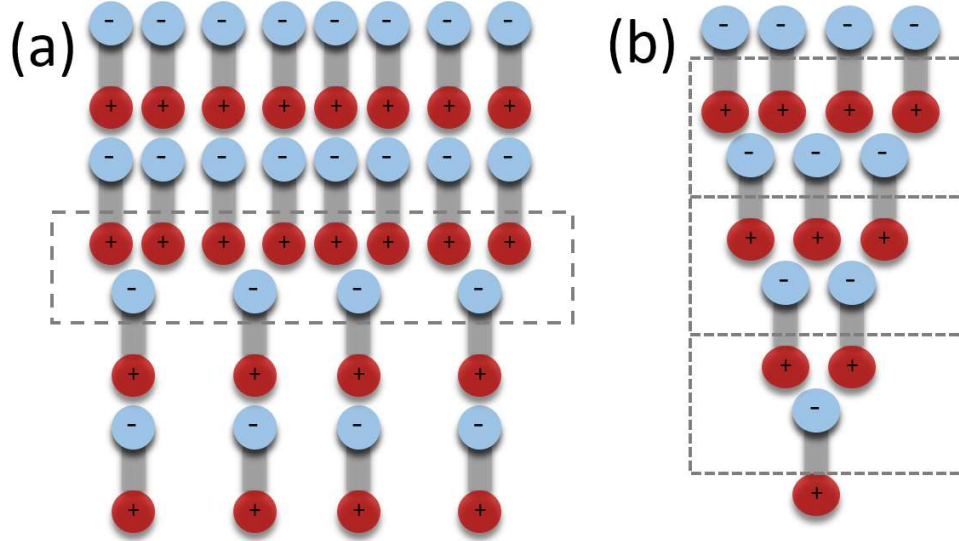


Figure 1-3. Dipole representation of the (a) 2D and (b) 3D bound charges.

Several works^{34–42} showed that, instead of the traditional “hydrogenic doping” which relies on thermal ionization of dopants, a “polarization doping” can be used for both n- and p- type doping. The trick is to create a gradient of the polarization field by grading the composition in an AlGa_N or InGa_N layer. The bound charges in 3D space then attract free carriers of the opposite sign. The polarization doping is in nature an electrical-field assisted, rather than a thermally activated, process. Thus, it is especially valuable to alleviate the difficulty of p-type doping, which suffers from the high dopant activation energy (~200 meV for Mg in GaN). J. Simon et al.⁴³ showed that polarization doped p-type layers can be used to improve electroluminescence of a UV LED. As a more recent example, Y. Enatsu et al.⁴² realized dopant free hole gases in compositionally graded InGa_N layers.

Different from the III-arsenide based HEMTs, for which a remote dopant reservoir is usually needed to provide electrons to the conductive channel, III-nitride HEMTs require no intentional doping. The polarization induced bound charges at the AlGa_N/Ga_N interface attract free carriers to form a highly mobile (typical mobility over 1000 cm²/(V·s)) two-dimensional electron gas (2DEG) with a 2D sheet electron density as high as 1×10^{13} cm⁻², where the surface states are believed to be the source of electrons.^{32,44} The combination of the high mobility, high electron density, and wide band gap gives nitride HEMTs a unique advantage for high power and high frequency electronics.

The inequivalence of the two surface orientations leads to very different physical and chemical properties between the Ga-face and N-face. The Ga-face can hold ~2.3 ML of Ga adlayers before droplet formation, while the N-face can only hold 1 ML.⁴⁵⁻⁴⁷ It is found that the N-face is more resistant to thermal decomposition,⁴⁸ so that the upper limit of the growth temperature window is higher for the N-face for both GaN⁴⁵ and InN⁴⁹. Due to the difference in chemical resistance,^{50,51} the high selectivity of KOH etching had been used to investigate the inversion domain of the Mg-doped Ga-face GaN samples.⁵² The impurity incorporation was also found to be dependent on surface polarities. For example, it has been found that, for the same Mg flux, the incorporated Mg concentration is about one order of magnitude higher in Ga-face GaN layers than that in N-face GaN layers.⁵³ Also, the most common n-type background dopant source, oxygen, is more easily incorporated in the N-face GaN,⁵⁴⁻⁵⁶ which is likely due to the difference in oxygen adsorption energy as is revealed by theoretical investigations.⁵⁷ The majority of HEMT devices were grown on the Ga-face mainly due to the superior crystal quality.^{45,46,58,59} Although hard to achieve high material quality, N-face HEMT devices have also attracted a lot of research interest because the flipped polarization allows device design that contains a natural back potential

barrier which is helpful to suppress current leakage, and also enables low contact resistance which is important for device scaling.^{60,61}

1.3. The historical development of nitride materials

The first epitaxial growth of GaN was attempted in 1969⁶² GaN crystals were grown on sapphire substrates using hydride vapor phase epitaxy (HVPE) by H. Maruska and J. Tietjen at RCA laboratories. The obtained crystals were determined to be in single wurtzite phase with a band gap of 3.39 eV. However, the background electron density was over 10^{19} cm^{-3} , reflecting the poor crystal quality. This ground-breaking work laid solid experimental foundation for future development of GaN-based technology.

In the following years, all efforts aiming to obtain p-type conductivity failed, which is not surprising considering that the background electron density was still high. The potential p-type dopants under investigation during this period of time included Ge, Mg, Zn, and Cd.^{62–66} Although p-type conductivity was not obtainable, these dopants appeared to compensate the native electrons effectively and semi-insulating GaN films were realized.⁶⁷ LEDs working in the green to violet spectral range can be fabricated based on these insulating layers.^{68–70} However, these devices typically use a metal-insulator-semiconductor (MIS) structure and the electroluminescence relies on the impact ionization of luminescence centers which require high voltage operation.⁷¹ Thus, more effective p-n junction based LEDs were still desirable.

In the 1980s, because of the persistent difficulties in achieving p-type conductivity and poor crystal quality, much research attention was moved to ZnSe, another potential material for blue LEDs. ZnSe was considered to be superior to GaN because low dislocation density less than 10^3 cm^{-2} could be achieved if grown on a GaAs substrate, which is strikingly lower than that of $\sim 10^9 \text{ cm}^{-2}$ for GaN grown on sapphire.⁷² On the other hand, GaN growth was explored using new

growth technologies including MBE⁷³ and MOCVD.⁷⁴ What is worth mentioning is that a AlN buffer inserted before GaN growth was found to greatly improve the quality of GaN films for both MBE and MOVCD.^{73,74} Using this technique, A. Amano et al. demonstrated the first crack-free GaN film with optically flat surface.⁷⁴ In later 1980s, S. Nakamura brought the GaN film quality to a higher level using a modified MOCVD system,^{75,76} the “two-flow MOCVD” which was named by himself. As an example, in a report from 1991,⁷⁶ the unintentional doped GaN film showed a room temperature background electron density of only $4 \times 10^{16} \text{ cm}^{-3}$, while the mobility was increased to $\sim 600 \text{ cm}^2/(\text{V}\cdot\text{s})$. In fact, later the two-flow MOCVD played a key role in developing and commercializing many GaN-based devices.

More importantly, the haunting p-type doping problem was finally solved in the early 1990s. H. Amano et al. discovered that the highly resistive as-grown Mg doped GaN film can be turned into a conductive p-type layer after being treated by low-energy electron beam irradiation (LEEBI). Employing this technique, the first p-n junction LED showing near band edge emission was demonstrated.³ However, the exact reason why the p-type conductivity can be triggered by LEEBI was not clear until 1992.^{4,5} S. Nakamura et al. developed a new method to activate the p-type conductivity by annealing the as-grown samples in N_2 ambient over 700°C .⁴ It was further discovered that the already activated p-type films could be passivated to be highly resistive if annealed in a NH_3 environment.⁵ Since the NH_3 dissociates at high temperatures, S. Nakamura et al. concluded that the hole compensation was due to the formation of Mg-H complexes. Because the thermal annealing approach can be implemented in the growth chamber and is not affected by the film thickness (LEEBI has limited electron penetration depth and is ex situ to growth), it became the standard procedure in industry for p-type conductivity activation.

Meanwhile, the growth of the InGaN alloy was also under investigation. The band gap of

the InGaN system covers the whole technologically important visible spectral range. They form the type I quantum well band alignment with GaN, similar to the GaAs/AlGaAs system based on which many new physics and device concepts have been realized. In 1992, S. Nakamura et al. showed MOCVD-grown InGaN samples with bright room temperature emission under PL measurement due to band-to-band transition,² which was in sharp contrast to all previously reported InGaN films whose optical properties were dominated by defects.

To this point, the obstacles towards fabricating high efficiency LEDs and LDs were cleared. High performance LEDs⁷⁷ and LDs^{7,78} employing optimized heterostructure design were demonstrated in 1990s and since then the research and industrialization of nitride-based optoelectronic devices was quickly revolutionized.

It is worth mentioning that the excellent light emitting performance of InGaN-based LEDs was initially unexpected considering the high dislocation density on the order of 10^9 cm^{-2} . It seems that the dislocations only reduce the effective volume of the InGaN film but do not play a significant role in carrier recombination. Although the reason for this insensitivity is still under debate, a common belief is that quantum-dot-like localized states caused by indium content fluctuation capture injected carriers effectively so that the possibility of defect-assisted nonradiative recombination is reduced.

MOCVD played a leading role in the development of III-nitride material and devices. On the other hand, due to many inherent advantages, especially the accurate control of the thickness and composition of heterostructures, much research efforts were also devoted to MBE. Because N_2 molecules are extremely stable, different techniques were adopted to provide active nitrogen species for MBE growth of III-nitride materials. Despite the early demonstration⁷⁹ of reactive MBE growth of single crystal GaN films using ionized N_2 and NH_3 mixture as the nitrogen source,

the commonly seen MBE systems can be categorized into electron-cyclotron-resonance-MBE (ECRMBE), plasma-assisted-MBE (PAMBE) and ammonia-MBE (NH₃MBE), depending on how the active N species is produced.

ECRMBE and PAMBE differ in the plasma sources used to crack the N₂ molecules, which are operating at 2.45 GHz and 13.56 MHz, respectively. Since it was eventually realized that the ECR plasma source causes larger ion damage^{80,81} and a trade-off between the growth rate and crystal quality has to be adopted, nowadays ECRMBE is less popularly used compared to PAMBE.

Due to the limited cracking efficiency, the active N flux in a PAMBE system is not sufficiently high to fight the decomposition of GaN when the growth temperature is over ~800 °C, which sets the temperature upper limit for PAMBE GaN growth. This turns out to be a fundamental limit to achieve a high crystal quality by PAMBE. The optimum growth temperature, at which the step-flow growth is promoted, is estimated to be about half of the melting temperature.^{82–86} This argument suggests an optimum growth temperature of ~1050 °C, which indeed is very close to the MOCVD growth temperature and may explain the generally good material quality and device performance obtained by MOCVD.

Although PAMBE/ECRMBE is deemed to be a low temperature growth technique, there were still many encouraging results in 1990s, such as the demonstration of high room temperature mobility of 580 cm²/(V·s) in 1993⁸⁷ and the first Mg-doped p-type sample in 1992.⁸⁸ One of the most important steps towards understanding the PAMBE growth mechanism is the identification of the role the Ga/N ratio played on crystal quality. A systematic study of GaN homoepitaxy on MOCVD grown GaN templates by B. Heying et al.^{89,90} in early 2000s showed that there is a sharp surface morphology transition when the Ga/N flux ratio was varied. As is shown in Figure 1-4, the smoothest surface is obtained in the droplet regime (Ga-stable regime) in which the high Ga flux

leads to not only ~ 2 ML Ga adlayers but also the accumulation of 3D droplets. Within the N-stable regime there is no surface adlayer or droplet accumulation, and the surface is the roughest and characterized by crater-like microstructures originated from threading dislocations. At relatively high growth temperatures, there exists an intermediate regime in which the sample surface is free of Ga droplets but a certain amount of a dynamically stable liquid-like adlayer can exist.^{91,92} The sample surfaces grown in the intermediate regime consist of a large area flat terraces which are separated by deep faceted trenches.

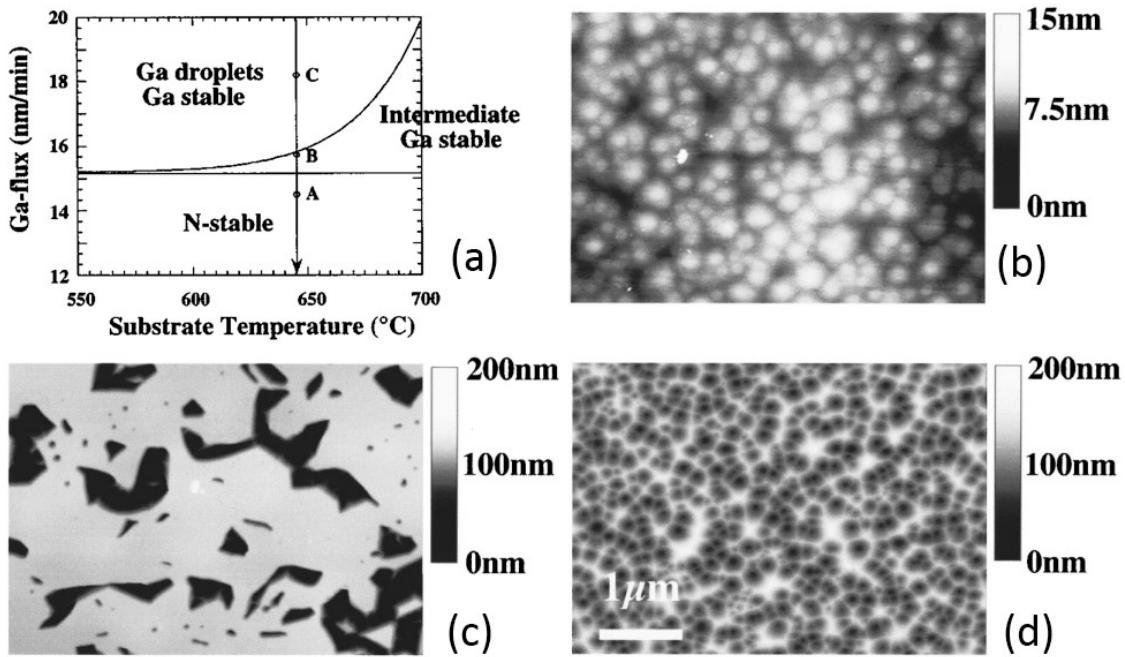


Figure 1-4. GaN growth regimes (a); the AFM images⁸⁹ of surface morphology for samples grown in Ga-stable, intermediate, and N-stable regimes (b)-(d).

The dramatic improvement of surface morphology and crystal quality is attributed to the enhanced adatoms diffusion due to the coverage of Ga adlayers. Similar metal/N flux ratio dependence on morphology and crystal quality were also found for PAMBE growth of AlN⁹³ and InN.⁹⁴ The detailed mechanism of the enhancement of adatom diffusion may be found in the

theoretical investigation by Neugebauer et al.,⁸⁵ which showed that an effective diffusion channel for nitrogen adatoms is formed when the sample surface is covered by indium adlayers. In a sense, these auto-surfactant adlayers is the very reason why PAMBE is considered to be a viable tool to grow nitride materials since it alleviates the temperature requirement which is not accessible to PAMBE system.

A relatively less frequently used MBE system is the NH_3MBE . As is suggested by the name, ammonia gas is the carrier of nitrogen and the active N species are generated when the NH_3 molecules were thermally cracked at the sample surface. For this reason, the NH_3MBE needs to operate at higher growth temperatures compared with the PAMBE, typically around 900 °C. The high supply rate of active nitrogen leads to much higher growth rates than that of PAMBE system. Also the large growth parameter window⁹⁵ allows easy growth process control. However, the corrosive nature of ammonia gas requires special design considerations for many components in the NH_3MBE systems. Further, the contradiction between the high temperatures required for cracking ammonia and the low dissociation temperature of InN makes the NH_3MBE unsuitable for InGaN growth.

So far the PAMBE grown HEMT devices show high mobility⁹⁶ and have comparably high-frequency performances to the MOCVD grown devices.¹² However, the performance of optoelectronic devices lagged behind the MOCVD grown devices. The first room temperature PAMBE grown pulsed lasers⁹⁷ were demonstrated in 2005, which is nine years later than the MOCVD grown counterpart.⁷ However, even this achievement is greatly due to the use of ultra-low dislocation density GaN substrates.

1.4. Growth of InN and InGaN

Early optical adsorption and transmission data suggested that the band gap of InN was

about 1.9 eV.^{98–100} These InN films under investigation were typically grown by sputtering techniques and thus had poor quality. In the early 2000s, MBE^{1,101–105} and MOCVD^{106,107} started to be used for InN growth and the crystal quality was eventually improved. The fundamental band gap of InN was then found to be dramatically smaller than 1.9 eV. Although the exactness is still under debate, new experimental values of the InN band gap are around 0.64 eV.^{1,18}

This revision of the band gap extends the long wavelength end of the InGaN ternary system from the visible into infrared range. Remarkably, it covers not only the whole visible spectral range but also the ~1310 nm and ~1550 nm windows for fiber optic communication systems. InGaN was proposed to be one of the best candidates for multijunction solar cells for high efficiency light harvesting,¹⁰⁸ and may also work as a light emitter or detector in fiber optic communication systems.¹⁰⁹

To the present date the native GaN substrate is still expensive and most InGaN-based devices are grown on foreign substrates such as sapphire and SiC. The mismatch of physical and chemical properties between substrates and GaN epilayers leads to a high dislocation density between 10^8 cm^{-2} to 10^{10} cm^{-2} . As shown in Figure 1-5, the substrates used in this dissertation had a dislocation density of $\sim 5 \times 10^8 \text{ cm}^{-2}$. These dislocations had been shown to be nonradiative recombination centers by CL investigations.^{110,111} Nonetheless, InGaN based LEDs and LDs surprisingly show good performance. It has been evaluated that the diffusion length of minority carriers is smaller than the average spacing of dislocations in InGaN films and therefore they are not captured by the dislocations before radiative recombination.^{112,113} A widely accepted explanation for this phenomenon is that there exists localized states caused by indium content variation and consequently the carriers are trapped by the localized states before they are captured by dislocations.¹¹⁴

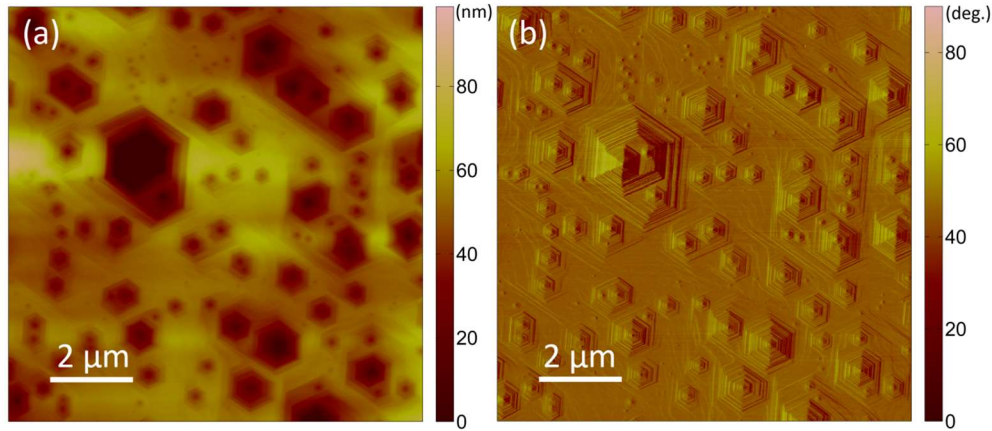


Figure 1-5. Dislocations in GaN revealed by H_3PO_4 etching at 200 °C. (a) and (b) are AFM images of a depth profile and a phase contrast profile, respectively.

However, the dislocation density must be reduced to further improve the performance of LEDs and LDs. It has been shown that at high driving current, the quantum efficiency is improved for both LEDs and LDs grown on low dislocation density substrates.¹¹⁵ This is because at high current operation the electrons can flow out of the localized states and be captured by nonradiative centers. Moreover, low dislocation density was found to dramatically improve lifetime of LDs,¹¹⁶ which is likely due to the reduction of dislocation-assisted diffusion of point defects and impurities towards the active region of lasers.^{117,118}

MOCVD has been the main production tool for InGaN-based short wavelength LEDs and LDs because of the high growth rate as well as the good crystal quality resulting from the high growth temperatures. However, the indium content in the active layer of these devices is low, typically smaller than 30%. The growth of high In content InGaN and InN films is still challenging. The dissociation of InN is thermally activated around 500 °C for both MBE^{94,119} and MOCVD^{106,107,120} systems, which practically determines the upper bound of InN growth temperature. For MOCVD systems, the active N species were provided via the pyrolysis of NH_3 gas which requires high growth temperatures typically ~1000 °C. This temperature contrast makes

PAMBE the advantageous tool to grow high In content InGaN and InN films because the active N species are independently provided through a plasma source and thus are not affected by the growth temperature.

Similar to the MBE GaN growth, the low growth temperature also presents a fundamental barrier for obtaining high crystal quality for InN. As previously discussed, the optimum temperature for InN growth should be around 800 °C, about half of the bulk InN melting temperature of 1873 °C.¹⁸ The high decomposition rate limits the InGaN film growth temperature to not much higher than the InN dissociation temperature of 500 °C, as is shown in Figure 1-6. Further, the low InGaN growth temperature also deteriorates the quality of GaN and AlGaN films which are often needed in a real device structure as quantum well barriers or electron blocking layers.

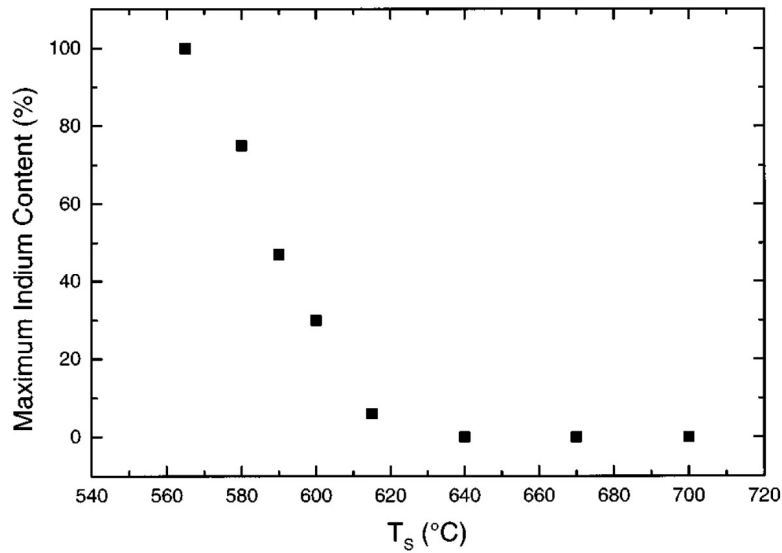


Figure 1-6. Maximum In content of InGaN films as a function of MBE growth temperature.¹²¹

Another fundamental difficulty for InGaN growth is the phase separation problem. As is shown in Figure 1-7(a), homogenous alloys are not stable in the region under the spinodal line

because even small fluctuations in composition lower the free energy and thus could trigger a phase separation. Between the spinodal and binodal lines, materials are metastable because there is an energy barrier against small composition fluctuation.¹²² From Figure 1-7(a), at the typical InGaN growth temperature between 500 °C and 600 °C, the phase separation can be prevented for In content no more than 20%. This difficulty for high In content incorporation could be alleviated by strain, which is important since most of the device structures are pseudomorphically grown on GaN substrates. The theoretical evaluation of strain effect on the spinodal lines by S. Figge et al.¹²³ is shown in Figure 1-7(b). It can be seen that if the InGaN film is compressively strained, the spinodal curves are modified in a way that is more favorable for high In content incorporation. The suppression of phase separation by strain had been experimentally confirmed by comparing the data of XRD and Raman scattering spectroscopy obtained on strained and relaxed InGaN films.¹²⁴

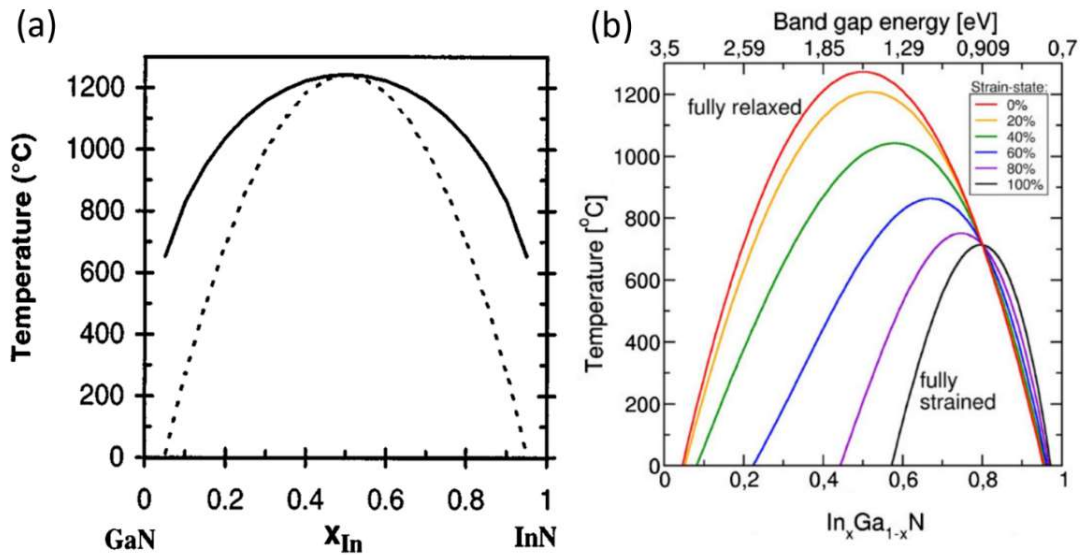


Figure 1-7. Theoretical spinodal and binodal curves^{122,125} of fully relaxed InGaN materials (a); theoretical spinodal curves with different strain states¹²³ (b).

Further, in InGaN epilayers, the In content is often found to be relatively low in the region close to the substrates, while it becomes higher in the region far away from the interfaces, an

alloying phenomenon known as “composition pulling^{122,126}” or “lattice latching”. This phenomenon was found not only in 2D films^{126–129} but also in nanowires.¹³⁰ Due to the lattice mismatch, the strain has a tendency to prevent the indium incorporation and thus “pulls” the indium content towards the low In content direction. The strain energy can be relieved by defect generation when the InGaN film becomes thicker and, thus, the increase of In content in the later stage of InGaN growth is accompanied by degradation of film quality.

Another alloying problem that causes structural inhomogeneity of InGaN films is the chemical ordering. The vertical ordering had been implied by observing forbidden XRD peaks¹³¹ and seeing additional diffraction spots in TEM selected area diffraction pattern.^{131–133} It was also directly observed by cross sectional TEM.¹³³ It has been shown that the phase separation and ordering can coexist in InGaN films, as competing mechanisms for strain relief.¹³¹ It appeared that for high In content films, the phase separation is more dominant while for low In content films ordering is more dominant.¹³¹ As an extreme case, Z. Wu et al. reported a spontaneous superlattice formation¹³⁴ during InGaN growth, as is displayed in Figure 1-8. This structure is only obtained at specific growth rates and has very long-range order and superior structural quality.

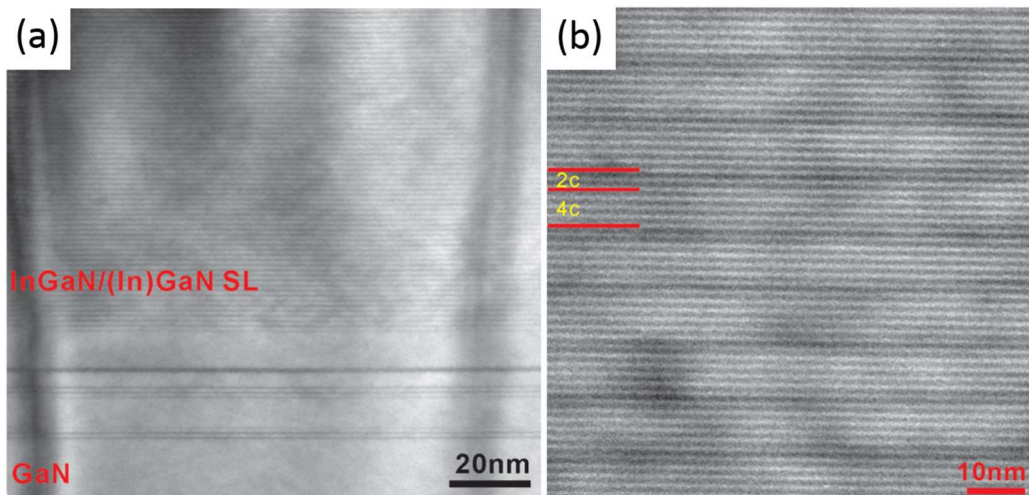


Figure 1-8. TEM images of spontaneously formed superlattice during InGaN growth in ref. 134.

1.5. The InN/GaN quantum wells

The alloying problems mentioned in the previous section presents major challenges in developing high quality random InGaN alloys for long wavelength applications. Therefore, alternative material designs and growth strategies are desired to approach the equivalent band gaps of InGaN random alloys while bypassing the alloying problems.

The “digital alloys”, superlattices with very short period, had been used in III-V semiconductor devices to alleviate certain growth difficulties of random alloys. For example, by changing the Al shutter duty cycle q , pseudo-quaternary digital alloys $q(\text{In}_{0.41}\text{Ga}_{0.21}\text{Al}_{0.38}\text{As}) + (1-q)(\text{In}_{0.66}\text{Ga}_{0.34}\text{As})$ were grown to mimic the random alloys.¹³⁵ This is to avoid the complex operation of changing group III cell temperatures or use more than one cell of the same species to achieve a sudden composition profile change.¹³⁶

The possibility of inserting InN QWs into the GaN matrix had been proposed and investigated by Yoshikawa et al..^{137,138} Atomically abrupt quantum wells were confirmed by TEM cross-sectional measurements even for samples grown as high as 650 °C and the QW thicknesses were found to be self-limited to 1 or 2 MLs. Being able to be grown at high temperatures is a remarkable property since it would also improve the crystal quality of GaN and AlGaIn layers, which are needed in real devices as both barriers and buffers. If the quantum well layers are coherent InN layers, by varying the GaN barrier thickness the effective In content in digital alloys could, in principle, reach 100%. More importantly, the alloying problems of random InGaIn, including the composition pulling, phase separation, and vertical chemical ordering, are naturally circumvented.

The electronic structure of the InN/GaN quantum wells are also promising. First principle calculations^{139–141} showed that for a single quantum well the InN thickness of only one monolayer

is sufficient to lower the band gap into the green region (< 2.2 eV). An exemplary result from ref. 141 is shown in Figure 1-9. The band gap of 2.0 eV is defined as the distance between the conduction band minimum (CBM) and valence band maximum (VBM). The spatial misalignment between the CBM and VBM results from the large internal electric field across the quantum well, a consequence of large polarization mismatch.

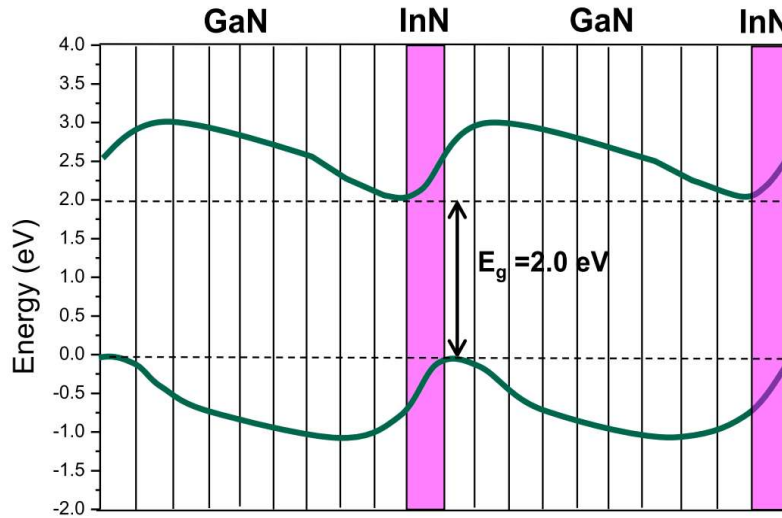


Figure 1-9. The conduction and valence band edge profiles of a 1-ML-InN/9-ML-GaN superlattice.¹⁴¹

Further increasing the quantum well thickness, thinning the GaN barrier or using InGaN instead of GaN as barriers, would potentially lead to lower band gap digital alloys for applications working in long wavelength region beyond green. There are a few preliminary works that demonstrate this band gap tunability. For example, Lin Zhou et al.¹⁴² showed that photoluminescence (PL) emissions are affected by the GaN barrier thickness. As another example, MQWs using InGaN as the barrier material were used as active layers of LEDs by Yuki et al.¹⁴³ and the emission peaks were shown to be red-shifted. Moreover, Miao et al. showed that the band gap of QW would experience a closing-to-reopening transition at a critical InN thickness of ~ 4

MLs. This transition would change the band ordering and transform the system into a 2D topological insulator.¹⁴⁴

The actual structure as well as the growth mechanism of these ultra-thin quantum wells is still under debate and have become a sharp research focus recently. The main confusion comes from the significantly higher energy of PL emissions. Against the expectation of a single consistent emission peak, the reported PL data from various groups showed a significant variation, with emission peak energy ranging from 2.8 eV to 3.3 eV.^{137,138,142,145–148} One possible reason for this discrepancy, as is pointed by Miao et al.,¹³⁹ is that the electrons/holes at CBM/VBM are recombining locally with holes/electrons since the large internal electric field separate CBM and VBM wave functions effectively. In ref. 140, it is suggested that the polarization induced electric field may be screened by the large amount of free carriers, and thus the reduced QCSE leads to higher PL energy. Recent TEM investigations^{149,150} point to a third explanation, the nominal InN wells in fact are a certain form of InGaN. Using TEM, Suski et al.¹⁴⁹ analyzed the c-lattice expansion in the vicinity of QWs with a 1-ML apparent thickness. An In concentration of 33% in the QWs was extrapolated. This concentration is reasonably consistent with the PL emission energy according to the theoretical evaluation in ref. 149 and 139. A more direct TEM investigation was recently carried out by G. P. Dimitrakopoulos et al..¹⁵⁰ Z-contrast was analyzed for samples having 1-ML and 2-ML apparent thickness. Although possible indium enrichment was found in the nearest neighboring layers, the indium content in the central 1-ML and 2-ML QWs was estimated to be ~0.23 and ~0.33, respectively.

The apparent thickness, 1 ML or 2 MLs, appeared to be specific to the growth conditions. For instance, Yoshikawa et al. have found that the growth temperature is critical to the maximum apparent QW thickness. At relatively low growth temperatures (< 650 °C), careful control of the

growth process allows the formation of quantum wells with thickness of either 1 ML or 2 MLs, which demonstrate PL emission peak at ~ 390 nm and ~ 430 nm, respectively.^{151,152} At higher growth temperatures only 1-ML or fractional-ML thick QW can be formed even with excessive indium deposition.

Given the complexity of the relationship between growth conditions and QW structural properties, systematic study of MQWs growth with various growth conditions need to be carried out to gain insight into growth mechanisms. In this dissertation, we focus on MQW growths at the two ends of the MQW growth temperature window, 550°C and 680°C . Through a series of in situ and ex situ characterizations, the influence of many key growth factors, such as the kinetics of indium coverage and surface reconstructions, were investigated and plausible growth mechanisms were proposed.

Chapter 2: Research methodology

2.1. Background of MBE

Since the early development in late 1960s and early 1970s,^{153–155} molecular beam epitaxy has been proven to be a powerful technique to grow a wide variety of high quality crystalline materials, including III-V, II-VI, Si/Ge, and oxide materials. MBE allows accurate growth rate control down to sub-monolayer per second level and in situ growth process monitoring by RHEED, which gives MBE the unique ability to grow epilayers with abrupt change in composition and doping profiles.

MBE is particularly suitable to study heterostructures where the quantum size effect is manifesting. A few well known examples which are initially prototyped using MBE are modulation-doped HEMT,¹⁵⁶ heterojunction bipolar transistors (HBT),¹⁵⁷ and quantum cascade lasers.¹⁵⁸ Advances in growth techniques, such as the vapor-liquid-solid mechanisms (VLS),^{159,160} the Stranski-Krastanov growth mode¹⁶¹ and droplet-epitaxy,¹⁶² extend the realm of MBE grown materials into nanostructures with higher dimensions of quantum confinement. Nowadays, MBE growth of 2D-confined (quantum wires) and 3D-confined (quantum dots) materials are active research areas.

Moreover, the research in condensed matter physics often put stringent requirements on material quality and device structural accuracy, which often makes MBE the only viable tool. For example, employing the modulation doping, the MBE grown GaAs/AlGaAs HEMTs can be refined to a level that the 2D electron transport is nearly not affected by impurities and interfacial roughness, in which case the electron-electron correlation is pronounced.¹⁶³ The realization of these high quality devices was a key step¹⁶⁴ for the successful observation of the fractional quantum Hall effect. A more recent example is the experimental realization of the 2D topological

insulator^{165,166} based on HgTe/(Hg,Cd)Te quantum wells. To observe the phase transition to topological insulator, the quantum well thickness on the order of a nanometer was systematically varied, which can only be achieved using MBE.

2.2. MBE system

The central idea of molecular beam epitaxy is to limit the pressure of the growth environment to a level that reactants from different sources do not interact with each other before reaching the substrate, which is heated to proper temperatures to activate adatom migration so that high quality crystalline epilayers can be grown.

The mean free path, or the average distance a molecule travels between two successive collisions, should be larger than the distance between sources and the substrate in a MBE chamber (typically ~20 cm). It has been estimated that, using a typical Ga cell temperature of 1250 K during growth, the requirement of mean free path would lead to a maximum total gas pressure of $\sim 5.8 \times 10^{-4}$ Torr.¹⁶⁷

For semiconductor materials, the unintentionally doped impurities must be suppressed since they may lead to unwanted background carriers and deep levels. For the convenience of discussion, the pressure is converted into unit of monolayers per second (ML/s), as is shown in Figure 2-1, according to typical crystal surface site densities in the range of 10^{14} to 10^{15} cm⁻² (the Ga surface site density of (0001) surfaces is 1.14×10^{15} cm⁻²). The typical MBE growth rate is on the order of 1 ML/s, corresponding to a pressure on the order of $\sim 1 \times 10^{-6}$ Torr.¹⁶⁸ Therefore, given that the bulk atomic density for GaN is on the order of 10^{23} cm⁻³, to limit the impurity concentration to below 10^{17} cm⁻³, a very rough estimation of the upper limit of dopant partial pressure is $\sim 10^{-12}$ Torr. Although this evaluation is overly simplified since it assumes that all impurities go into the material, the necessity of maintaining ultra-high vacuum (UHV) for MBE system is clarified.

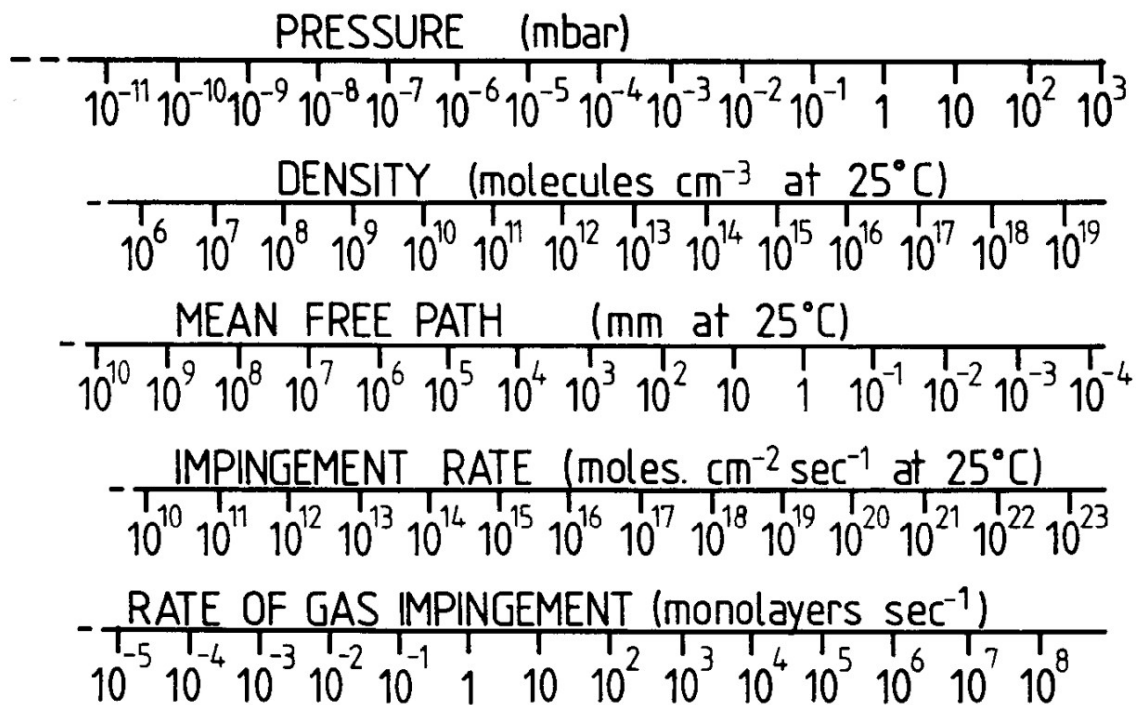


Figure 2-1. Unit conversions in vacuum technology.¹⁶⁸

The schematic of a nitride MBE system is shown in Figure 2-2. The whole system consisted of three connected chambers, namely the load lock chamber, the buffer chamber and the growth chamber. The main purpose of this design is to minimize the chance that impurities have to get introduced into the growth chamber. The substrates, carried by a trolley, were loaded into the load lock chamber first. Since a large amount of chemisorbed and physisorbed gas species up to a few monolayers could be accumulated on the sample and trolley surface during atmosphere exposure,¹⁶⁸ a preliminary outgas was carried out in the load lock chamber until the pressure was lowered to $\sim 10^{-8}$ Torr. Before being finally loaded into the growth chamber, the sample was outgassed again in the buffer chamber until the pressure reached $\sim 10^{-10}$ Torr, which was sufficiently close to the base pressure of the growth chamber. A pumping system consisting of a turbo molecular pump, an ion pump, and a titanium sublimation pump (TSP) kept the growth

chamber base pressure on the order of $\sim 10^{-10}$ Torr. Prior to sample growth, the cryoshroud of the growth chamber was filled with liquid nitrogen and effectively became a cryopump, which would further reduce the growth chamber pressure to the order of 10^{-11} Torr.

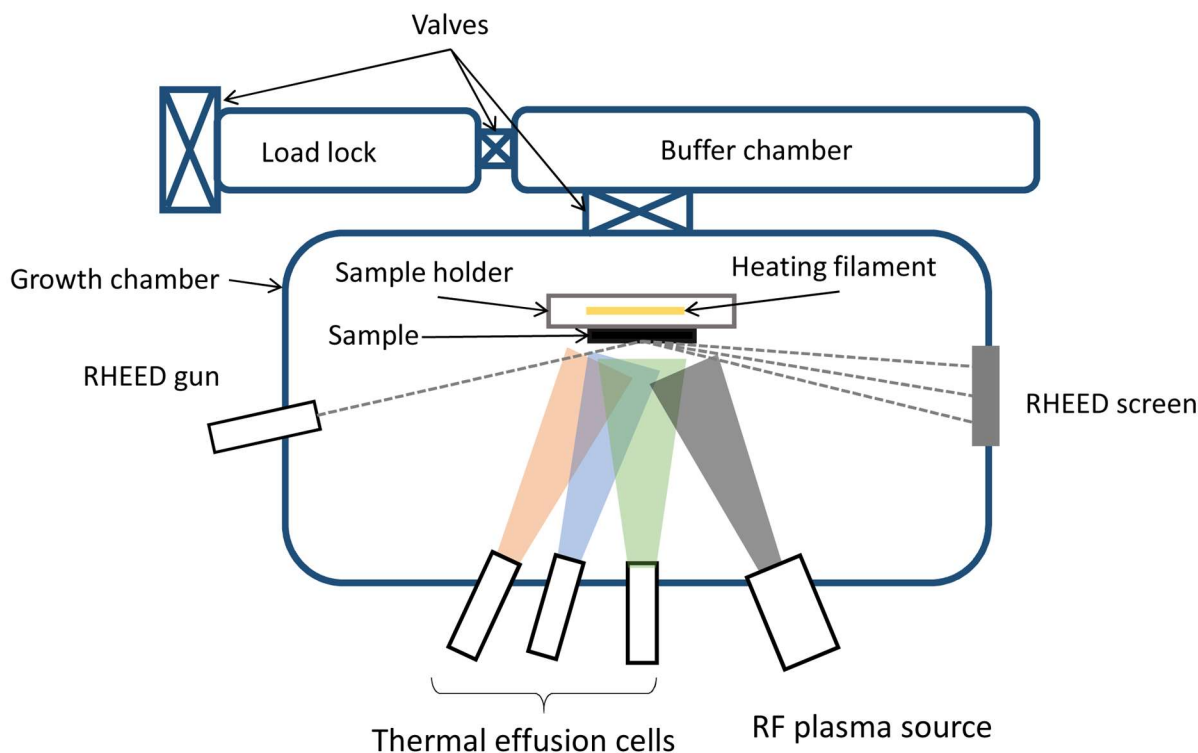


Figure 2-2. Schematic of nitride MBE system.

During growth, the group III species and the silicon (n-type dopant) were heated in thermal effusion cells to provide desired beam flux for growth. Since the p-type dopant material Mg had a very high vapor pressure, a valve cracker cell was used to control the flux. During operation, the cell was kept at a constant temperature and the beam flux was regulated by a needle valve. Special cell designs were needed to provide active nitrogen species because N_2 is very stable with a molecular cohesive energy of 9.8 eV.¹⁶⁹ For the PAMBE system used in this study, a radio-frequency (RF) plasma source was used to crack the stable N_2 molecules. The switching of the

molecular beams was controlled by mechanical shutters with a shuttering time on the order of 0.1 s. Therefore, the deposition could be controlled with an accuracy smaller than 0.1 ML.

Thanks to the low growth pressure, a versatile in situ surface characterization instrument, known as reflection high energy electron diffraction (RHEED), is generally installed on the MBE system. As is shown in Figure 2-2, during growth the electron beam from the RHEED gun hits the sample surface at a grazing angle, and then the reflected/diffracted beams create patterns on a phosphor screen, which are captured by a CCD camera and then analyzed by software. Because of the grazing incident angle, the electron beam only penetrates a few monolayers and, thus, there is rich information about the growth front contained in RHEED images.

2.3. RHEED fundamentals

The ability of in situ surface characterization by RHEED largely differentiates the MBE from other high-pressure growth techniques such as MOCVD. RHEED has been used to obtain valuable growth information such as: in situ growth rate, lattice constant of epilayers, symmetry of surface reconstructions, and growth mode transition. Since RHEED was extensively used in this research in defining growth parameters, studying surface kinetics and determining surface adsorbate structures, it is worth revising the working principles of RHEED in this section.

At grazing incident angles (no more than a few degrees), due to the extremely small penetration depth, the diffraction of the electron beam should be regarded as caused by 2D lattices rather than 3D lattices. The 2D lattices involved in diffraction contains the top few monolayers of the bulk material and, in many cases, surface reconstructions.

The diffraction conditions by a 2D lattice is most easily explained using the Ewald sphere, a conceptual sphere with a radius of the magnitude of the incident electron beam wavevector, which is illustrated as the gray sphere in Figure 2-3(a). The diffracted beams would produce an

intensity maxima when the difference between the incident beam wavevector and a diffracted beam wavevector have a projection on the 2D lattice plane coincide with a reciprocal lattice vector.

This is expressed as

$$(\mathbf{k}_{m,n} - \mathbf{k}_i)_{\parallel} \in \mathbf{G} \quad (\text{Equation 2.1})$$

where \mathbf{G} is the collection of all reciprocal space lattice vectors; \mathbf{k}_i is the wavevectors of the incident beam; and $\mathbf{k}_{m,n}$ are the wavevectors of the diffracted beams, which are indexed by m,n to be consistent with the position of intensity maxima in Figure 2-3(b).

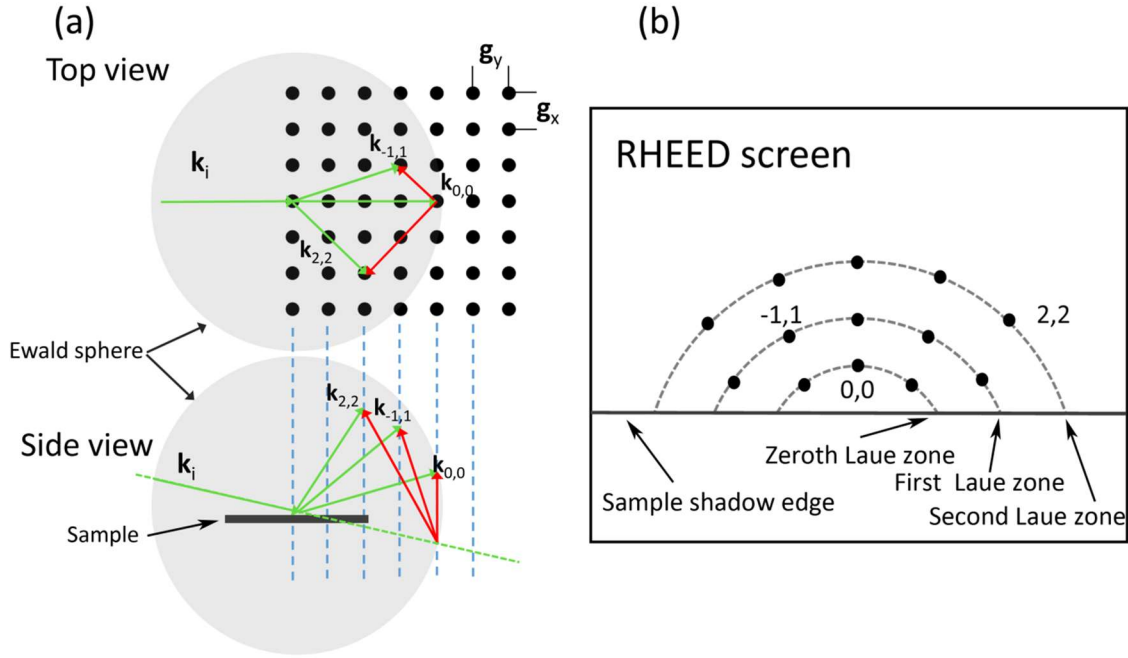


Figure 2-3. Electron beams scattered by a 2D lattice. (a) Ewald construction of 2D scattering; (b) the RHEED pattern on the phosphor screen corresponding to (a).

From the side view in Figure 2-3(a), each column of reciprocal space lattice sites defines an intercepting circle on the Ewald sphere, which is projected onto the RHEED screen as a Laue zone in Figure 2-3(b). Each RHEED intensity maxima sits on one of the Laue zones. Among these intensity maximas, a special one is the specular spot labeled as $(0,0)$ in Figure 2-3(b), whose

direction is along the reflection direction of \mathbf{k}_i . The diffraction condition is trivially satisfied for the specular spot because $\mathbf{k}_{m,n} - \mathbf{k}_i$ is perpendicular to the 2D lattice plane.

A common practice in MBE growth is to use the RHEED intensity oscillation to determine the in situ growth rate when the growth mode is layer-by-layer. Figure 2-4(a) shows different stages during the formation of a new atomic layer and their corresponding RHEED intensities. The RHEED intensity is a function of the surface roughness, and is strongest when the surface is the smoothest, i.e., when an atomic layer is completed. During growth the adatoms nucleate into 2D islands, which increases the surface roughness and decreases the RHEED intensity. As the growth continues, the expanding islands finally coalesce to form a new layer and the RHEED intensity is expected to return to the same value as defined by the previous complete layer. A continuous intensity oscillation defined in this manner is thus used to determine the growth rate. However, as is illustrated in Figure 2-4(b), in real growth there is an overall dampening of the RHEED oscillations, and eventually the intensity becomes a constant with time. This phenomenon suggests that the new layer may grow on partially formed layers, which roughens the surface by forming new steps. Eventually, the surface morphology would reach a steady state, meaning that the creation and coalescence of steps reach a balance, which is also the moment the intensity becomes invariant. Further, Due to miscuts or island formation, a real crystal surface is never a smooth infinite plane but consists of terraces divided by step-edges, which provide energetically favorable sites for nucleation. Therefore, crystal growth occurs when the adatoms on surfaces are captured by these step-edges. If this is the dominating growth mechanism, the growth mode is known as the step-flow growth mode, as is illustrated in Figure 2-4(c). Although the steps move during growth, the average roughness at any moment during growth is the same, and therefore, no RHEED intensity oscillation can be observed.

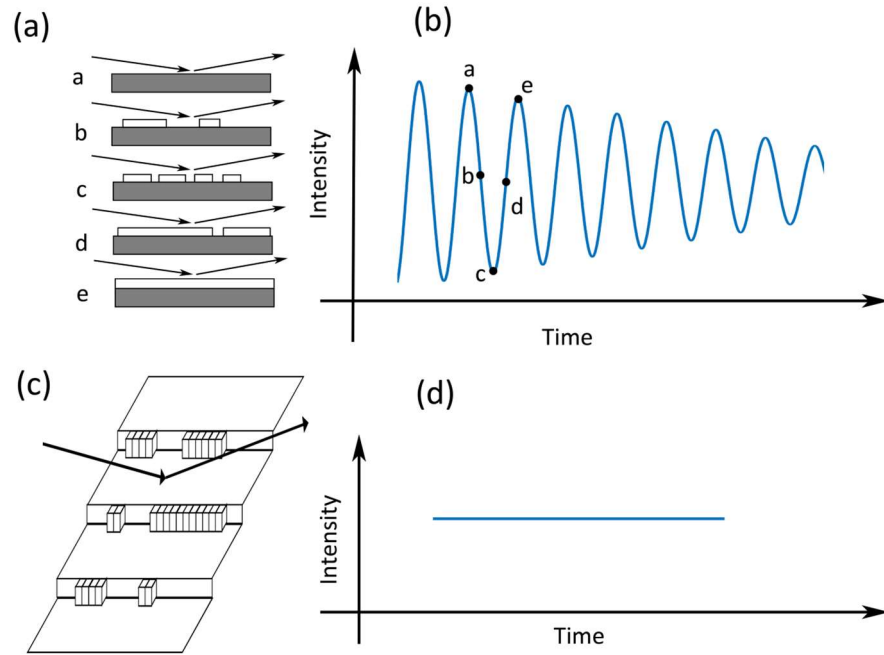


Figure 2-4. Layer-by-layer (a) and step-flow (c) growth mode and their RHEED intensity evolution during growth [(b) and (d)].

It should be noted that layer-by-layer and step-flow growth could coexist during growth. When the adatom migration length is not sufficiently large, the 2D island formation, and thus the layer-by-layer growth, could occur on the terraces. The transition of growth mode from layer-by-layer to step-flow was observed by Neave et al.,¹⁷⁰ when studying GaAs growth on vicinal surfaces. In ref. 170 the transition is due to thermally activated adatom migration at high growth temperatures. Moreover, being able to maintain the step-flow growth is a key factor for the success of the PAMBE growth of III-nitride materials, where, instead of high growth temperatures, liquid-like adlayers plays a key role in enhancing the surface migration.

2.4. III-nitride growth by PAMBE

As was introduced in Chapter 1, PAMBE is inherently a low temperature growth technique for nitride materials. For instance, the optimum growth temperature for GaN is estimated to be ~ 1050 °C, half of the GaN melting temperature.^{82–86} This temperature cannot be reached during

PAMBE GaN growth because GaN decomposition begins at $\sim 800^\circ\text{C}$ under typical PAMBE growth pressures.

It is found that the material quality benefits greatly from the surfactant effect of metal adlayers.^{89,90,93,94} Therefore, the requirement of high growth temperature is alleviated if the growth is carried out in the Ga-rich regime, in which the metal/N flux ratio is so high that the surface is covered by metal adlayers as well as droplets. The surfactant effect may be explained by the adlayer enhanced lateral diffusion mechanism proposed by J. Neugebauer et al..⁸⁵ The influence of In adlayers on the adatom diffusion on the GaN(0001) surface is investigated with first principle calculations. As is shown in Figure 2-5, the energetically favorable sites for N adatoms to stay are the hollow sites (H3 sites) below the In adlayer, and the diffusion barrier is the smallest if the diffusion path passes beneath the In atoms. Therefore, an effective diffusion channel below the In adlayer, indicated by the yellow arrows in Figure 2-5, is identified for N adatoms.

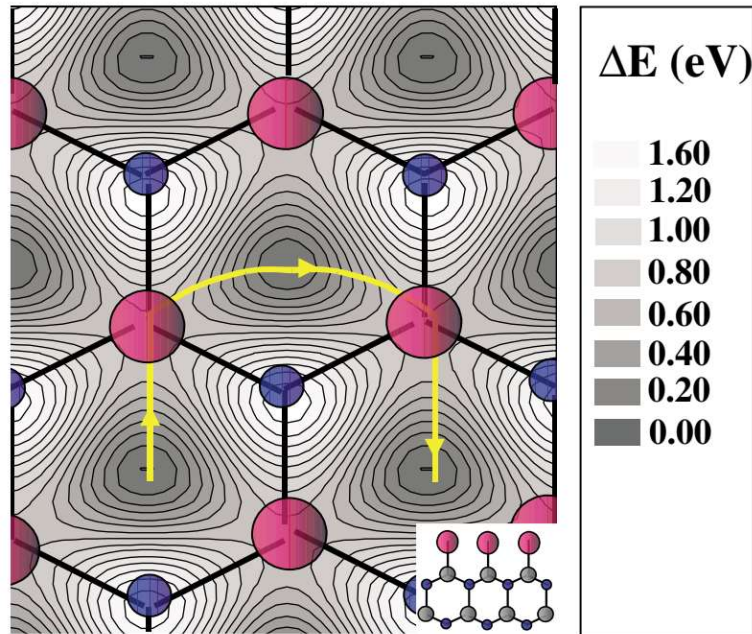


Figure 2-5. N diffusion channel between a GaN(0001) substrate and an indium adlayer.⁸⁵ The diffusion path is indicated by yellow arrows. The blue, gray and red colors denote nitrogen, gallium and indium atoms respectively. The inset is the side view of the GaN substrate and In adlayer.

Although growth can be easily set in the droplet regime by using a large metal flux, the metal flux overpressure, if not controlled well, leads to excessive surface droplets accumulation. It has been shown that there are undesirable morphology variations under droplets.¹⁷¹ The unchecked droplets may also lead to the formation of compositionally unknown clusters, presumably GaN_x, which lower the buffer breakdown voltage for HEMT devices.¹² More relevant to this work, for multiple quantum well or superlattice growth, the left-over droplets after each quantum well growth cycle give a different initial growth condition for the next growth cycle, and thus may cause structural nonuniformity among quantum wells.

As a result, the most ideal growth scenario for III-nitride materials is that the metal/N flux ratio is adjusted to a point that the dynamically stable metal adlayers, e.g., 2.3 MLs for GaN, are maintained while no 3D droplets are accumulating. In other words, the metal flux is at the boundary between Ga-rich and intermediate regimes (see Figure 1-4(a)). In reality, such an optimum flux cannot be defined for the entire sample surface. This is because the optimum flux is sensitive to temperature and a uniform temperature profile over the whole sample surface is hard to obtain. Therefore, a slight Ga/flux overpressure is used to ensure a good surface morphology uniformity over the whole sample surface while avoiding excessive droplets accumulation. In routine growth, this slight metal-rich condition is found by tracking the RHEED intensity transient.

Without loss of generality, the procedure to find the optimum growth condition discussed in this section is based on GaN growth and can be straightforwardly extended to AlN and InN growth. Figure 2-6 shows a typical RHEED intensity evolution before, during, and after metal-rich GaN growth at the growth temperature of ~790 °C. Once the N and Ga shutter were opened at t_0 , the RHEED intensity began to drop from a stable value corresponding to a completely dry GaN surface. It initially dropped drastically and then reached a relatively stable phase after t_1 .

The fast drop was mainly due to the buildup of ~ 2.3 ML Ga adlayers which were liquid-like and attenuated the RHEED intensity drastically. 3D droplets started to form following the ~ 2.3 ML adlayers with a resulting weaker shadowing effect and, thus, the intensity during this stage appeared to be roughly stable.¹⁷² After the N and Ga shutters were closed at t_2 , there was a delay before the intensity onset at t_3 . During this stage the desorption only reduced the size of the droplets while the ~ 2.3 ML adlayers remained intact. This was because the droplets compensated the loss from liquid-like adlayers at a very fast rate.¹⁷² Finally, the remaining ~ 2.3 ML adlayers started to desorb after t_3 and the RHEED intensity was eventually returned to the level corresponding to a dry GaN surface.

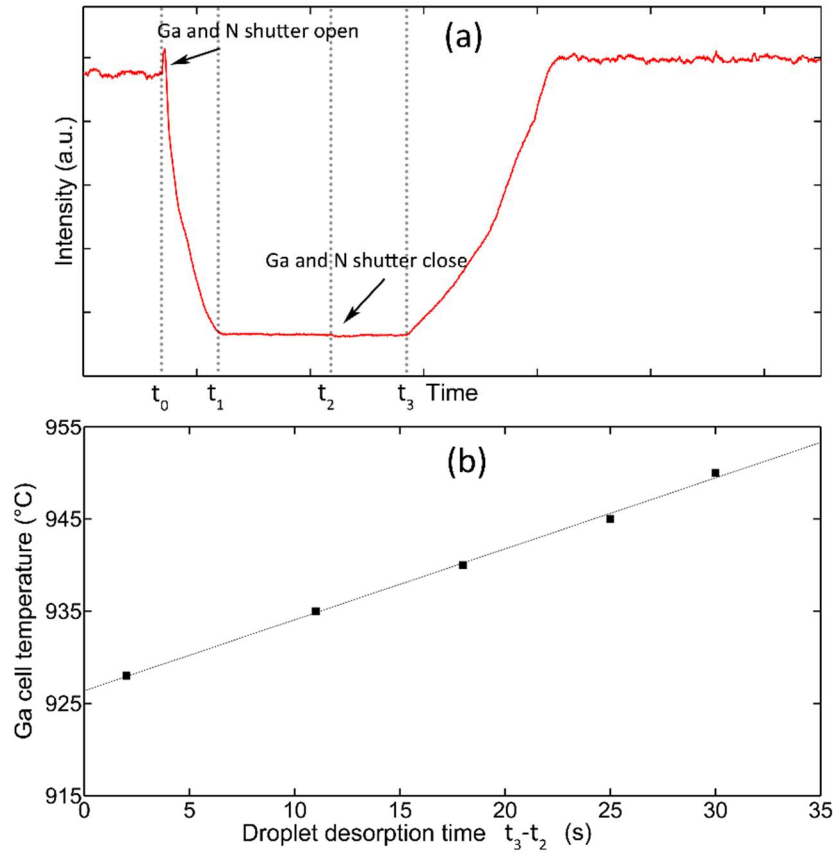


Figure 2-6. RHEED intensity evolution of Ga-rich GaN growth (a); Ga cell temperature as a function of droplets desorption time $t_3 - t_2$ (b).

As shown in Figure 2-6(b), the droplet desorption time $t_3 - t_2$ showed a good linear relationship with the Ga cell temperature for a fixed growth time $t_2 - t_0$. Following this assumption, the linear interpolation of Ga cell temperatures to when the droplet desorption time vanished corresponds to the Ga flux ϕ_0 that would build ~ 2.3 -ML Ga adlayers during the GaN growth time. ϕ_0 determined with this method lies in the Ga-rich regime and is generally larger than the ideal flux ϕ_b at the boundary between intermediate and Ga-rich regimes. Obviously, it takes a longer time to build the same ~ 2.3 -ML Ga adlayers if a smaller Ga flux is used. As a result, the extracted ϕ_0 would be closer to ϕ_b if a longer growth time $t_2 - t_0$ is used. At the GaN buffer growth temperatures $\sim 790^\circ\text{C}$ used in this research, the Ga flux ϕ_0 was routinely obtained using a growth time $t_2 - t_0$ of 30 s. The ϕ_0 extracted this way kept most of the sample surface in the Ga-rich regime without excessive droplet accumulation.

At low growth temperatures, the desorption time would be unreasonably long since the thermal desorption rate of Ga is slow. In this case, the procedure to extract ϕ_0 could be modified such that only the Ga shutter was closed at the moment t_2 while the nitrogen shutter was still left open. Therefore, the surface Ga accumulation was consumed by GaN growth instead of thermal desorption. In this case the RHEED intensity recovery behavior is still very similar to that shown in Figure 2-6(a), and the time to consume droplets $t_3 - t_2$ also has a good linear relationship with Ga cell temperatures. Therefore, ϕ_0 was extracted in a similar manner to the high temperature growths.

Further, the GaN growth diagram was obtained using the above mentioned procedure and is shown in Figure 2-7. The Ga flux ϕ_b at the boundary of the Ga-rich regime is approximated by

ϕ_0 since a large growth time of 100 s was used. ϕ_b can be fitted nicely using⁸⁹

$$\phi_b = A \exp\left(\frac{E_a}{k_B T}\right) + \phi_N \quad (\text{Equation 2.2})$$

where k_B is the Boltzmann's constant; $E_a = -2.57 \text{ eV}$; $A = 1.00 \times 10^5 \text{ Torr}$; and the effective nitrogen flux $\phi_N = 1.09 \times 10^{-7} \text{ Torr}$. When the temperature is low ($< \sim 675^\circ \text{C}$), the desorption of Ga becomes negligible and the Ga-rich regime boundary ϕ_b is essentially the same as the effective nitrogen flux ϕ_N .

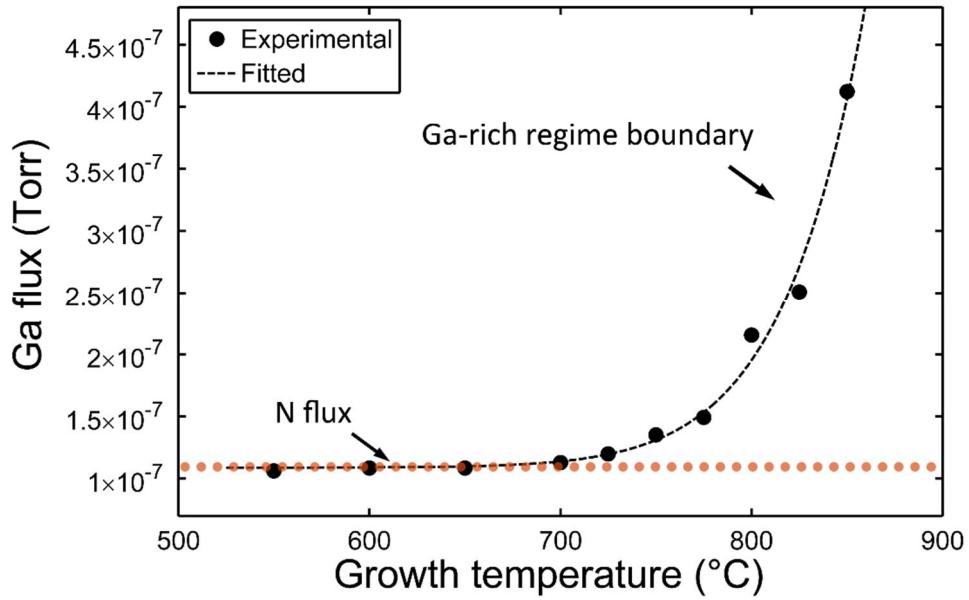


Figure 2-7. GaN growth diagram.

2.5. The eight-band k.p method

2.5.1. Bulk materials

The electron Hamiltonian taking into account the spin-orbit interaction is

$$H = \frac{\mathbf{p}^2}{2m_0} + V(\mathbf{r}) + \frac{\hbar}{4m_0^2 c^2} (\boldsymbol{\sigma} \times \nabla V) \cdot \mathbf{p} \quad (\text{Equation 2.3})$$

where m_0 is the electron rest mass; c is the speed of light; and the components of $\boldsymbol{\sigma}$ (σ_x , σ_y and σ_z) are Pauli matrices. Due to the translational symmetry of the crystals, the wave function of an energy eigen state has a general form (Bloch theorem)

$$\psi_{\mathbf{k}}(\mathbf{r}) = e^{i\mathbf{k}\cdot\mathbf{r}} u_{\mathbf{k}}(\mathbf{r}) \quad (\text{Equation 2.4})$$

where $u_{\mathbf{k}}(\mathbf{r})$ is a periodic function with the lattice periodicity and \mathbf{k} is a wavevector in the first Brillouin zone. Applying the Hamiltonian on Eq. 2.4, the energy eigenvalue problem can be rearranged to be

$$H(\mathbf{k})u_{\mathbf{k}}(\mathbf{r}) = E(\mathbf{k})u_{\mathbf{k}}(\mathbf{r}) \quad (\text{Equation 2.5})$$

where $E(\mathbf{k})$ is an energy eigenvalue. Here $H(\mathbf{k})$ can be written explicitly as^{173,174}

$$H(\mathbf{k}) \approx H_0 + \frac{\hbar^2 k^2}{2m_0} + \frac{\hbar}{m_0} \mathbf{k} \cdot \mathbf{p} + H_{so} \quad (\text{Equation 2.6})$$

where

$$H_0 = \frac{\mathbf{p}^2}{2m_0} + V(\mathbf{r}) \quad (\text{Equation 2.7})$$

and the spin-orbit interaction energy operator is

$$H_{so} = \frac{\hbar}{4m_0^2 c^2} (\boldsymbol{\sigma} \times \nabla V) \cdot \mathbf{p} \quad (\text{Equation 2.8})$$

The central idea of the $\mathbf{k}\cdot\mathbf{p}$ theory is to use a small set of basis functions to approximate the energy dispersion in the vicinity of the Brillouin zone center. For wurtzite materials, the conduction band and the valence band can be treated simultaneously by employing the following eight zone-center ($\mathbf{k} = 0$) states

$$\{|S, \uparrow\rangle, |S, \downarrow\rangle, |X, \uparrow\rangle, |Y, \uparrow\rangle, |Z, \uparrow\rangle, |X, \downarrow\rangle, |Y, \downarrow\rangle, |Z, \downarrow\rangle\} \quad (\text{Equation 2.9})$$

where the first two s-like states are the conduction band edge states and the rest six p-like zone-

center states are energetically close to the valence band edge. To maximally diagonalize the Hamiltonian, the following new basis states were used

$$\left\{ \begin{aligned} |1\rangle &= |iS, \uparrow\rangle, |2\rangle = \frac{-1}{\sqrt{2}} |X + iY, \uparrow\rangle, |3\rangle = \frac{1}{\sqrt{2}} |X - iY, \uparrow\rangle, |4\rangle = |Z, \uparrow\rangle \\ |5\rangle &= |iS, \downarrow\rangle, |6\rangle = \frac{1}{\sqrt{2}} |X - iY, \downarrow\rangle, |7\rangle = \frac{-1}{\sqrt{2}} |X + iY, \downarrow\rangle, |8\rangle = |Z, \downarrow\rangle \end{aligned} \right\} \quad (\text{Equation 2.10})$$

The Hamiltonian matrix, $H_{8 \times 8}$, can then be written as

$$H_{8 \times 8} = H^1 + H^L + H_{strain} \quad (\text{Equation 2.11})$$

H^1 is obtained by treating the eight basis functions as a complete set where its entries are of the form $H_{ij}^1 = \langle i | H | j \rangle$

$$H^1 = \frac{\hbar^2 \mathbf{k}^2}{2m_0} + \begin{pmatrix} E_c & -\frac{k_+ P_2}{\sqrt{2}} & \frac{k_- P_2}{\sqrt{2}} & k_z P_1 & 0 & 0 & 0 & 0 \\ -\frac{P_2 k_-}{\sqrt{2}} & E_v + \Delta_1 + \Delta_2 & 0 & 0 & 0 & 0 & 0 & 0 \\ \frac{P_2 k_+}{\sqrt{2}} & 0 & E_v + \Delta_1 - \Delta_2 & 0 & 0 & 0 & 0 & \sqrt{2} \Delta_3 \\ P_1 k_z & 0 & 0 & E_v & 0 & 0 & \sqrt{2} \Delta_3 & 0 \\ 0 & 0 & 0 & 0 & E_c & \frac{k_- P_2}{\sqrt{2}} & -\frac{k_+ P_2}{\sqrt{2}} & k_z P_1 \\ 0 & 0 & 0 & 0 & \frac{P_2 k_+}{\sqrt{2}} & E_v + \Delta_1 + \Delta_2 & 0 & 0 \\ 0 & 0 & 0 & \sqrt{2} \Delta_3 & -\frac{P_2 k_-}{\sqrt{2}} & 0 & E_v + \Delta_1 - \Delta_2 & 0 \\ 0 & 0 & \sqrt{2} \Delta_3 & 0 & P_1 k_z & 0 & 0 & E_v \end{pmatrix}$$

$$(\text{Equation 2.12})$$

where $k_{\pm} = k_x \pm ik_y$; $\langle S | H_0 | S \rangle = E_c$ is the conduction band edge; Δ_1 is the crystal field splitting energy such that

$$\langle X | H_0 | X \rangle = \langle Y | H_0 | Y \rangle = E_v + \Delta_1 \quad (\text{Equation 2.13})$$

and

$$\langle Z | H_0 | Z \rangle = E_v \quad (\text{Equation 2.14})$$

Further, $\Delta_2 = \Delta_3 = \Delta_{SO} / 3$ is originated from the spin-orbit interaction. If rewriting the spin-orbit interaction operator in terms of the Pauli matrices, then

$$H_{SO} = H_{sx} \sigma_x + H_{sy} \sigma_y + H_{sz} \sigma_z \quad (\text{Equation 2.15})$$

and Δ_{SO} is defined as

$$\langle X | H_{sz} | Y \rangle = \langle Y | H_{sx} | Z \rangle = \langle Z | H_{sy} | X \rangle = -i\Delta_{SO} / 3 \quad (\text{Equation 2.16})$$

The non-vanishing momentum matrix elements lead to the definition of P_1 and P_2

$$P_1 = \frac{-i\hbar}{m_0} \langle S | p_z | Z \rangle \quad (\text{Equation 2.17})$$

and

$$P_2 = \frac{-i\hbar}{m_0} \langle S | p_y | Y \rangle = \frac{-i\hbar}{m_0} \langle S | p_x | X \rangle \quad (\text{Equation 2.18})$$

Further, the influence of remote energy bands other than the eight dominant bands was folded into the matrix H^L using the Löwdin perturbation theory.^{173,175,176} If C is the collection of the eight basis functions and R is the collection of all the remote bands, then for $m, n \in C$

$$H_{mn}^L = \sum_{r \in R} \frac{H_{mr} H_{rn}}{E - H_{rr}} \quad (\text{Equation 2.19})$$

Considering that^{173,177}

$$H_{mr} = \langle m | H(\mathbf{k}) | r \rangle \approx \langle m | \frac{\hbar}{m_0} \mathbf{k} \cdot \mathbf{p} | r \rangle = \frac{\hbar}{m_0} \mathbf{k} \cdot \langle m | \mathbf{p} | r \rangle \quad (\text{Equation 2.20})$$

the entries of H_{mn}^L consists of second order terms in \mathbf{k} , given by

$$H_{mn}^L = \frac{\hbar^2}{2m_0^2} \sum_{\substack{r \in R \\ \alpha, \beta \in \{x, y, z\}}} \frac{p_{mr}^\alpha p_{rn}^\beta + p_{mr}^\beta p_{rn}^\alpha}{E - H_{rr}} k_\alpha k_\beta \quad (\text{Equation 2.21})$$

Finally, the strain effect for epilayers grown along the [0001] direction can be introduced by modifying the diagonal line of $H_{8 \times 8}^{173}$ and, thus, H_{strain} is a diagonal matrix with the diagonal line

$$[AcS, HS, HS, PS, AcS, HS, HS, PS] \quad (\text{Equation 2.22})$$

These entries are defined as^{173,178,179}

$$\begin{cases} PS = D_1 \varepsilon_{zz} + D_2 (\varepsilon_{xx} + \varepsilon_{yy}) \\ QS = D_3 \varepsilon_{zz} + D_4 (\varepsilon_{xx} + \varepsilon_{yy}) \\ HS = PS + QS \\ AcS = a_{cz} \varepsilon_{zz} + a_{ct} (\varepsilon_{xx} + \varepsilon_{yy}) \end{cases} \quad (\text{Equation 2.23})$$

where ε_{xx} , ε_{yy} and ε_{zz} are strains; a_{cz} and a_{ct} are deformation potentials for the conduction band; and D_1 to D_4 are deformation potentials related to the valence band.

2.5.2. Heterostructures

For heterostructures, the $\mathbf{k} \cdot \mathbf{p}$ theory is based on the envelop function expansion method developed by Burt.^{180–182} Assuming $U_n(\mathbf{r})$ is a set of complete and orthogonal functions that have the crystal lattice periodicity, then a wavefunction is expanded as

$$\psi(\mathbf{r}) = \sum_n F_n(\mathbf{r}) U_n(\mathbf{r}) \quad (\text{Equation 2.24})$$

where $F_n(\mathbf{r})$ are the corresponding envelop functions of $U_n(\mathbf{r})$. If $\psi(\mathbf{r})$ is an energy eigenfunction, inserting Eq. 2.24 into Schrödinger's equation leads to

$$\left(\frac{-\hbar^2}{2m_0} \nabla^2 + V(\mathbf{r}) \right) \psi(\mathbf{r}) = E\psi(\mathbf{r}) \quad (\text{Equation 2.25})$$

Expanding both sides of Eq. 2.25 in terms of basis functions $U_n(\mathbf{r})$, a set of coupled integro-differential equations of only the envelop functions is obtained

$$\frac{-\hbar^2}{2m_0} \nabla^2 F_n(\mathbf{r}) + \sum_m \frac{-i\hbar}{m_0} \mathbf{p}_{nm} \cdot \nabla F_m(\mathbf{r}) + \sum_m \int d\mathbf{r}' H_{nm}(\mathbf{r}, \mathbf{r}') F_m(\mathbf{r}') = EF_n(\mathbf{r}) \quad (\text{Equation 2.26})$$

where

$$\begin{cases} \mathbf{p}_{nm} = \frac{1}{V} \int_{UC} U_n^*(\mathbf{r}) \mathbf{p} U_m(\mathbf{r}) \\ T_{nm} = \frac{1}{V} \int_{UC} U_n^*(\mathbf{r}) \frac{\mathbf{p}^2}{2m_0} U_m(\mathbf{r}) \\ H_{nm}(\mathbf{r}, \mathbf{r}') = T_{nm} \Delta(\mathbf{r} - \mathbf{r}') + V_{nm}(\mathbf{r}, \mathbf{r}') \\ \Delta(\mathbf{r} - \mathbf{r}') = \frac{1}{\Omega} \sum_{\mathbf{k} \in FBZ} e^{i\mathbf{k} \cdot (\mathbf{r} - \mathbf{r}')} \end{cases} \quad (\text{Equation 2.27})$$

where V and Ω are volumes of the unit-cell in real and reciprocal spaces.

The treatment of $V_{nm}(\mathbf{r}, \mathbf{r}')$ is sophisticated and the detailed analysis can be found in ref. 182. Although Eq. 2.26 is an exact expression, the last integration term on the left-hand side brings difficulties for the implementation of a numerical solver. In ref. 182, Burt argued that if the envelop functions are slowly varying the non-local parts of the term $V_{nm}(\mathbf{r}, \mathbf{r}')$ can be ignored and thus Eq. 2.26 is modified into

$$\frac{-\hbar^2}{2m_0} \nabla^2 F_n(\mathbf{r}) + \sum_m \frac{-i\hbar}{m_0} \mathbf{p}_{nm} \cdot \nabla F_m(\mathbf{r}) + \sum_m H_{nm}(\mathbf{r}) F_m(\mathbf{r}) = EF_n(\mathbf{r}) \quad (\text{Equation 2.28})$$

where $H_{nm}(\mathbf{r})$ are the local energy matrix elements with respect to $U_n(\mathbf{r})$ and $U_m(\mathbf{r})$.

Further, to build a practical theory using a limited number of basis functions, F_n are separated into two groups in the spirit of Löwdin perturbation theory.^{173,175,176} The dominant bands

are labeled with C , while all other bands are labeled with R (remote bands). Using the slow-varying property of envelop functions, a remote band $F_r(\mathbf{r})$ can be approximated in terms of the dominant bands as

$$F_r(\mathbf{r}) \approx (E - H_{rr})^{-1} \sum_{s'} \left[\frac{-i\hbar}{m_0} \mathbf{p}_{rs'} \cdot \nabla F_{s'}(\mathbf{r}) + H_{rs'}(\mathbf{r}) F_{s'}(\mathbf{r}) \right] \quad (\text{Equation 2.29})$$

where the index $s' \in C$ and $r \in R$. Inserting Eq. 2.29 back into Eq. 2.28 and neglecting the nonsignificant terms leads to^{181,183}

$$\begin{aligned} & \frac{-\hbar^2}{2m_0} \sum_{s'} \nabla \cdot [\gamma_{ss'}^{(r)}(\mathbf{r}) \cdot \nabla F_{s'}(\mathbf{r})] \\ & + \sum_{s'} \frac{-i\hbar}{m_0} \mathbf{p}_{ss'} \cdot \nabla F_{s'}(\mathbf{r}) + \sum_{s'} H_{ss'}^{(2)}(\mathbf{r}) F_{s'}(\mathbf{r}) = E F_s(\mathbf{r}) \end{aligned} \quad (\text{Equation 2.30})$$

where $s \in C$ and $H_{ss'}^{(2)}(\mathbf{r})$ can be understood as energy matrix elements corrected to the second order using perturbation theory

$$H_{ss'}^{(2)}(\mathbf{r}) = H_{ss'}(\mathbf{r}) + \sum_r \frac{H_{sr}(\mathbf{r}) H_{rs'}(\mathbf{r})}{E - H_{rr}(\mathbf{r})} \quad (\text{Equation 2.31})$$

$\gamma_{ss'}^{(r)}(\mathbf{r})$ in Eq. 2.30 represents the interaction between dominant bands and the remote bands and can be regarded as the generalized effective mass tensor¹⁸¹

$$\gamma_{ss'}^{(r)}(\mathbf{r}) = \mathbf{I} \delta_{ss'} + \sum_r \frac{2}{m_0} \frac{\mathbf{p}_{sr} \mathbf{p}_{rs'}}{E - H_{rr}(\mathbf{r})} \quad (\text{Equation 2.32})$$

Therefore, the first term in Eq. 2.30 can be re-written explicitly to be

$$\frac{-\hbar^2}{2m_0} \nabla^2 F_s(\mathbf{r}) + \sum_{\substack{s',r \\ \alpha, \beta \in \{x,y,z\}}} \frac{-\hbar^2}{m_0^2} \partial_\alpha \frac{p_{sr}^\alpha p_{rs'}^\beta}{E - H_{rr}(\mathbf{r})} \partial_\beta F_{s'}(\mathbf{r}) \quad (\text{Equation 2.33})$$

For bulk crystals, quantities such as $\gamma_{ss'}^{(r)}(\mathbf{r})$ and $H_{rr}(\mathbf{r})$ are position-independent and it is easy to see that $F_n(\mathbf{r})$ has the form $A_n(\mathbf{k}) e^{i\mathbf{k} \cdot \mathbf{r}}$. In this case one can find

$$\hat{k}_\alpha = -i\partial_\alpha \leftrightarrow k_\alpha \quad (\text{Equation 2.34})$$

Therefore, from the similarity between Eq. 2.33 and Eq. 2.21, it is easy to see that Eq. 2.30 can be reduced to the spinless version of the bulk \mathbf{k}, \mathbf{p} Hamiltonian. For heterostructures where the translational symmetry is broken at least in one dimension, quantities such as $H_{rr}(\mathbf{r})$ become position-dependent and thus the ordering of differential operators in Eq. 2.33 becomes relevant. It is worth noting that the theoretical analysis of correct operator ordering is an essential feature of Burt's envelop function theory. Traditional envelop function theories typically use ad hoc operator orderings to keep the hermicity of the Hamiltonian or to maintain numerical stability. This lacks physical stand ground and may lead to erroneous results.¹⁸³

The eight-band \mathbf{k}, \mathbf{p} Hamiltonian based on the basis states in Eq. 2.10 is organized in a matrix form^{144,183,184}

$$\begin{pmatrix} E_c & -\frac{\hat{k}_+ P_2}{\sqrt{2}} & \frac{\hat{k}_- P_2}{\sqrt{2}} & \hat{k}_z P_1 & 0 & 0 & 0 & 0 \\ & F & W & U & 0 & 0 & 0 & 0 \\ & & G & V & 0 & 0 & 0 & \sqrt{2}\Delta_3 \\ & & & \Lambda & 0 & 0 & \sqrt{2}\Delta_3 & 0 \\ & & & & E_c & \frac{\hat{k}_- P_2}{\sqrt{2}} & -\frac{\hat{k}_+ P_2}{\sqrt{2}} & \hat{k}_z P_1 \\ & \dagger & & & & F & W^\dagger & V \\ & & & & & & G & U \\ & & & & & & & \Lambda \end{pmatrix} \quad (\text{Equation 2.35})$$

Entries, such as F and W , may contain terms with the ordering $\hat{k}_\alpha \eta(\mathbf{r}) \hat{k}_\beta$, where $\eta(\mathbf{r})$ is a position dependent quantity. The effect of the dagger operator is seen from the example

$$(\hat{k}_z \eta(\mathbf{r}) \hat{k}_+)^\dagger = \hat{k}_- \eta(\mathbf{r})^* \hat{k}_z \quad (\text{Equation 2.36})$$

where $\hat{k}_\pm = \hat{k}_x \pm i\hat{k}_y$. For quantum wells, the translational symmetry are still valid in the directions

perpendicular to the growth direction (z), therefore the envelop function can be written as

$$F_n(\mathbf{r}) = f_n(z)e^{i\mathbf{k}_{\parallel}\mathbf{r}} \quad (\text{Equation 2.37})$$

As a result, for quantum wells grown along the z direction

$$\begin{cases} \hat{k}_x = -i \frac{\partial}{\partial x} \rightarrow k_x \\ \hat{k}_y = -i \frac{\partial}{\partial y} \rightarrow k_y \\ \hat{k}_z = -i \frac{\partial}{\partial z} \end{cases} \quad (\text{Equation 2.38})$$

Chapter 3: InN/GaN MQW growth at 680 °C

3.1. Introduction

High growth temperature is not only favorable for InGaN crystal quality, but also necessary to obtain high quality GaN and AlGaN layers, which are often used as barrier or electron blocking layers in real devices. Due to the severe decomposition at high growth temperatures, the tradeoff between indium incorporation and growth temperature turns out to be one of the fundamental limiting factors for high quality InGaN growth.

A remarkable property of the InN/GaN MQWs is that they can be grown at a temperature even higher than 650 °C.^{137,138,142,151,152} If the periodicity is properly designed, the band gap of these high temperature grown InN/GaN MQWs/SLs can be tuned to be equivalent to random InGaN alloys with arbitrarily high In content. Other than the superior crystal quality due to the high growth temperature, the phase separation of InGaN random alloys could be bypassed if the active layers of QWs are pure InN.

Due to the potential superior crystal quality, this chapter focuses on MBE growth of InN/GaN QWs at a high growth temperature of 680 °C. To understand the growth mechanisms in the high temperature range, special attentions must be paid to the following issues.

Indium desorption: Being able to accurately control the surface indium coverage is crucial to understand the QW growth mechanisms. However, the indium coverage is hard to control because the indium desorption becomes pronounced when the substrate temperature is higher than ~650 °C. As a result, to compensate the indium desorption an indium overdose to much larger than 2 MLs is generally needed to ensure the maximum indium incorporation in the QWs.^{137,138} Further, the indium desorption is a complex issue since it is not only a function of substrate temperature but also has a dependence on the coverage. Using RHEED as the investigation tool, E. Monroy et

al.¹⁸⁵ had identified the existence of dynamically stable indium coverage up to ~1.7 ML on the GaN and AlGaIn surfaces, similar to the well known autosurfactant Ga adlayers on GaN surfaces.^{91,92,186} A quantitative relationship between the dynamically stable indium coverage and the desorption rate was also established. However, during the growth of the nominal InN quantum wells the active nitrogen flux is also irradiating the sample surfaces and how the coverage and desorption rates are changed in this more realistic growth scenario is less studied. The difference had been noticed by Yoshikawa et al..¹⁸⁷ Employing in situ spectroscopic ellipsometry, they have observed that the ~2-ML thick indium adlayer desorbs faster under active nitrogen irradiation.

Surface reconstruction: It is widely observed that a “1×3” RHEED pattern quickly appears if indium is co-deposited with active nitrogen on a GaN or InGaIn surface. The “1×3” and the “1×1” RHEED patterns viewed along the $[1\bar{1}00]$ azimuth are compared in Figure 3-1. The “1×3” RHEED pattern is traditionally attributed to an In and N-containing surface structure with a $(\sqrt{3} \times \sqrt{3})R30^\circ$ symmetry (Figure 3-2(a)). However, recent theoretical investigation by Lymperakis et al.¹⁸⁸ suggests that the “1×3” RHEED pattern is produced by a more energetically favorable $(2\sqrt{3} \times 2\sqrt{3})R30^\circ$ reconstruction (Figure 3-2(b)). Considering that the amount of indium, 1/3 ML and 1/4 ML contained in the $(\sqrt{3} \times \sqrt{3})R30^\circ$ and $(2\sqrt{3} \times 2\sqrt{3})R30^\circ$ reconstructions, respectively, reasonably coincides with the indium concentrations of 25-29% found by TEM investigation¹⁴⁹, it is tempting to think that the entire surface reconstruction was frozen into the QWs. Such a claim was first made by Chèze et al.¹⁴⁸ based solely on the observation that a $3 \times$ diffraction pattern appeared on the RHEED screen during the InN QW deposition. In a later TEM investigation, the $3 \times$ ordering of indium atoms along the $[11\bar{2}0]$ direction in the 1-ML thick quantum wells was observed.

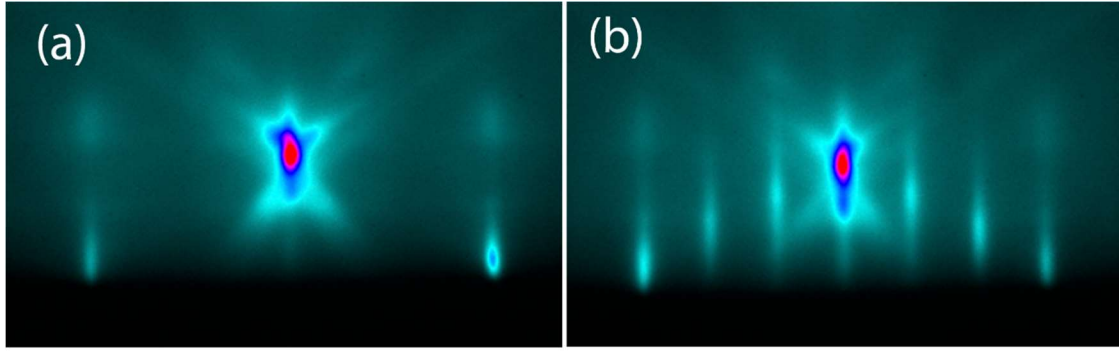


Figure 3-1. The 1×1 (a) and $(\sqrt{3} \times \sqrt{3})R30^\circ$ (b) RHEED patterns viewed along the $[1\bar{1}00]$ azimuth.¹⁸⁹

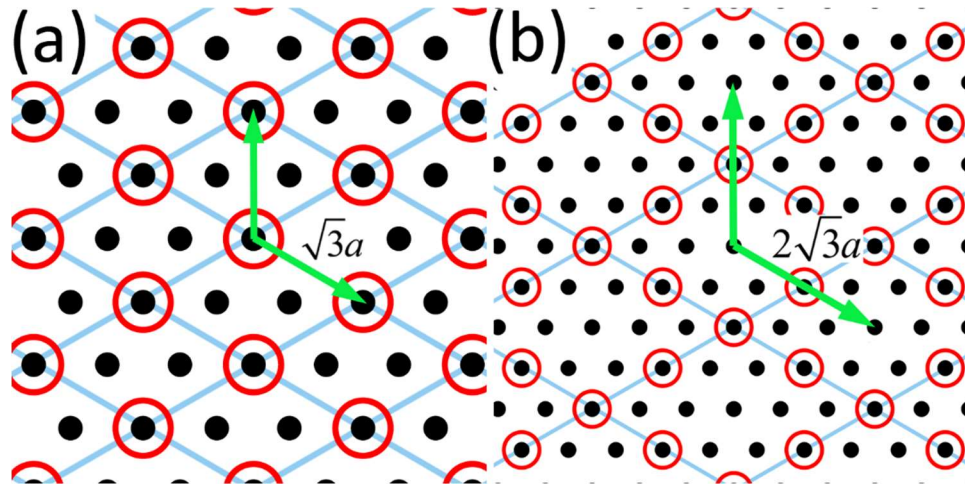


Figure 3-2. The schematics of the $(\sqrt{3} \times \sqrt{3})R30^\circ$ (a) and the $(2\sqrt{3} \times 2\sqrt{3})R30^\circ$ (b) surface reconstructions. The unit cells are indicated by blue lines; the Bravais lattice of GaN(0001) planes is indicated by the black dots; and the arrangement of In atoms is labeled by red circles.

3.2. Growth

The material growths were performed using a Veeco Gen II plasma-assisted MBE (PAMBE) system (Veeco, Plainview, NY, USA) on iron-doped semi-insulating GaN templates (Kyma, Raleigh, NC, USA). The back side of the GaN templates were coated with a $\sim 1\text{-}\mu\text{m}$ thick Ti film to improve the heating uniformity. The system was equipped with a Veeco UNI-Bulb radio frequency (RF) plasma source to generate active N species. For all experiments, the combination

of the RF power of 350 W and nitrogen flow of 0.5 sccm was used to ensure a constant active nitrogen flux which leads to a low temperature GaN growth rate¹²¹ of 0.26 ML/s.

The indium flux of 0.26 ML/s in this work was calibrated at a growth temperature of 350 °C by finding the stoichiometric InN growth conditions, meaning that the active nitrogen flux was equal to the indium flux. This particular InN growth temperature was chosen because it was low enough that both InN decomposition and indium desorption were negligible.⁹⁴ It is worth pointing out that the unit “ML/s” and “ML” used for indium flux and coverage are defined with respect to the Ga-surface site density.

Prior to RHEED investigations and MQW growth, a high temperature GaN buffer was grown at ~770 °C in a Ga-rich condition to ensure good morphology and crystal quality. After buffer growth, the residual surface droplets were desorbed by annealing the sample at the buffer growth temperature with nitrogen flux shuttered. Then the samples were cooled to target temperatures for RHEED investigations or MQW growth.

3.3. The existence of dynamically stable indium coverage

The dynamically stable surface In coverages gives unique opportunity to study the indium adsorption/desorption kinetics by analyzing RHEED intensity transients. In order to demonstrate the existence of the dynamically stable indium coverage, a constant indium flux of 0.28 ML/s was used to impinge the GaN surface at a growth temperature of 710 °C. The deposition time was varied and for each deposition time the RHEED intensity was recorded to analyze the indium adsorption and desorption behavior.

A full RHEED intensity evolution before, during, and after indium deposition was plotted in Figure 3-3(a). The dampening of RHEED intensity is due to the adsorption of liquid-like indium coverage. After shuttering the flux, the RHEED intensity eventually recovered to its original level,

which indicated the complete desorption of indium coverage. The RHEED intensity recovery curves without/with active nitrogen irradiation are summarized in Figure 3-3(b)/Figure 3-3(c). Here the desorption time is defined as the time interval between closing the In shutter ($t = 0$) and the time when 80% of the fully recovered intensity was reached. These are indicated by the dotted lines in Figure 3-3(b) and Figure 3-3(c).

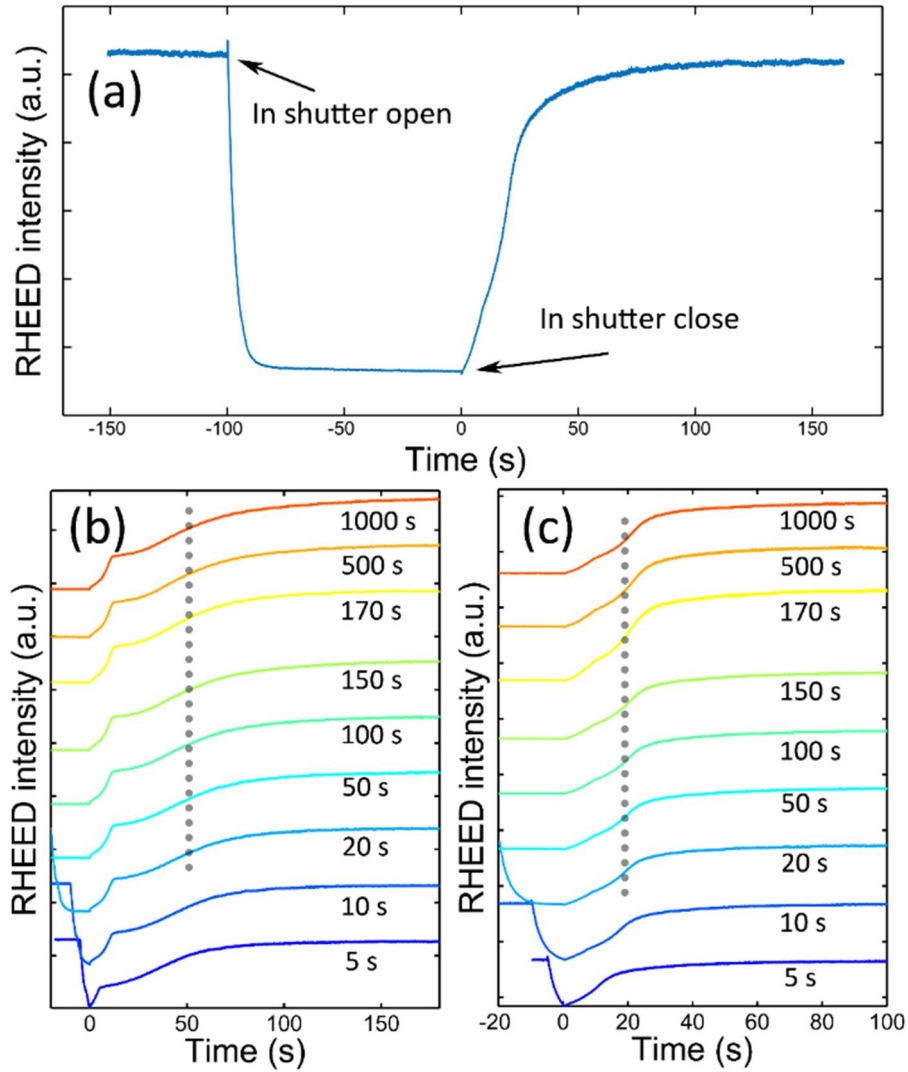


Figure 3-3. (a) The full RHEED intensity evolution corresponding to deposition time of 100 s on the $(\sqrt{3} \times \sqrt{3})R30^\circ$ surface; RHEED intensity transients after In deposition with various deposition times on the (b) GaN 1×1 surface and (c) $(\sqrt{3} \times \sqrt{3})R30^\circ$ surface. The substrate temperature was 710°C and the In flux was 0.28 ML/s. The dotted line indicates 80% of fully recovered intensity.

The main result from Figure 3-3(b) and Figure 3-3(c) is that the desorption time and the shape of recovery curves become independent of the deposition time when the indium irradiation is long enough (> 20 s). The identical recovery curves indicate that before closing the indium shutter there was identical indium coverage on the surfaces. Since this coverage is not increasing with time during indium irradiation, it can be concluded that the impinging rate and desorption rate were the same and, therefore, the coverage was dynamically stable.

3.4. Quantitative determination of the dynamically stable coverage

A method based on analyzing the desorption time is used here to study the relationship between the indium surface coverage and the desorption rate.¹⁸⁵ Without impinging flux, the indium coverage was decaying with time only due to desorption, as is shown in Figure 3-4.

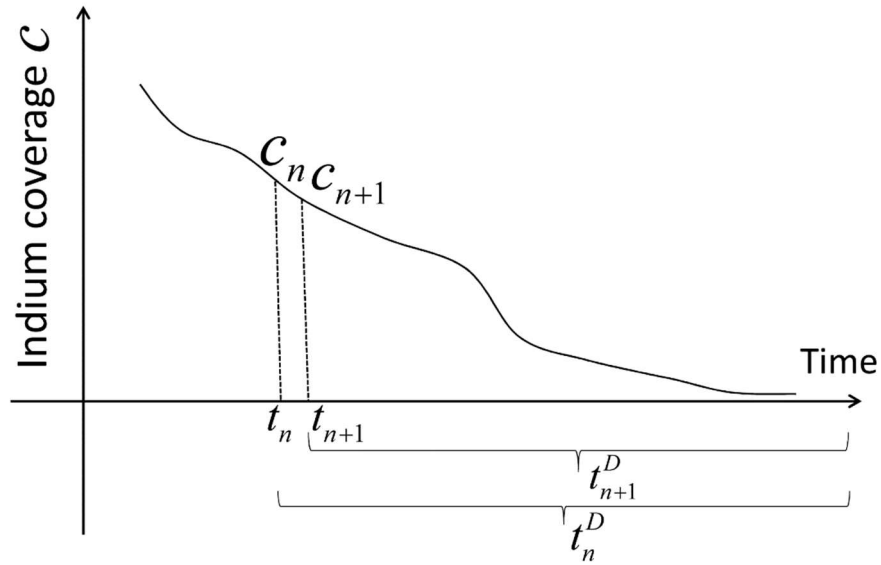


Figure 3-4. Schematic of the decay of indium surface coverage due to desorption.

Then at a given time t the desorption rate $\phi^d(t)$ can be expressed as

$$\phi^d(t) = \frac{dc}{dt} \quad (\text{Equation 3.1})$$

As a result

$$c(\infty) - c(t) = \int_t^\infty \frac{dc}{d\varepsilon} d\varepsilon = \int_t^\infty \phi^d(\varepsilon) d\varepsilon \quad (\text{Equation 3.2})$$

Since the indium coverage would be completely desorbed if the desorption time was sufficiently long, or $c(\infty) = 0$, then

$$c(t) = \int_t^\infty -\phi^d(\varepsilon) d\varepsilon \quad (\text{Equation 3.3})$$

To this point, it can be seen that if the desorption rate $\phi^d(t)$ is known, the desorption curve $c(t)$ can be obtained. From the last section, it is known that for a dynamically stable coverage, the desorption rate ϕ^d has the same magnitude as the indium flux ϕ^i

$$\phi^d = -\phi^i \quad (\text{Equation 3.4})$$

Then Eq. 3.3 can be rewritten as

$$c(t) = \int_t^\infty \phi^i(\varepsilon) d\varepsilon \quad (\text{Equation 3.5})$$

In a real calculation the integration is replaced by a Riemann sum

$$c(t) = \int_t^\infty \phi^i d\varepsilon = \sum_n \phi^i(t_n^\xi) \Delta t_n = \sum_n \phi^i(t_n^\xi) (t_{n+1} - t_n) \quad (\text{Equation 3.6})$$

where $t_n^\xi \in (t_n, t_{n+1})$. Experimentally, the desorption time, t^D , is the measured quantity. From

Figure 3-4 then, it is obvious that

$$(t_{n+1}^D - t_n^D) = -(t_{n+1} - t_n) \quad (\text{Equation 3.7})$$

Finally,

$$c(t) = \sum_n -\phi^i(t_n^\xi) (t_{n+1}^D - t_n^D) \quad (\text{Equation 3.8})$$

It worth noting that both indium flux ϕ^i and desorption time t^D were obtained from experiments, and thus the indium coverage $c(t)$ is determined experimentally.

Two sets of indium adsorption and desorption experiments were performed at 680 °C. For the first set, the nitrogen was not introduced into the growth chamber while for the second set the sample surface was under constant active nitrogen irradiation. Also, for the first set the surface gave an unconstructed 1×1 RHEED pattern throughout the whole experiment. In the latter, a $(\sqrt{3}\times\sqrt{3})R30^\circ$ RHEED pattern quickly appeared as long as the indium shutter was open.

For both surfaces, the specular spot RHEED intensity was monitored along the $[1\bar{1}00]$ azimuth. To maximally eliminate the uncertainty brought by temperature nonuniformity, the two sets of experiments were performed on the same sample successively. In addition, the sample was not rotated throughout the whole experiment to ensure that the electron beam from the RHEED gun was hitting the same position on sample surface all the time.

Special attention must be paid to the deposition times to ensure that the indium surface coverage already reached a steady state before they were measured. Specifically, for experiments on the GaN 1×1 surface, a very large deposition time of 1000 s was chosen when the flux was smaller than 0.02 ML/s. The deposition time of 500 s was found to be sufficient in the flux range between 0.02 ML/s and 0.044 ML/s. For higher fluxes, the deposition time was 100 s. A constant indium deposition time of 100 s was found to be long enough for all fluxes used for experiments on the $(\sqrt{3}\times\sqrt{3})R30^\circ$ surface. Also, the active nitrogen flux was hitting the sample surface for the purpose of simulating the real growth scenario of InN/GaN MQWs. A question that may arise is whether it is appropriate to treat the GaN surface with a $(\sqrt{3}\times\sqrt{3})R30^\circ$ reconstruction as a stable surface like the unreconstructed GaN 1×1 surface, since the $(\sqrt{3}\times\sqrt{3})R30^\circ$ reconstruction is decaying itself. This is valid at the growth temperature of 680 °C due to the exceptional stability of the $(\sqrt{3}\times\sqrt{3})R30^\circ$ reconstruction. This point will be elucidated in detail in the discussion of Figure 3-7.

The RHEED intensity recovery curves are shown in Figure 3-5(a) and Figure 3-5 (b). The indium shutter was closed at time = 0 s. Since the intensity transition to the final plateau, indicating complete desorption of indium, is not sharp, the moments when the 80% of the intensity plateau was reached were defined as the recovery times.

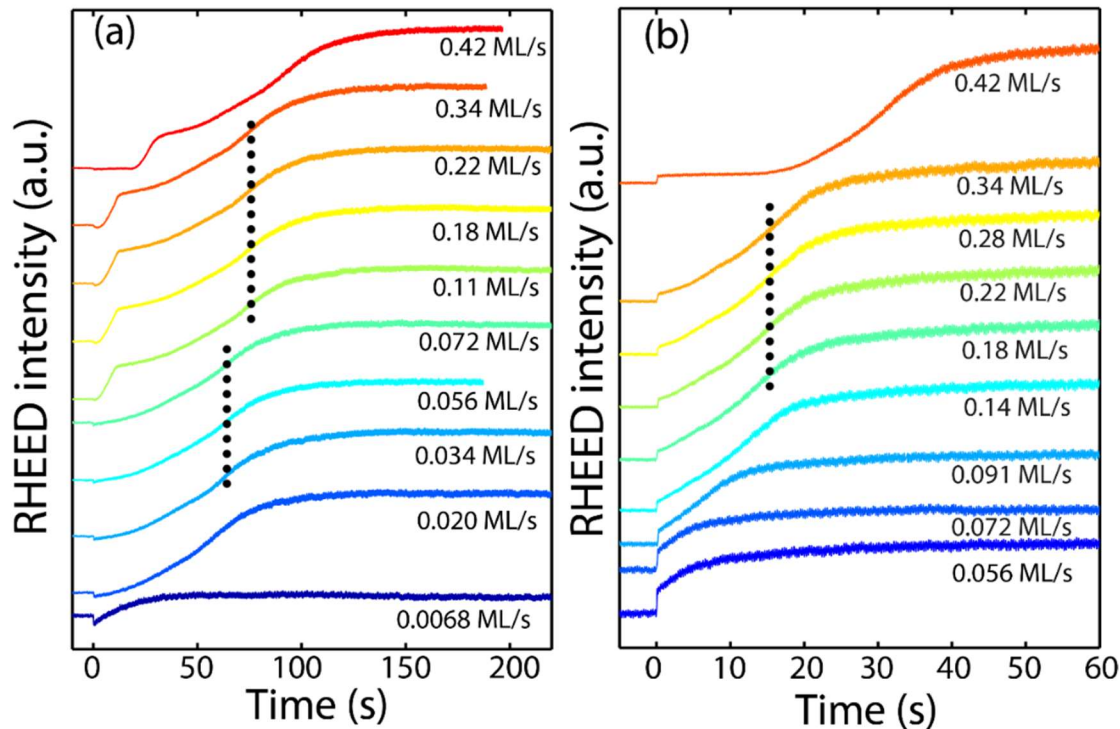


Figure 3-5. The RHEED intensity recorded during the desorption of dynamically stable indium coverages stabilized under various fluxes on a (a) GaN 1×1 surface and (b) $(\sqrt{3} \times \sqrt{3})R30^\circ$ surface.¹⁸⁹ The desorption times of flux windows with nearly constant desorption time are labeled by black dotted lines.

In both Figure 3-5(a) and Figure 3-5(b) there are flux windows in which the desorption time are nearly constant. A main difference is that there are two such windows in Figure 3-5(a) while only one can be found in Figure 3-5(b). Similar to Figure 3-3(a), for the higher flux window in Figure 3-5(a) the desorption is a two-stage process. The duration of the first stage just after the shutter closing is much shorter and the intensity rises at a much higher speed. However, in the

lower stable flux window of Figure 3-5(a), the faster recovery stage is missing and only the slow recovery stage is observed. In sharp contrast, the recovery curves in the one stable flux window of Figure 3-5(b) appeared to be featureless. Nonetheless, for the highest flux of 0.42 ML/s, there appeared a delay before the onset of RHEED intensity recovery for experiments on both the GaN 1×1 and $(\sqrt{3} \times \sqrt{3})R30^\circ$ surfaces. This was the signature of droplet accumulation and the delay was the time needed to desorb these droplets.

Using the method introduced in the last section,¹⁸⁵ the dynamically stable indium coverage was calculated as a function of indium flux and plotted in Figure 3-6(a). The indium coverage increased with the flux in a step-like manner on the GaN 1×1 surface. It increased smoothly at the beginning and eventually reached a plateau of 1 ML. This coverage was maintained until the flux reached 0.081 ML/s. It then jumped to another plateau of 2-ML abruptly and remained stable as long as the indium flux was below 0.34 ML/s. Beyond this critical value, the indium coverage increased with flux without bounds because droplets started to form, which corresponded to the delayed RHEED intensity recovery in Figure 3-5(a). These observations are in good agreement with the results in ref. 185.

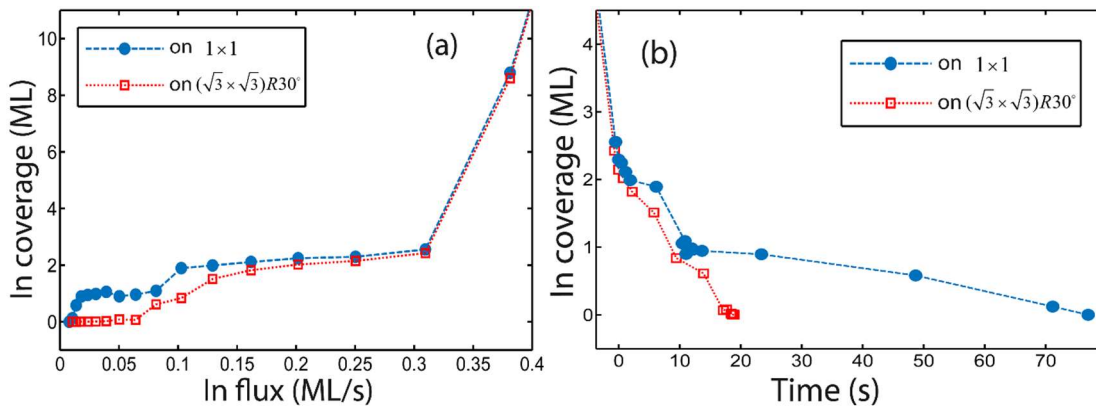


Figure 3-6. (a) Indium surface coverage at 680 °C as a function of impinging indium flux on a GaN 1×1 surface and $(\sqrt{3} \times \sqrt{3})R30^\circ$ surface. (b) The decay of indium surface coverage due to desorption on a GaN 1×1 surface and $(\sqrt{3} \times \sqrt{3})R30^\circ$ surface.¹⁸⁹

By comparing with the flux dependence of recovery curves in Figure 3-5(a), it is immediately clear that on the GaN 1×1 surface, indium fluxes in the high and low stable flux window would stabilize 2-ML and 1-ML indium coverage, respectively. The fast desorption was due to the indium adlayer on the top, while the slow desorption was due to the adlayer that was directly sitting on the GaN surface.

As shown by the red curve in Figure 3-5(a), the dynamically stable indium coverage had a very different behavior on the $(\sqrt{3}\times\sqrt{3})R30^\circ$ surface. The main difference was the lack of the 1-ML flux plateau. The coverage started to be discernable at the flux of ~ 0.056 ML/s, and then eventually reached a relatively stable level of ~ 2 MLs at the flux of ~ 0.18 ML/s. However, the onset of droplets accumulation occurred at the same flux of 0.34 ML/s as is seen on the GaN 1×1 surface.

It should be noted that the method used in this study to extract the indium coverage only works for the dynamically stable coverage. This is because when the droplets start to accumulate the condition $\phi^d = -\phi^i$ (Eq. 3.4) is not satisfied. However, considering that droplets accumulation means the incoming flux is larger than the desorption rate ($|\phi^i| > |\phi^d|$), the calculated indium coverage in the droplet accumulation flux regime can be regarded as the upper bound of the real coverage. An important observation is that the two curves are nearly overlapping when droplets start to accumulate. This strongly suggests that the indium desorption was not affected by the active nitrogen flux any more as long as the formation of top indium adlayer was completed.

With the data in Figure 3-6(a), the decaying curves of indium coverage without impinging flux, corresponding to the schematic in Figure 3-4, was reconstructed and shown in Figure 3-6(b). Due to the smaller y-axis scale in Figure 3-6(b), it is noticeable that the decay starts from a value of ~ 2.4 MLs instead of exactly 2 MLs. This extra indium accumulation resulted in the small but

discernible increase of indium coverage in the 2-ML plateau in Figure 3-6(a). A similar increase had been noticed in RHEED¹⁹⁰ and spectroscopic ellipsometry¹⁹¹ investigations of indium adlayers on GaN 1×1 surfaces. In ref. 191, it was proposed that for both the bottom and top indium adlayer, a critical amount of nucleation is needed to trigger the 2D film growth. Thus, it is reasonable to speculate that the extra ~ 0.4 ML indium is the critical nucleation coverage for 3D droplet formation.

Based on Figure 3-6(b), the desorption rate of the individual indium adlayers on the GaN 1×1 surface and $(\sqrt{3}\times\sqrt{3})R30^\circ$ surface can be roughly compared. For the convenience of discussion, $t_{D,1}^n$ and $t_{D,2}^n$ are used to denote the decaying time during which the indium coverage decreased from ~ 2 MLs to 1 ML and from 1 ML to 0 ML, where the upper index $n = 1, 2$ labels the GaN 1×1 surface and the $(\sqrt{3}\times\sqrt{3})R30^\circ$ surface. Then it is found that the desorption rates of the top adlayer were quite close ($t_{D1}^1 / t_{D1}^2 \approx 1.2$), while the desorption of the bottom layer on the $(\sqrt{3}\times\sqrt{3})R30^\circ$ surface was drastically faster ($t_{D2}^1 / t_{D2}^2 \approx 6.6$). Combined with the fact that before droplet accumulation, the two surfaces had identical indium coverage (~ 2.4 ML) and identical desorption rates (0.34 ML/s), it can be inferred that when the bottom layer was completely sealed by another indium adlayer, the adsorption/desorption kinetics were completely determined by the top adlayer.

The desorption behaviors of the two indium adlayers in the temperature range between 650 °C to 700 °C were compared in Figure 3-7. Since the stable flux window has a dependence on temperature,¹⁸⁵ the indium fluxes used to stabilize the 2-ML In coverage were tested individually for each temperature. Here the flux of 0.14 ML/s, 0.28 ML/s, and 0.28 ML/s was used for 650 °C, 680 °C, and 700 °C, respectively.

For the GaN 1×1 surface, the specular spot RHEED intensity was monitored and the results are shown in Figure 3-7(a). Since the two desorption stages are clearly defined for all three

curves, the desorption time t_D for each adlayer could be easily measured. From the Arrhenius plot of $1/t_D$ in the inset of Figure 3-7(a), the activation energies of 2.91 ± 0.07 eV and 2.67 ± 0.02 eV for the bottom and top adlayers, respectively, were obtained. These activation energies agree well with those reported in ref. 185 (2.7 eV, 2.7 eV) and ref. 191 (2.64 eV and 2.53 eV), with RHEED and spectroscopic ellipsometry as the investigation tools, respectively.

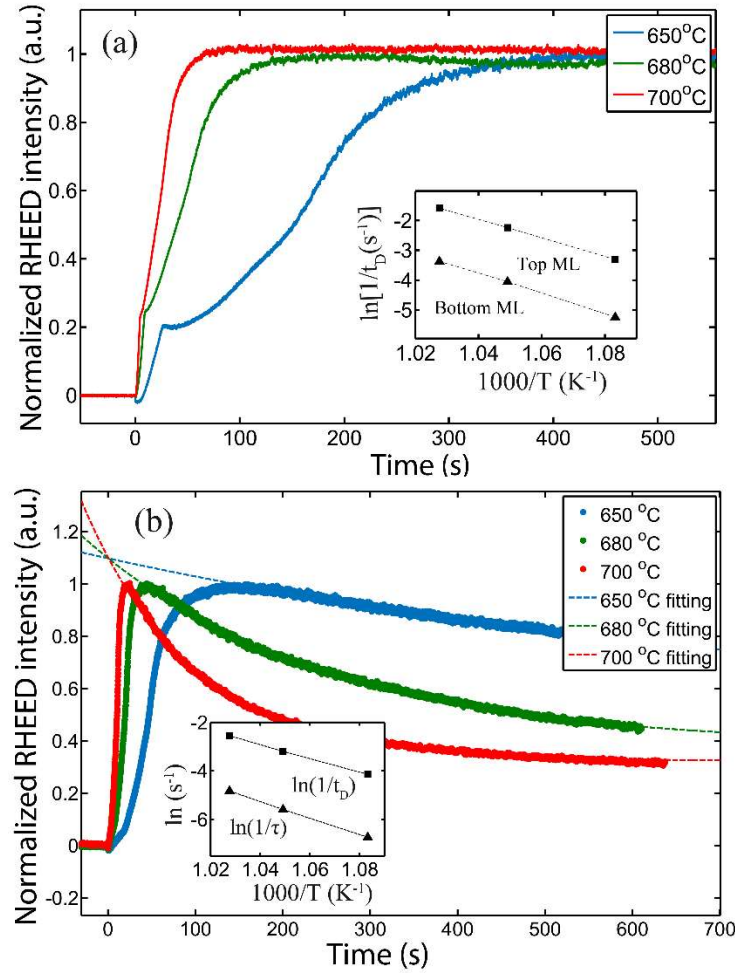


Figure 3-7. (a) Normalized specular spot/streak RHEED intensity transients caused by the desorption of two In adlayers on a GaN 1×1 surface at 650 °C, 680 °C and 700 °C. (b) Normalized RHEED intensity transients of $1/3$ order streak caused by the desorption of two In adlayers and the decay of the $(\sqrt{3} \times \sqrt{3})R30^\circ$ reconstruction at 650 °C, 680 °C and 700 °C. The Arrhenius plots of the inverse desorption times $1/t_D$ of indium adlayers and the inverse of decaying life time $1/\tau$ of the $(\sqrt{3} \times \sqrt{3})R30^\circ$ reconstruction are plotted in the insets in (a) and (b).¹⁸⁹

For the $(\sqrt{3} \times \sqrt{3})R30^\circ$ surface, the 1/3 order streak is a better choice for RHEED intensity monitoring since it is not only sensitive to the desorption of indium adlayers and droplets, but also sensitive to the decay of the surface reconstruction. As shown in Figure 3-7(b), the initial rise of RHEED intensity was due to the desorption of the liquid-like indium adlayers. An exponential decay followed because of the thermal decomposition of the surface reconstruction. Since there is no two-stage feature for the rising part, the desorption time t_d of the two monolayers can only be measured together, which leads to a combined activation energy of 2.46 ± 0.06 eV.

The decaying part can be nicely fitted assuming a single exponential decay

$$I(t) = A \exp(-t / \tau) + B \quad (\text{Equation 3.9})$$

The fitted data yields an activation energy of $1 / \tau$ of 2.94 ± 0.05 eV. The validity of treating the $(\sqrt{3} \times \sqrt{3})R30^\circ$ surface as stable, similar to the GaN 1×1 surface is justified by comparing t_d and τ . At the temperature of 680°C , τ is found to be 267.8 s, vastly larger than two indium adlayer desorption time, $t_d = 24.5$ s.

3.5. Sample growth

In order to study the influence of indium flux and coverage on the formation of InN quantum wells, five samples with different combinations of indium flux and deposition time were grown at 680°C . The sample structure is shown in Figure 3-8(b). For each sample, ten InN quantum wells were grown on a high temperature grown GaN buffer. A 15-nm thick GaN spacer was inserted after each nominal InN active layer growth except that the last InN layer was capped by a 5-nm thin GaN capping layer. The growth procedure, along with the transition of RHEED patterns, is represented in Figure 3-8(a). The nitrogen shutter was kept open throughout the whole growth, while the growth of both the InN well and GaN spacer were controlled by simply opening

the metal shutters. Because of the lagging time of the mechanical shutters, a growth interruption (GI) of 1 s was inserted after each InN layer growth to prevent co-deposition of Ga and In. The nitrogen flux used in this study led to a GaN growth rate of 0.26 ML/s. At the QW growth temperature of 680 °C, the gallium desorption was already nonnegligible and thus a fairly large Ga flux of ~0.35 ML/s was used for the GaN spacer growth to ensure an actual metal-rich growth condition for smooth morphology. The growth time for the ~15 nm spacer was 225 s. After the GaN spacer growth there would be excess gallium droplets on the surface, which, if left unchecked, would prevent indium incorporation in the next QW growth step due to the preferential incorporation of gallium.¹²¹ Therefore, a second GI of 150 s was used after the GaN spacer growth to let the active nitrogen consume the excess gallium.

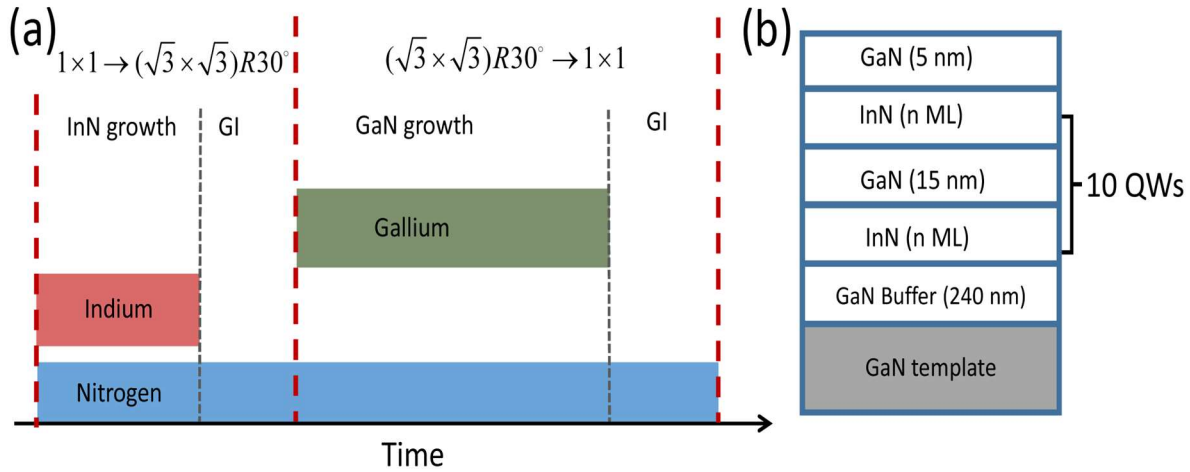


Figure 3-8. (a) The shutter sequence of one InN/GaN growth cycle. The transition of RHEED patterns during different growth stages are labeled on the top. (b) Sample structure of MQWs grown at 680 °C.¹⁸⁹

The indium flux, deposition time, as well as the total indium deposition are listed in Table 3-1. The indium flux of 0.28 ML/s for sample I, II and III are within the window of 2-ML stable indium coverage. For the final two samples, larger indium fluxes in the droplet accumulation regime were chosen.

Table 3-1. Summary of growth parameters of InN/GaN MQWs.

Sample	Total In deposition (ML)	In deposition time (s)	In Flux (ML/s)
Sample I	1	3.57	0.28
Sample II	2	7.14	0.28
Sample III	28	100	0.28
Sample IV	47	100	0.47
Sample V	63	100	0.63

The RHEED intensity evolution during the sample growth was recorded and is displayed in Figure 3-9. For all samples, the RHEED intensity showed a periodic pattern which indicates all growth cycles experienced identical growth processes. Common to all samples, the RHEED intensity dropped immediately after the opening of indium shutter (shutter event A in Figure 3-9) due to the accumulation of liquid-like adlayers. During the GaN spacer growth (between B and C), although having different shapes initially, the samples all reached a stable intensity before closing the Ga shutter. The final stable level corresponds to a surface covered by excessive gallium droplets due to the Ga-rich growth condition intentionally was used, which is evidenced by the delay before the intensity rise during the second GI (after C in Figure 3-9). When the gallium droplets were reduced by active nitrogen to a certain critical amount, the intensity starts going up and finally reached a stable value that was comparable with the level before indium shutter opening (A). This was because all the surface gallium accumulation was completely incorporated into a GaN film.

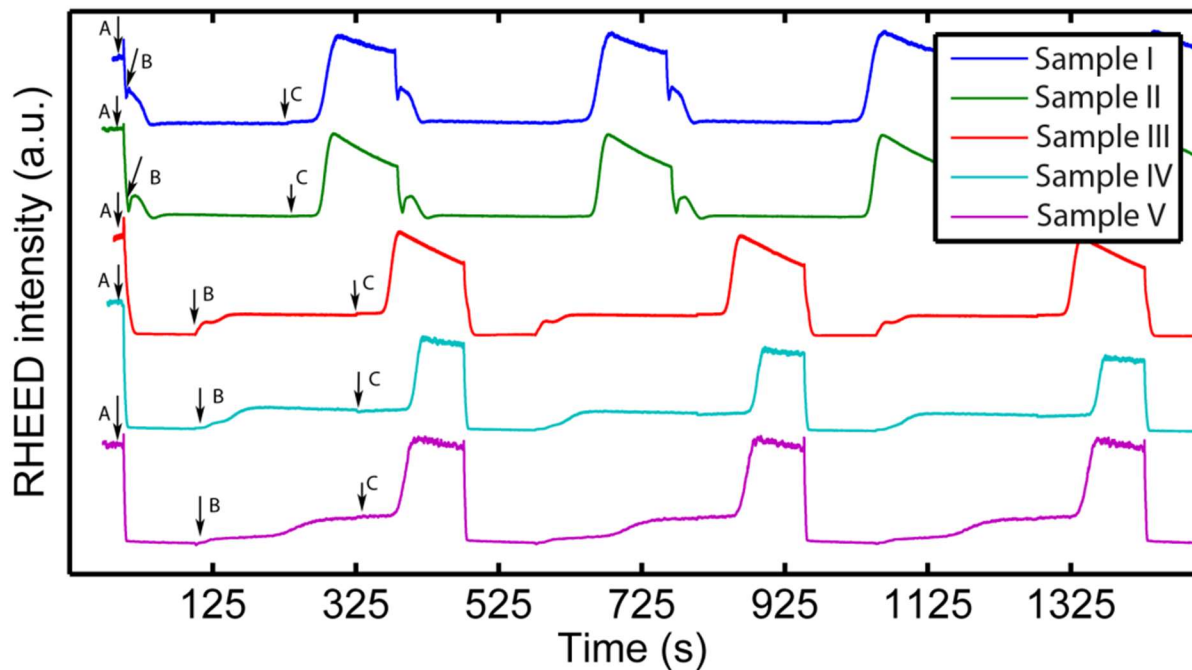


Figure 3-9. Specular spot RHEED intensity evolutions of the first few InN/GaN growth cycles viewed along the $[1\bar{1}00]$ azimuth at $680\text{ }^{\circ}\text{C}$.¹⁸⁹ The shutter events of opening In shutter, opening Ga shutter and closing Ga shutter in the first growth cycle are labeled as A, B and C.

To analyze the difference in growth between the five samples, the time during the indium adsorption stage and GaN capping stage are displayed more closely in Figure 3-10, where the shutter event labels A, B and C have the same definition as in the Figure 3-9. In Figure 3-10(a) all curves are aligned according to the indium shutter opening time (A). For samples I, II and III with identical indium fluxes of 0.28 ML/s , the indium coverage finally reached 2 MLs only for sample III with the longest deposition time of 100 s, which is indicated by the decaying RHEED intensity finally reaching a final stable level. For samples I and II with shorter deposition times, the RHEED intensity decline was interrupted by the incoming gallium flux (labeled by B) and, therefore, the 2-ML stable indium coverage was not established before GaN capping. The increase of the RHEED intensity upon the opening of the Ga shutter was mainly due to the desorption of indium as well as the adsorption of gallium since gallium has a larger reflectivity to electron beam.¹⁹² This

increase is possibly enhanced by the RHEED pattern transition from the $(\sqrt{3} \times \sqrt{3})R30^\circ$ to 1×1 . For sample IV and V, the RHEED intensity saturated more quickly than sample III, which was expected since larger fluxes of 0.47 ML/s and 0.63 ML/s were used. Different from sample III, there were not only the two indium adlayers, but also droplets buildup on the surface when the RHEED intensity was saturated since the fluxes were in the droplet accumulation regime.

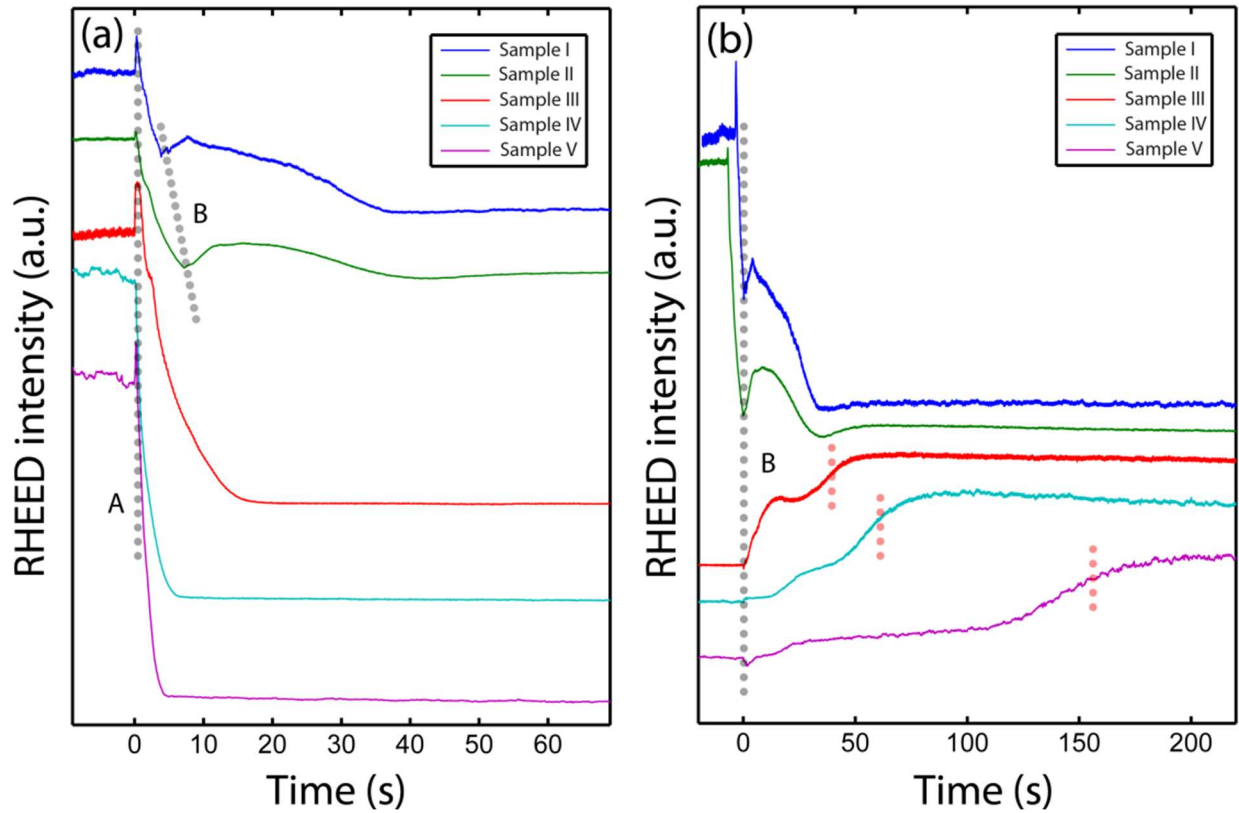


Figure 3-10. Magnified view of the (a) InN deposition stage and (b) GaN capping stage of the RHEED intensity evolutions in Figure 3-9.¹⁸⁹ In (a), all the curves are aligned according to the In shutter opening time (A); in (b) all curves are aligned according to the Ga shutter opening time (B). The definition of shutter events are the same as that in Figure 3-9.

To compare the GaN capping stage, all the RHEED intensity curves were aligned according to the Ga Shutter opening time (B) in Figure 3-10(b). For all samples, the final stable level corresponding to a Ga-droplets-covered surface was reached but in drastically different ways.

As already mentioned in the discussion of Figure 3-10(a), for samples I and II the 2-ML indium coverage was not reached before GaN capping and the intensity dropping was prematurely intercepted by the adsorption of Ga adatoms. For the samples III, IV, and V, the intensity all raised from a relatively low level corresponding to a surface covered by 2 MLs of indium adlayers (sample III) or 2-ML adlayers plus excess droplets (samples IV and V), and finally reached a relatively high level dominated by Ga droplets. The recovery times, defined as the time interval between opening the Ga shutter and the moment that 80 % of the final high level was reached, were indicated by red dotted lines in Figure 3-10(b). For sample III, the immediate intensity rise upon closing of the indium shutter was mainly due to the loss of indium from the two indium adlayers by desorption, which was similar to the desorption behavior in the window of stable coverage in Figure 3-5(a). It was also enhanced by the RHEED pattern transition from $(\sqrt{3} \times \sqrt{3})R30^\circ$ to 1×1 and the high reflectivity of gallium adatoms. The interplay about these mechanisms is a complex issue and brings features to the recovery curves. However, after all the indium was gone and gallium accumulation became significant, the intensity reached the high stable level. Compared to sample III, there was a delay in intensity rise for sample IV, which was caused by extra time to desorb excess indium droplets accumulation since a larger flux of 0.47 ML/s was used. The delay was even longer for sample V, which was expected since the flux of 0.63 ML/s was also the largest among all samples.

It is important to note that the complete desorption of the indium accumulation before the second GI was important. This was because, although gallium is preferentially incorporated, when gallium was about to be fully consumed by the active nitrogen, i.e., the gallium coverage was less than 1 ML, the InGa₂N film formation was still possible. The indium flux and GaN growth time were intentionally designed in this study such that the indium would be completely desorbed

during the GaN growth. This was evidenced by the final stable RHEED intensity level in Figure 3-10(b), as well as the bright 1×1 RHEED pattern, instead of the In-containing $(\sqrt{3} \times \sqrt{3})R30^\circ$ pattern, at the end of second GI.

3.6. Photoluminescence

Samples I to V were characterized by photoluminescence (PL) measurements and the results are summarized in Figure 3-11. The experiments were performed at 10 K using a 266 nm laser excitation, which was focused to spots with a diameter of $\sim 50 \mu\text{m}$. The optical signal from the samples was collected using a liquid nitrogen cooled silicon photodiode array.

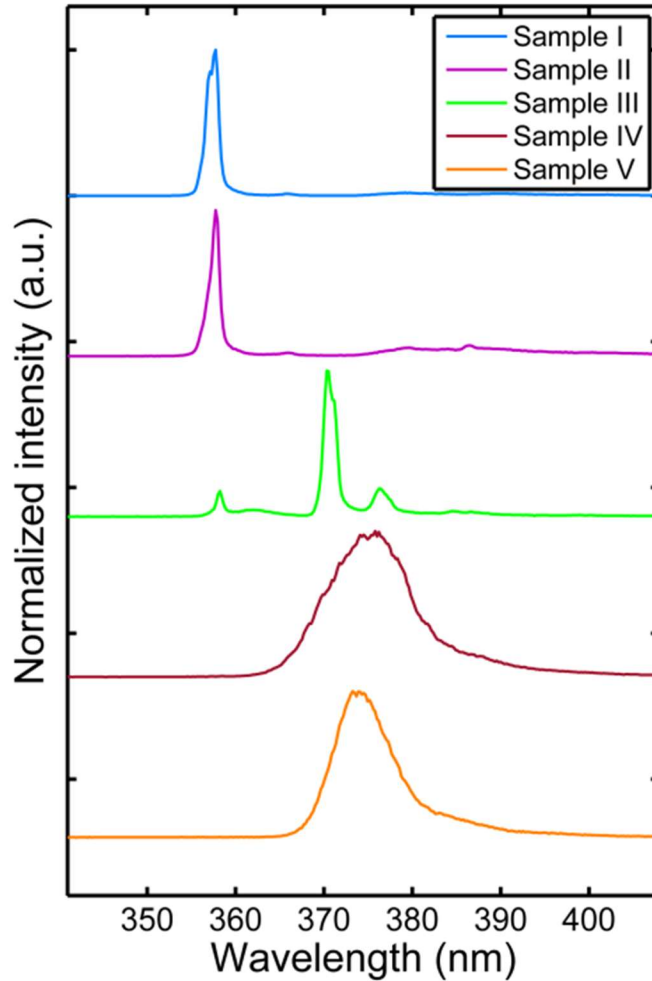


Figure 3-11. Normalized PL intensity of InN/GaN MQWs measured at 10 K.¹⁸⁹

The normalized PL intensities are shown in Figure 3-11. Because only the GaN band edge emission around 357.8 nm was observed, indium was poorly incorporated in samples I and II, which had indium coverages below 2 MLs before GaN capping. For sample III, with ~2 MLs indium coverage when capped, PL emission with wavelength longer than the GaN band edge emission was observed. However, the PL data also showed a large variation over the sample surface. Nonetheless, a representative curve is shown in Figure 3-11. Beside the weak band edge emission, two peaks were found for this specific curve, a stronger one at 370.3 nm and a weaker one at 376.3 nm. Further, for sample IV and V with excess indium droplets before GaN capping, consistent but broader peaks around ~375 nm were observed. The peak positions of sample IV and V agree well with reported values,^{147,151,152} and it can be concluded that they are originated from InN quantum wells with an apparent thickness of 1 ML.

3.7. X-ray diffraction

ω - 2θ scans of the symmetrical (0002) reflection for samples II, IV, and V were carried out to examine the formation of MQWs and the results are shown in Figure 3-12. The two strongest peaks on all spectra are from GaN substrates (left) and AlN seeding layers (right). As can be seen, there is no sign of quantum well formation for sample II with a nominal indium deposition of 2 MLs. This is consistent to the fact that only the GaN band edge PL emission was observed for this sample. In sharp contrast, for samples IV and V with indium droplets accumulation before the GaN spacer growth, the sharp Pendellösung fringes on both sides of the GaN peak could be observed, which indicates MQW formation and is consistent with the PL measurements. Moreover, for sample V, the fringes were less pronounced. This may be attributed to the larger indium droplets size (highest In flux for sample V), which could influence the mass transport of adatoms and thus worsen the interface sharpness.

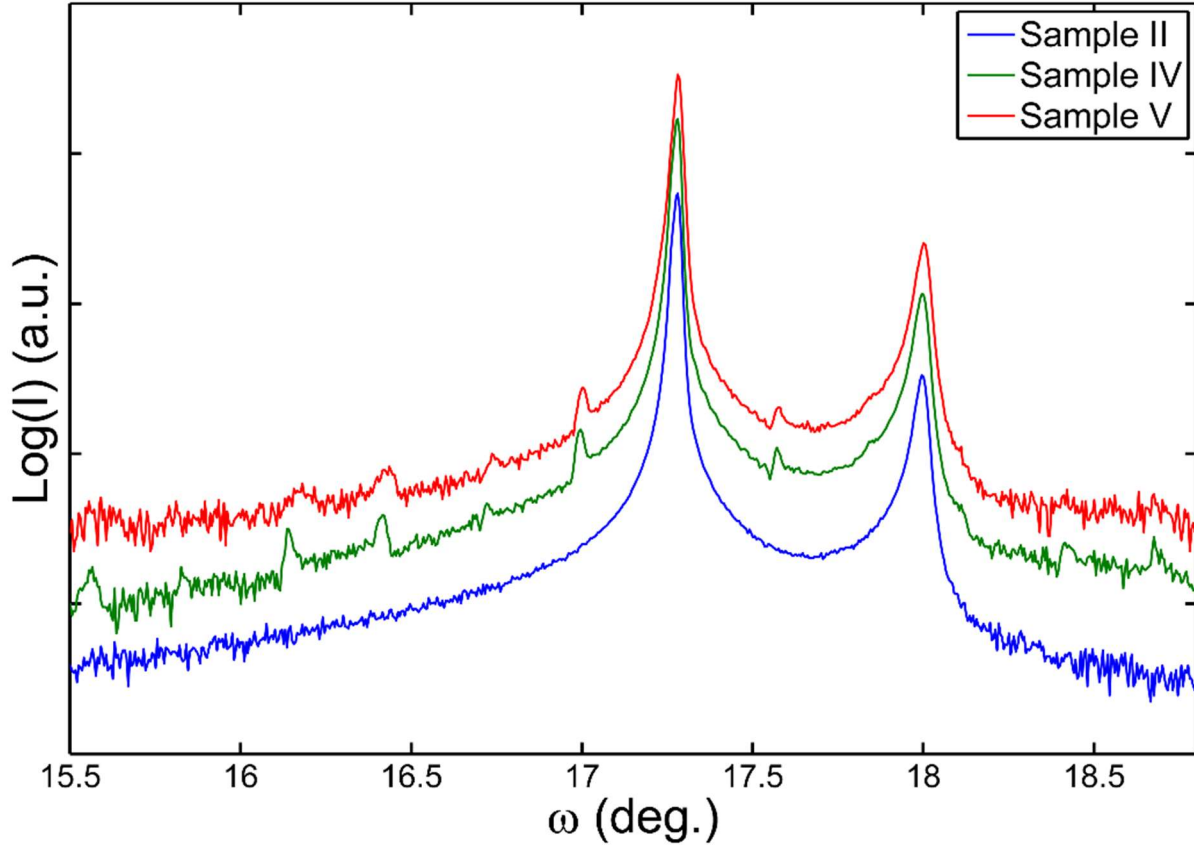


Figure 3-12. ω - 2θ scans of the (0002) reflection of samples II, IV and V.

3.8. Discussion

From previous discussions, the exceptional stability of the In and N-containing $(\sqrt{3} \times \sqrt{3})R30^\circ$ surface reconstruction allows RHEED investigations to confirm dynamically stable indium coverage up to ~ 2 MLs, which is similar to that on the bare GaN 1×1 surface.

The coverage-flux relationship is very different for the two surfaces. The most striking difference is that there does not exist a wide flux window in which a nearly invariant indium coverage of 1 ML is stabilized on the $(\sqrt{3} \times \sqrt{3})R30^\circ$ surface. Also, the desorption rate of the bottom monolayer of indium is much faster on the $(\sqrt{3} \times \sqrt{3})R30^\circ$ surface.

The explanation about the difference in adsorption/desorption kinetics for the two surfaces

requires understanding of the atomic structure of the indium adlayers. However, direct experimental characterization is still lacking. For the GaN 1×1 surface, the structure of the bilayer may be inferred from the STM study of InGaN surfaces.¹⁹³ It was found that an indium bilayer was arranged into a “T1+T4” configuration. The indium atoms in the bottom adlayer directly sat on the underlying Ga/In atoms (T1 position). This was expected since one of the bonds from the Ga/In atoms in the underlying metal layer was dangling and would be paired with one orbital of newly added indium atoms.¹⁹¹ This interaction was strong and thus the indium atoms in the bottom adlayer were forced in registry with underlying Ga/In atoms. Probably due to the weak In-In interactions, indium atoms in the top adlayer were sitting in the T4 sites and triply coordinated with indium atoms in the bottom In adlayer.

For a GaN surface with a $(\sqrt{3}\times\sqrt{3})R30^\circ$ reconstruction, it can be expected that the dangling bonds of the Ga atoms would be involved in forming the surface reconstruction. Therefore, the interaction between the GaN surface and the bottom indium adlayer should be weakened, which would in turn lead to a faster desorption. This explanation is supported by recent first principle calculations.¹⁸⁸ The results suggest that the experimentally observed “ 1×3 ” RHEED pattern should be attributed to a surface reconstruction with a $(2\sqrt{3}\times 2\sqrt{3})R30^\circ$ symmetry, instead of the widely-believed $(\sqrt{3}\times\sqrt{3})R30^\circ$ one. One unit cell is shown in Figure 3-13, underneath a 2×2 nitrogen adlayer, indium atoms substituted certain gallium atoms in the top metal layer of GaN bulk and formed a $(2\sqrt{3}\times 2\sqrt{3})R30^\circ$ structure, which led to an indium concentration of 25%. Due to the existence of the 2×2 nitrogen adlayer, the dangling bonds of the four-fold coordinated metal atoms (indicated by green and blue colors) were used, and, therefore, a weak interaction between this surface structure and the first applied indium adlayer could be expected.

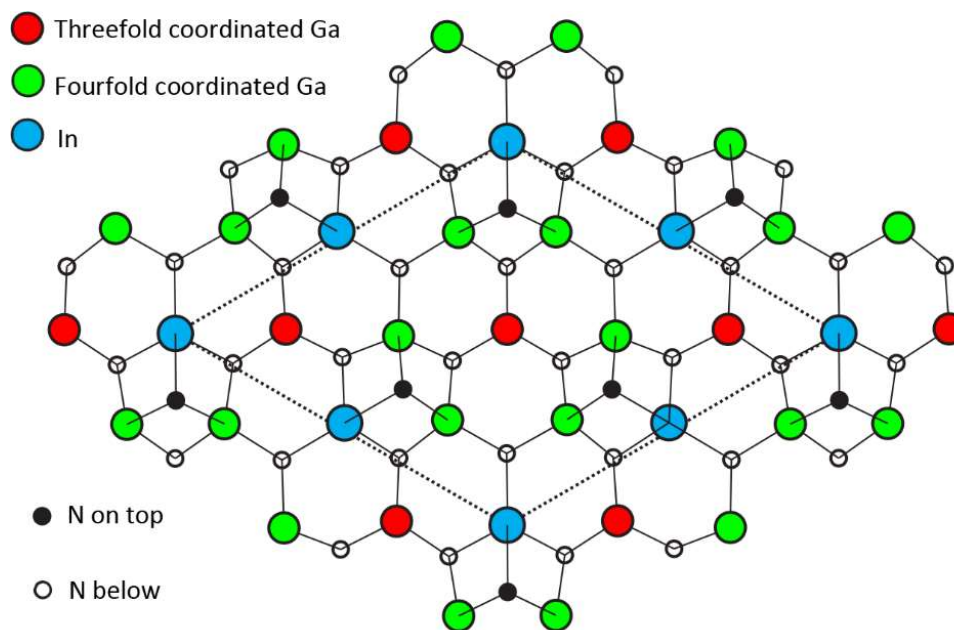


Figure 3-13. The $(2\sqrt{3} \times 2\sqrt{3})R30^\circ$ reconstruction proposed in ref. 188.

Given the fact that InN growth is prohibited when the growth temperature is higher than 500 °C, it can be expected that the In-N bonding is extremely unstable at the chosen growth temperature of 680 °C in this study. As a result, another plausible explanation for the faster desorption on the $(\sqrt{3} \times \sqrt{3})R30^\circ$ surface may be that the In-N bonds served a role like catalysts, which helped the liquid-like indium go into a vapor phase through breaking the In-N bonds.

Despite the fact that the bottom indium adlayer desorbed much faster on the $(\sqrt{3} \times \sqrt{3})R30^\circ$ surface, after the completion of the second adlayer the desorption rates became identical for both surfaces, as if the influence of the surface reconstruction or the active nitrogen flux disappeared. A plausible explanation may be that the top indium layer served as an effective diffusion barrier that the escaping atoms from the bottom layer could not penetrate. As a result, the adsorption and desorption kinetics were completely determined by the top adlayer.

Consistent PL emissions were only observed from sample IV and V, which had excessive

droplet accumulation before the GaN capping. It is known that the droplets keep the integrity of the underlying indium adlayers by compensating the loss from desorption or growth. Therefore, it is reasonable to expect that the consistent QW structure of sample IV and V resulted from a quasi-liquid phase growth, i.e. the growth front was immersed in the two liquid-like indium adlayers. The preservation of the quantum well should be a highly dynamical process which may involve the following process: the diffusion of Ga adatom to the growth front; the formation/dissociation of In-N bonds; the formation/dissociation of Ga-N bonds; and the In-N bonds being replaced by Ga-N bonds similar to what is observed in GaN/AlN superlattice growth.¹⁹⁴ The presence of droplets ensures that the surface is always covered by ~2-ML liquid-like adlayers, which not only ensures that the indium atoms are maximally incorporated but also provides a nearly identical initial condition for all QW growth. As a result, consistent PL showing the largest indium incorporation was observed for samples IV and V.

Inspired by the indium content of less than 33% obtained from TEM studies,^{148,149} it had been suggested in ref. 148 that the entire $(\sqrt{3} \times \sqrt{3})R30^\circ$ adsorbate structure was buried during the GaN capping, even though the only provided evidence was the short appearance of the “1×3” RHEED pattern upon opening the indium shutter. Another supportive observation of this assumption is from the recent TEM study, in which a 3× indium atomic ordering in 1-ML thick QWs was directly observed.¹⁸⁸ Even at the very low growth temperature of 550 °C used in ref. 148, indium overdose to more than 2 MLs was still needed for maximal indium incorporation. This suggests that being immersed in liquid-like indium effectively prevents the indium atoms in the $(\sqrt{3} \times \sqrt{3})R30^\circ$ structure from being substituted by gallium atoms. Nonetheless, the final proof of this assumption needs further understanding in the adsorbate structure as well as the incorporation processes. As another plausible explanation, the first principle simulations of InGa_N film growth

by Lee et al.¹⁹⁵ suggested a strong tendency that the indium atoms would self-assemble into a $(\sqrt{3} \times \sqrt{3})R30^\circ$ pattern, and thus the surface reconstruction is not needed in this process.

3.9. Summary

In summary, to understand the growth mechanism of the InN/GaN MQWs in a high temperature range, this research first focused on the indium adsorption/desorption kinetics during the InN deposition stage. Using RHEED as an in situ monitoring tool, it was found that under active nitrogen flux, the In and N-containing $(\sqrt{3} \times \sqrt{3})R30^\circ$ surface reconstruction quickly appears which further influences the indium adsorption/desorption kinetics. Compared to the bare GaN 1×1 surface, the bottom adlayer desorbs much faster on the $(\sqrt{3} \times \sqrt{3})R30^\circ$ surface and there does not exist a flux window corresponding to a dynamical stable In coverage of 1 ML. However, when the indium coverage becomes larger than 2 MLs, the desorption rates become identical for both surfaces. Finally, the knowledge of indium adsorption/desorption kinetics were applied to MQW growth, and the growth process was understood by analyzing the RHEED intensity evolution during growth. Through PL and XRD characterizations, the important role of In surface coverage before GaN capping was revealed, i.e. in order to insert nominal InN QWs into a GaN matrix at high temperature, the surface should be completely soaked in liquid-like indium adlayers before GaN capping.

Chapter 4: InN/GaN MQW growth at 550 °C

4.1. Introduction

In the last chapter, successful insertion of nominal InN quantum wells was demonstrated at a high growth temperature of 680 °C. Even with excessive InN deposition, the PL emission energy was found only slightly smaller than that of bulk GaN at ~3.3 eV. For the InGaN random alloys, it is well known that growth temperature is the key factor in determining the maximum indium content,¹²¹ as is shown in Figure 1-6. This suggests that growing at a low temperature may be a viable approach to move the PL emission towards the long wavelength region.

Lowering the growth temperature appears to complicate the quantum well structures and the PL emissions. Yoshikawa et al.^{151,152} were the first to report that at a low or intermediate growth temperature (< ~650 °C), the QW thickness can be controlled to 1 ML or 2 MLs if the growth parameters are carefully designed. Compared to the 1-ML thick QWs, the PL emission peaks for the 2-ML thick QWs were found to be redshifted from ~390 nm to ~430 nm.^{151,152} A similar observation was reported in a recent TEM investigation by Dimitrakopoulos et al..¹⁵⁰ As shown in Figure 4-1, despite the possible indium enrichment in the closest neighboring layers, the QW thickness appeared to be either 1 or 2 MLs, with average indium content of ~0.22 or ~0.33, respectively. However, in a more recent temperature dependent study of indium incorporation by P. Wolny et al.,¹⁹⁶ the quantum well apparent thickness never exceeded 1 ML in the growth temperature range between 580 °C to 650 °C, even when large nominal InN depositions of up to 4.3 MLs was used.

In this chapter, the growth phenomena as well as the structural and optical properties of InN/GaN MQWs grown at a low temperature of 550 °C are presented. Compared to the high temperature growth, one particular advantage was that the indium deposition was exactly known

for each QW growth since the indium desorption rate was very small at 550 °C.

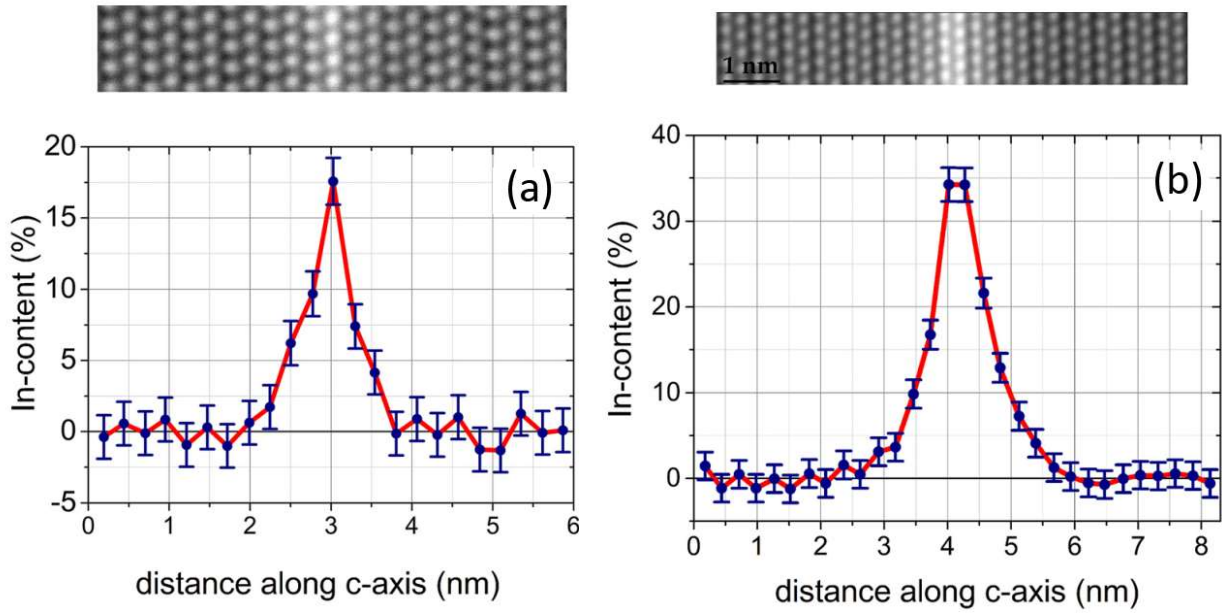


Figure 4-1. InN/GaN quantum wells from ref. 150 with apparent thickness of 1 ML (a) and 2 MLs (b). The top images are noise averaged high resolution scanning transmission electron microscopy (HRSTEM) images. The bottom images are profiles of indium content.

4.2. Growth

All sample growth and RHEED investigation were performed on iron-doped semi-insulating GaN templates (Kyma) in a VEECO Gen II MBE system. A constant nitrogen flux of 0.5 sccm with a RF power 350 W was used to generate nitrogen plasma, which resulted in a GaN growth rate of 0.26 ML/s at low temperature, i.e., temperatures at which the GaN thermal decomposition was negligible. The metal fluxes were provided using thermal effusion cells. The indium flux of 0.26 ML/s was calibrated by finding the boundary of droplet accumulation regime at 350 °C.

The shutter sequence of a full InN/GaN growth cycle and the sample structures are depicted in Figure 4-2(a) and Figure 4-2(b). The introduction of growth procedure will be skipped here since it was similar to the growth at 680 °C. As shown in Figure 4-2(b), GaN spacers of 15 nm

were used to separate QWs. The indium flux of 0.26 ML/s was used to grow QWs with nominal thickness of $n = 1, 3$, and 5 MLs and indium shutter opening times were 4 s, 12 s, and 20 s, respectively. The indium flux and shutter opening times for $n = 0.5$ ML were 0.13 ML/s and 4 s, respectively. The duration of the first GI is 2 s for all samples and the duration of the second GI is 75 s for $n = 0.5$ and 1 ML and 100 s for all other thicknesses. Before lowering to the target growth temperature of 550 °C, a GaN buffer layer of ~240 nm was grown at a high temperature (~790 °C) to achieve good surface morphology and crystal quality.

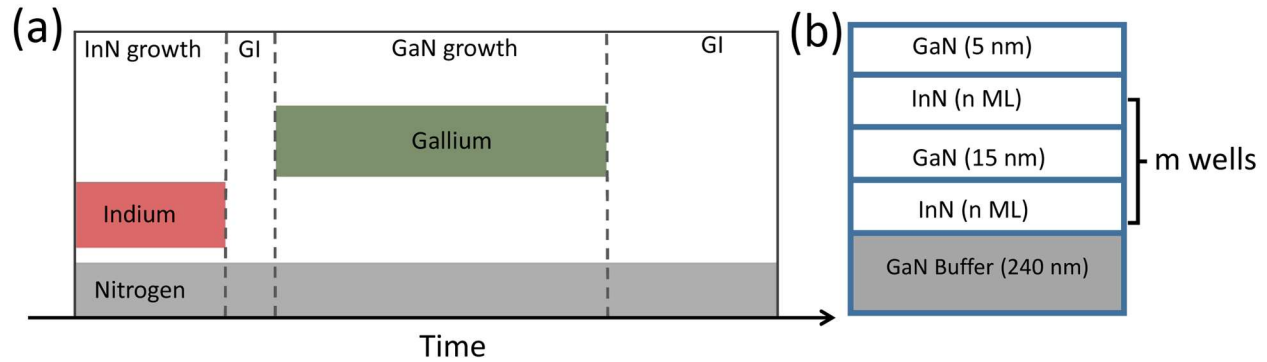


Figure 4-2. (a) Shutter sequence for one InN/GaN bilayer growth. (b) Sample structure.

4.3. RHEED intensity

RHEED investigations were carried out prior to the actual MQW growth. Specular RHEED spot/streak viewed along the $[11\bar{2}0]$ azimuth were recorded during the MQW growth. The nominal InN layer thicknesses under investigation were 0.5, 1, and 3 MLs. Each of the MQW stacks contained 10 repeats of InN/GaN bilayers. Between stacks, a GaN buffer layer was grown at ~790 °C to recover the surface morphology.

During the growth of all test MQW structures, no 3D RHEED pattern was observed, indicating the growths were indeed under metal-rich conditions. Figure 4-3(a) shows the RHEED intensity evolution of MQWs with the nominal InN thickness of 1 ML. The inset in Figure 4-3(a)

is the magnified view of the area in the hollow square frame. The intensity patterns in Figure 4-3(a) were modulated by a dampening envelop which is in sharp contrast to the repeating pattern in Figure 3-9 observed during high temperature growth. To display the fine features more clearly, the second InN/GaN bilayer cycle (shaded area in Figure 4-3 (a)) was zoomed in and shown in Figure 4-3(b).

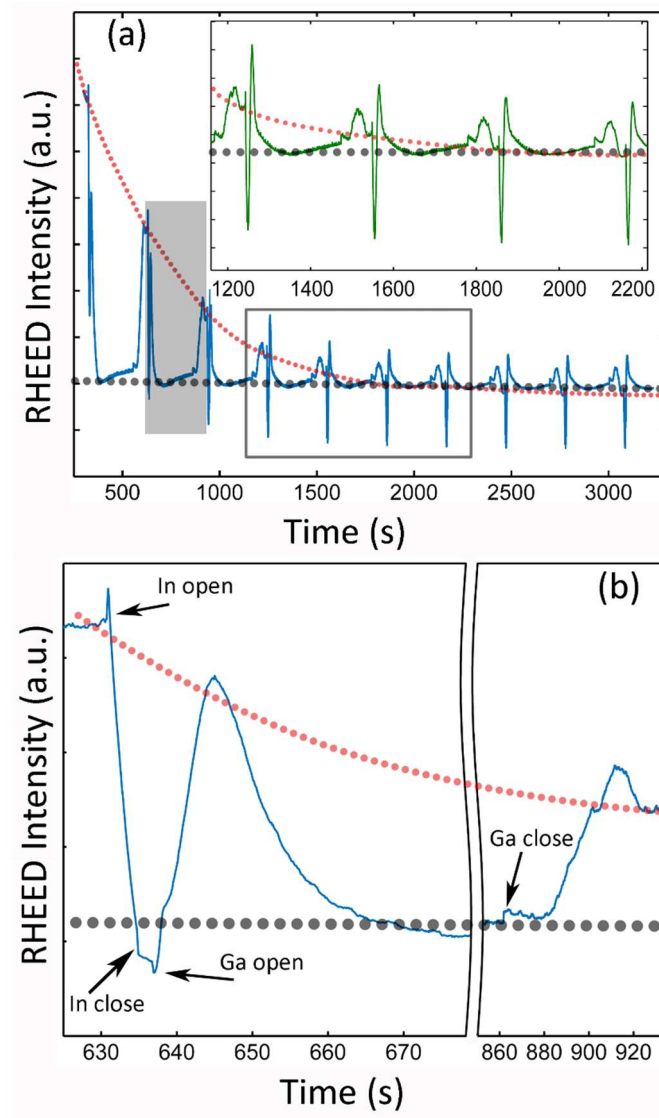


Figure 4-3. (a) RHEED intensity evolution of 1-ML-InN/GaN MQW growth; the inset is the zoomed view of the hollow rectangular area. (b) Zoomed view of RHEED intensity evolution of one InN/GaN bilayer growth cycle (shaded area in (a)). The gray and red dotted lines in (a) and (b) are eye-guides for the evolution of level A and level B.

Different from the well-defined oscillatory behavior, a signature of layer-by-layer growth mode commonly observed in arsenide material growth, the RHEED intensity transient behavior of nitride material growth usually show much more complex patterns, which are often interplays of film growth, liquid-like metal adlayer accumulation, and growth mode transitions, e.g., from layer-by-layer to step flow.^{92,170}

As shown in Figure 4-3(b), except for a noticeable intensity spike upon the opening of the indium shutter, there was an overall decay of the RHEED intensity during the InN deposition stage. The initial spike was confirmed to be caused by physically adsorbed nitrogen adatoms being replaced by newly landed indium adatoms¹⁷² since the high electron density of metal species resulted in a higher reflectivity to electron beams. Given the fact that InN growth is forbidden above 500 °C, the intensity drop after the spike was due to the accumulation of liquid-like indium adlayers.

After being relatively stable during the first growth interruption, the opening of the Ga shutter triggered a dramatic increase in intensity. Based on the observation that a Ga-droplets-covered surface resulted in a higher RHEED intensity level than a In-droplets-covered surface as shown in Figure 3-10, it is proposed that the dominant reason for the RHEED intensity increase upon opening the Ga shutter was the higher electron reflectivity of gallium. This phenomenon is similar to the observation in ref. 192 and ref. 197 of MME (metal-modulated epitaxy) InGaN growth. The simultaneous impingement of Ga and In on an In-wetted surface leads to an intensity spike, which was explained as a combined effect of the completion of a metal adlayer and the larger electron reflectivity of gallium.¹⁹²

Due to the Ga-rich growth condition, continuous liquid-like Ga accumulation would attenuate the RHEED intensity. After the Ga accumulation reached a certain critical amount, the

RHEED intensity was saturated at a relatively stable value, which was indicated by the gray dotted line in Figure 4-3(b). This level corresponded to a GaN surface covered by Ga droplets and a certain amount of indium coverage. As seen in Figure 4-3(a), this level was nearly invariant for all InN/GaN growth cycles. For the convenience of discussion, this level will be labeled as “level A” hereafter.

Similar to the high temperature GaN growth, the intensity recovery after closing the Ga shutter was a two-step behavior. Although it appeared to be stable initially in the first step, the GaN spacer was still growing because the active nitrogen was consuming the excess Ga droplets. When the Ga accumulation was reduced to a critical amount, the recovery entered the second step and an intensity rise was observed. After the Ga accumulation was fully consumed, a new stable level (level B) was finally reached, which is labeled by the red dotted lines in Figure 4-3.

In sharp contrast to the level A which was nearly independent of growth cycles, level B showed an overall decline. Specifically, although dropping drastically, level B was above level A in the initial few growth cycles. During the subsequent cycles it approached a lower level that was even below that of level A. This decline of level B was attributed to the surface indium accumulation. Studies of InGaN growth by MBE^{198,199} have already established that Ga/N ratio is the most crucial factor in determining indium incorporation. A Ga/N ratio larger than unity, the Ga-rich growth condition used in spacer growth, would completely prevent the indium incorporation. As a result, the portion of non-incorporated indium during the nominal InN QW growths would stay on the growth front during the whole GaN spacer growth. Further, the size of this floating indium would increase with each QW growth cycle. This scenario explains the decline of level B.

Two more MQW growths, with nominal InN thicknesses of 3 MLs and 0.5 MLs, were also

investigated and the RHEED intensity evolutions of the initial few growth cycles are shown in Figure 4-4. Although appearing differently at first sight, all the features in Figure 4-3 can find correspondence in Figure 4-4. For $n=3$, the indium accumulated so fast that level B was saturated at the third InN/GaN growth cycle and the saturated level was maintained in all following cycles. It should be noted that the saturated value of level B was lower than level A, which supports the argument that the RHEED intensity rise upon opening the Ga shutter was mainly caused by Ga adsorption. For $n = 0.5$, the dropping of level B was very slow and, thus, the indium accumulation was hardly discernible. However, the indium accumulation could be revealed by RHEED pattern transitions in the following discussions.

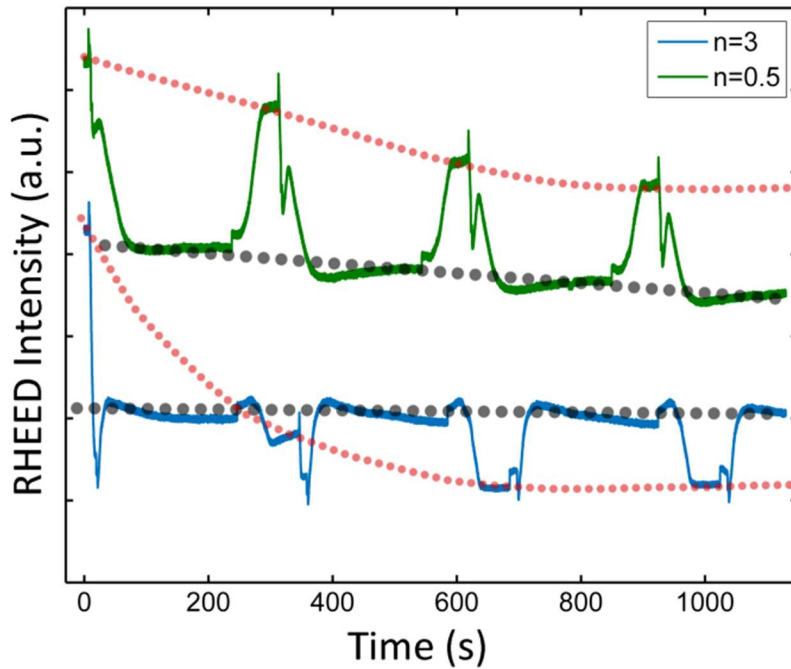


Figure 4-4. RHEED intensity evolution of n -ML-InN/GaN MQWs growth for $n = 0.5$ and $n = 3$. The gray and red dotted lines are eye-guides for the evolution of level A and level B.

4.4. RHEED pattern

In this section, the RHEED pattern transition during different growth stages is analyzed. A

bare GaN surface exhibits an unreconstructed 1×1 pattern after high temperature GaN buffer growth at $\sim 790^\circ\text{C}$. When the substrate was cooled to the growth temperature of 550°C , a very faint 2×2 pattern was typically seen, which may be attributed to a 2×2 nitrogen adlayer.¹⁸⁸ Additional experiments were conducted to investigate the RHEED pattern change when indium was deposited on the GaN surface at 550°C . It was found that a faint “ 1×3 ” pattern, presumably caused by a $(\sqrt{3}\times\sqrt{3})R30^\circ$ surface reconstruction, was identifiable when the indium deposition was $\sim 1/3$ ML. It is worth noting that in MBE system used in this study, this pattern became well defined in temperature range between $\sim 590^\circ\text{C}$ to $\sim 700^\circ\text{C}$.

The RHEED pattern viewed along the $[11\bar{2}0]$ direction during the second growth interruption when level B was reached is shown in Figure 4-5. For MQWs with nominal thickness of 1 ML, although the RHEED intensity was varying as was displayed in Figure 4-3(a), the RHEED pattern maintained as “ $1\times$ ” during the entire first InN/GaN growth cycle. The “ $1\times$ ” pattern also appeared initially during the second growth cycle before level B was reached in the second growth interruption. However, as shown in Figure 4-5, when level B was reached a new RHEED pattern suddenly appeared and survived the whole growth interruption. Although dampened by In adsorption, this new pattern was also observable during the InN growth of the third growth cycle. However, upon opening the Ga shutter for GaN spacer growth, the new pattern immediately switched into a “ $1\times$ ” pattern, only to return later when the level B was reached again. The RHEED pattern transition in the following growth cycles were similar to that during the third cycle. Noticeably, as seen in Figure 4-5, the new pattern became more and more dim as the number of the bilayer growths increased, which echoes the drop of level B in Figure 4-3. For MQWs with nominal thickness of 0.5 ML, the new pattern appeared much slower and was only identifiable from the sixth cycle. For MQWs with a larger thickness of 2 MLs, the new pattern could be seen

even in the first growth cycle. Also, it dampened so fast that it became barely visible from the third growth cycle, consistent to the saturation of level B in Figure 4-4.

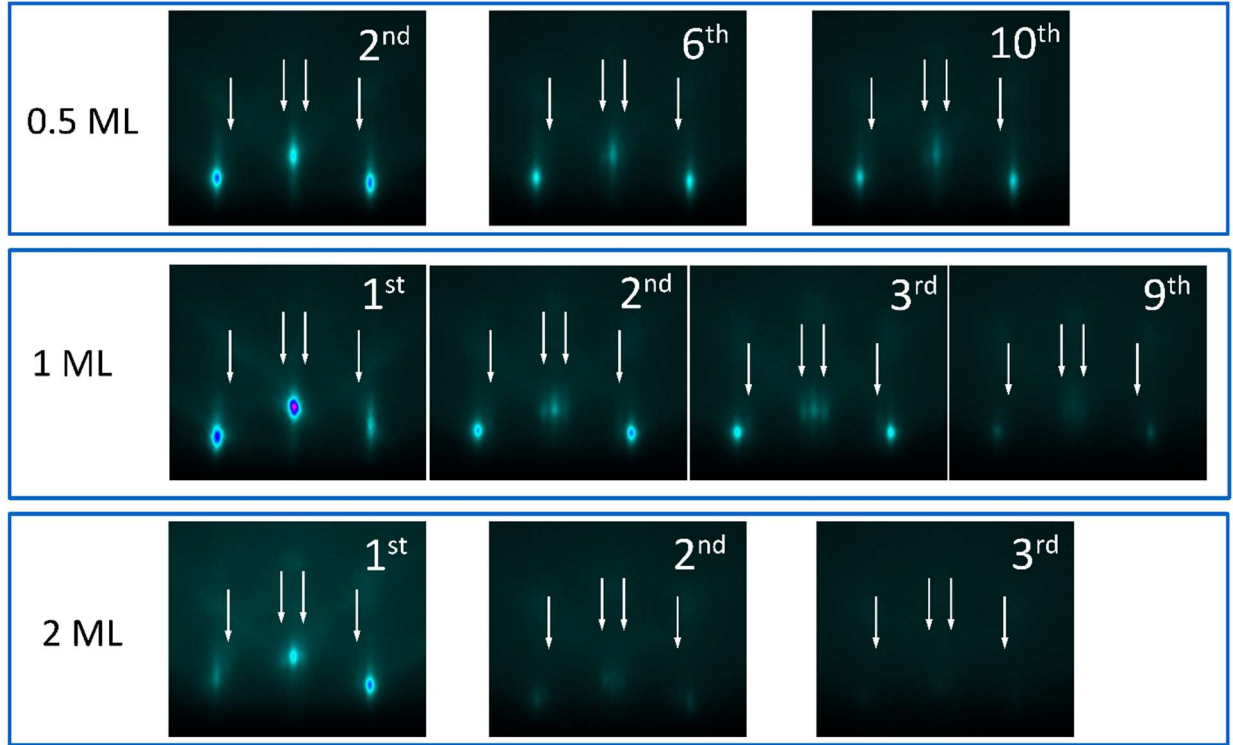


Figure 4-5. RHEED patterns viewed along $[11\bar{2}0]$ azimuth during different InN/GaN growth cycles when level B is reached. The positions of side streaks are labeled by white arrows. The top, middle, and bottom row correspond to nominal InN depositions of 0.5, 1, and 2 MLs.

A distinct feature of the new RHEED pattern was the appearance of side streaks by the main “ $1\times$ ” streaks. A similar pattern had been observed by Smith et al.²⁰⁰ on a GaN (0001) surface at temperatures below 350 °C, as shown in Figure 4-6(a). This has been named the “ $1+1/6$ ” pattern because the distance between the side streaks to the main “ $1\times$ ” streaks is about $1/6$ the distance between main streaks. Following this convention, the new pattern observed in this work is referred as the “ $1+1/7$ ” hereafter due to the fact that the distance between the side streak to the main streak was about $1/7$ the distance between main streaks. Further, the “ $1+1/6$ ” pattern in ref. 200 is

attributed to double scattering between a GaN 1×1 surface and an incommensurate overlayer,²⁰¹ i.e. scattered electron beams by the GaN surfaces/overlayer were scattered again by the overlayer/GaN surface. Also, the side streaks were more intuitively represented as the satellite peaks around the first-order diffraction spots of GaN 1×1 surface in LEED (Low Electron Energy Diffraction) images, as shown in Figure 4-6(b). Further, a very similar “ $1+1/6$ ” LEED pattern was reported by C. Friedrich et al.²⁰² in an ex situ annealing study of fully strained InGaN layers in a high vacuum chamber, as shown in Figure 4-6(c). This pattern started to appear when the temperature was raised to 710 °C under nitrogen plasma.

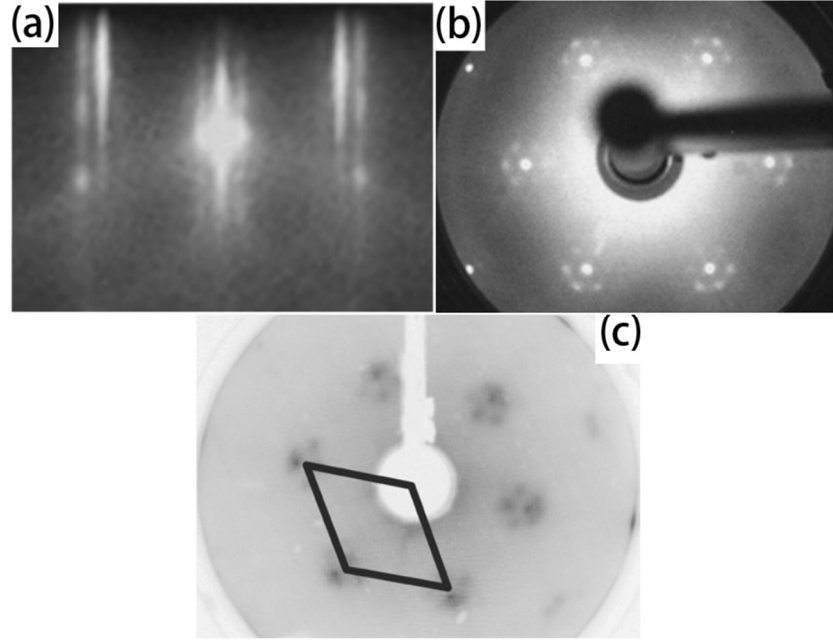


Figure 4-6. The “ $1+1/6$ ” RHEED pattern (a) and LEED pattern (b) caused by Ga adsorption on a GaN(0001) surface at low temperature (< 350 °C).²⁰⁰ The “ $1+1/6$ ” LEED pattern²⁰² obtained by annealing a InGaN sample under nitrogen plasma at 710 °C (c).

The double scattering by two 2D lattices is illustrated in Figure 4-7, which is applied to both RHEED and LEED techniques. Without the loss of generality, it was assumed that the incident electron beam with wavevector of \mathbf{k}_i was scattered by the GaN surface first and then the

overlayer. \mathbf{k}_{o1} and \mathbf{k}_{o2} are the corresponding wavevectors of the scattered beams.

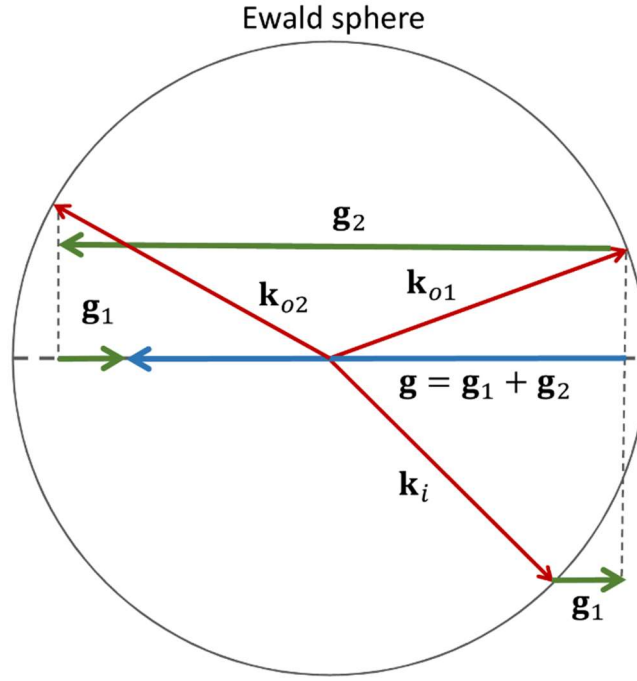


Figure 4-7. The schematic of double scattering process between 2D lattices. (side view)

As was discussed in Chapter 2, the diffraction condition for the first and second scattering are

$$(\mathbf{k}_{o1} - \mathbf{k}_i)_{\parallel} \in \mathbf{G}_1 \quad (\text{Equation 4.1})$$

and

$$(\mathbf{k}_{o2} - \mathbf{k}_{o1})_{\parallel} \in \mathbf{G}_2 \quad (\text{Equation 4.2})$$

where \mathbf{G}_1 and \mathbf{G}_2 are the collection of reciprocal space lattice vectors of the GaN surface and the overlayer, respectively. If $\mathbf{g}_1 \in \mathbf{G}_1$ and $\mathbf{g}_2 \in \mathbf{G}_2$, the direction of doubly scattered beam is determined by

$$(\mathbf{k}_{o2} - \mathbf{k}_i)_{\parallel} \in \mathbf{G}' \quad (\text{Equation 4.3})$$

where elements in \mathbf{G}' have the form $\mathbf{g}_1 + \mathbf{g}_2$ with $\mathbf{g}_1 \in \mathbf{G}_1$ and $\mathbf{g}_2 \in \mathbf{G}_2$.

A set of additional experiments were carried out to gain insight of the origin of the “1+1/7” pattern. First, by following the InN/GaN bilayer growth sequence at 550 °C, the “1+1/7” appeared consistently when level B was reached. However, it could not be reproduced by depositing only In or Ga on the surface, no matter if active nitrogen impingement was present or not. Moreover, at 550 °C the nitrogen flux played a crucial role in the stability of the “1+1/7” pattern. While persisting fairly long under active nitrogen, the “1+1/7” pattern would be immediately gone upon closing the nitrogen shutter. In addition, once gone, the new pattern would not come back if the nitrogen shutter was opened again. The temperature was found to be another key factor influencing the stability of the “1+1/7” pattern. Lower substrate temperatures made it last significantly longer and it even persisted for a long time without the active nitrogen. Compared to the rather faint patterns displayed in Figure 4-5, the “1+1/7” patterns obtained at 520 °C were much more well-defined.

Representative RHEED patterns at 520 °C viewed along $[11\bar{2}0]$ and $[1\bar{1}00]$ azimuth are shown in Figure 4-8(b) and Figure 4-8(e). The white arrows label the identifiable streaks/spots that does not belong to the 1×1 pattern. Considering that in Figure 4-8(b) the side-streaks on the short-wave-vector sides (inner sides) of the first order 1×1 main streaks appeared to be much stronger than that on the long-wave-vector sides, a reasonable guess is that the incommensurate superstructure has the same in-plane symmetry as the GaN 1×1 surface but with a lattice constant that is 1/6 larger. With this assumption, the intensity maxima of the GaN 1×1 RHEED pattern, along with the intensity maximas caused by double scattering, were calculated and presented in Figure 4-8(c) and Figure 4-8(f). Higher order scatterings were not included because their intensities were much weaker. Using the experimental value of electron energy of 16 keV, the

intensity maximas in the simulated results have nearly perfect correspondence to the streaks in the real RHEED image when the incident angle of the electron beams were taken as 4.1° and 4.3° when viewed along the $[11\bar{2}0]$ and $[1\bar{1}00]$ azimuth.

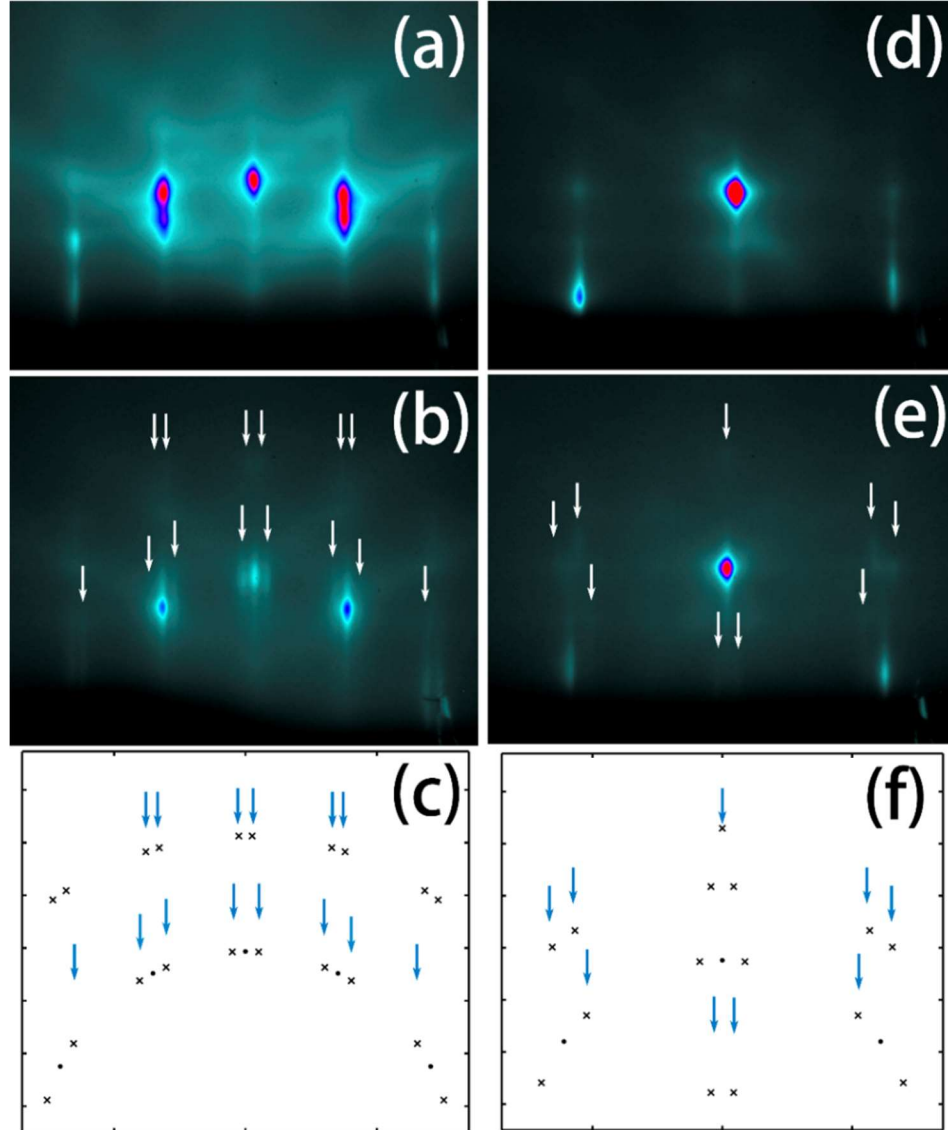


Figure 4-8. (a) and (d): GaN 1×1 RHEED pattern viewed along $[11\bar{2}0]$ and $[1\bar{1}00]$ azimuth after high temperature GaN buffer growth. (b) and (e): The “ $1+1/7$ ” RHEED pattern obtained at 520°C viewed along $[11\bar{2}0]$ and $[1\bar{1}00]$ azimuth with identifiable streaks not belonging to the 1×1 pattern labeled by white arrows. (c) and (f): Simulated electron beam maximas caused by GaN 1×1 surface (dots), and by double scattering between the GaN 1×1 surface and an overlayer with the same in-plane symmetry as GaN and a lattice constant $1/6$ larger (crosses). The blue arrows in (c) and (f) correspond to the white arrows in (b) and (e).

In the MBE system used for this study, the In and N-containing $(\sqrt{3} \times \sqrt{3})R30^\circ$ surface reconstruction became well defined at $\sim 590^\circ\text{C}$, while the “1+1/7” pattern could be observed at $\sim 550^\circ\text{C}$ or lower temperatures. Despite the seemingly different temperature values, this temperature dependence of the surface reconstruction transitions is very similar to what is reported in ref. 202. The “1+1/6” LEED pattern shown in Figure 4-6(c) during annealing of an InGaN sample became visible when the temperature was raised to $\sim 710^\circ\text{C}$. Further heating of the samples to $\sim 760^\circ\text{C}$ under active nitrogen would change the LEED pattern into $(\sqrt{3} \times \sqrt{3})R30^\circ$. It should be noted that the temperatures reported in ref. 202 were too high to keep the bulk InGaN from decomposing. Therefore, it is believed that the temperature difference between this work and ref. 202 was caused by the difference in instruments and experimental setup.

From this comparison, it is believed that the “1+1/7” RHEED pattern observed in this work and the “1+1/6” LEED pattern observed in ref. 202 had the same physical origin. In ref. 202, the LEED pattern was named “1+1/6” instead of “1+1/7” which should be merely caused by the uncertainty in measuring the distance between the satellite spots and the main spots, as can be seen from the rather blurred LEED image in Figure 4-6(c). Auger electron spectroscopy and atomic force microscopy results in ref. 202 suggest that the “1+1/6” LEED pattern was caused by a incommensurate overlayer of group III atoms sitting on an InGaN surface.

It is well known that indium incorporation is not allowed when the flux ratio of Ga/In is large (≥ 1).¹²¹ Since there was a significant amount of Ga surface accumulation after the GaN spacer growth due to the Ga-rich growth condition, it could be expected that during the initial stage of the second growth interruption the film under growth was pure GaN even though there may also be indium accumulation on the surface. However, when the Ga accumulation was about to be completely consumed by the active nitrogen, presumably less than 1 ML, the indium incorporation

became possible. In fact, in many reported growths^{145,151,203} of InN/GaN MQWs/SLs, the second growth interruption in Figure 4-2(a) was broken into two stages in order to prevent the formation of InGaN layers. Using the fact that indium has a higher vapor pressure compared to Ga, the nitrogen shutter was closed during the first stage so that the indium was thermally desorbed with the protection of Ga. Then, the nitrogen shutter was opened to consume the remaining Ga during the second stage. However, this strategy was not used in this study because at the growth temperature of 550 °C, the indium desorption rate was very small which would lead to an unreasonably large desorption time. As a result, it can be concluded that in this study the “1+1/7” pattern appeared during the second GI was caused by an incommensurate indium layer on an InGaN film.

The InGaN layer without being capped by GaN was not stable at 550 °C. The immediate disappearance of the “1+1/7” pattern upon shuttering the active nitrogen flux indicated that the InGaN film was experiencing a decomposition which involved losing nitrogen atoms. This is supported by the STM studies of InGaN surfaces.^{193,204,205} It is found that indium atoms in the topmost layer of a InGaN film tend to bond to each other directly by losing the underlying nitrogen atoms when they are close to each other. In this way, the strain caused by the larger size of the indium atoms is relieved. As a result, it can be expected that under active nitrogen the surface InGaN layer has a strong tendency to segregate into pure indium and GaN.

4.5. Photoluminescence

MQW samples with different combinations of nominal InN thickness (n-ML) and QW repetitions (m) were grown and the PL results were summarized in Figure 4-9. Instead of a continuous redshift, Figure 4-9(a) shows that increasing the nominal InN thickness to be equal to or greater than 2 MLs would lead to a saturation of emission peak at ~423 nm. The energy of this

saturated peak is nearly coincident with the PL emission energy from MQWs with an apparent thickness of 2-ML, as reported in the studies by Yoshikawa et al..^{151,152} Also, for those samples with a nominal InN thickness of 1 ML, the emission peak fall into the range between 390 nm to 400 nm, which is in good agreement with the reported PL emissions from QWs with an apparent thickness of 1 ML.^{142,148,151,152,206}

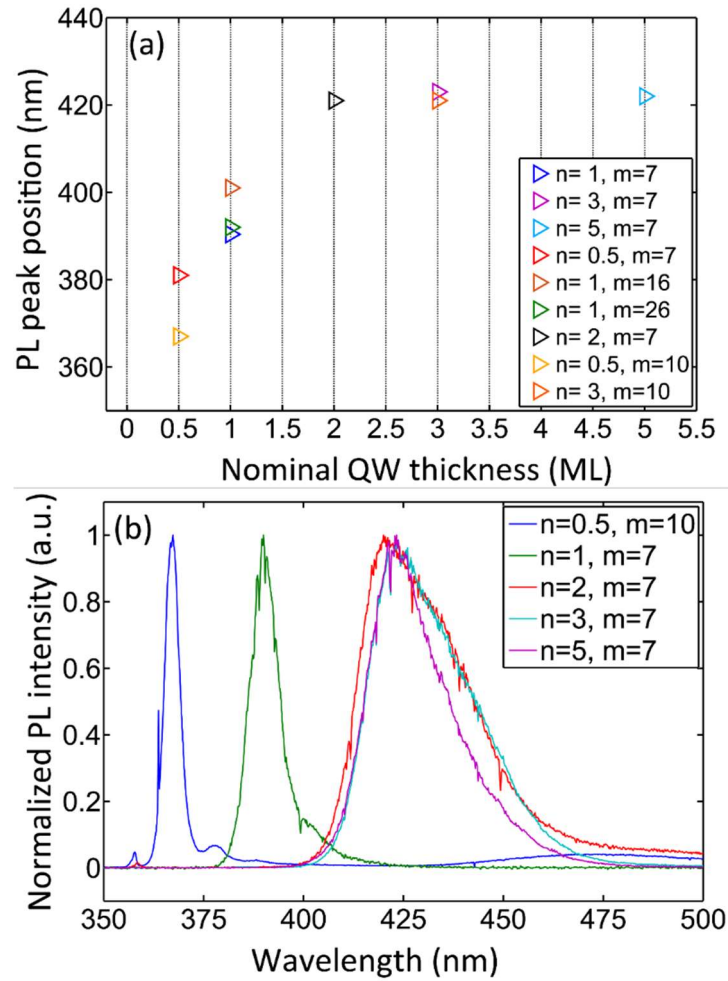


Figure 4-9. (a) Summary of PL emission peaks of MQWs with different combinations of nominal InN thickness (n-ML) and numbers of QWs (m). (b) Representative PL curves for samples with various nominal thickness (n-ML).

The PL spectra shows a large position dependence over the sample surface when the nominal InN deposition was 0.5 ML. Nonetheless, a representative PL spectrum is shown in Figure

4-9(b). In addition to a weak main emission peak and side peaks in the range between 360 nm and 380 nm, the band edge emission of GaN (357.8 nm) and a broad yellow band emission are typically observable. These observations point to a possibility that the small InN deposition of 0.5 ML leads to a sheet-like quantum well structure with a large sheet-size inhomogeneity.

4.6. X-ray diffraction

Figure 4-10 summarizes the ω - 2θ scans of the (0002) reflection of MQW samples with total QW number $m = 7$. Same as Figure 3-12, the two strongest peaks on the left and right were caused by the GaN substrates and AlN seeding layer, respectively. For all samples, the formation of QWs was clearly seen from the well-defined interference fringes. An indium induced peak at 16.47° was observable for the sample with nominal thickness of 2 MLs and this peak became more pronounced for the sample with the largest nominal thickness of 3 MLs. This observation was consistent with the faster drop of level B with larger nominal InN thickness in the discussion of Figure 4-3 and Figure 4-4.

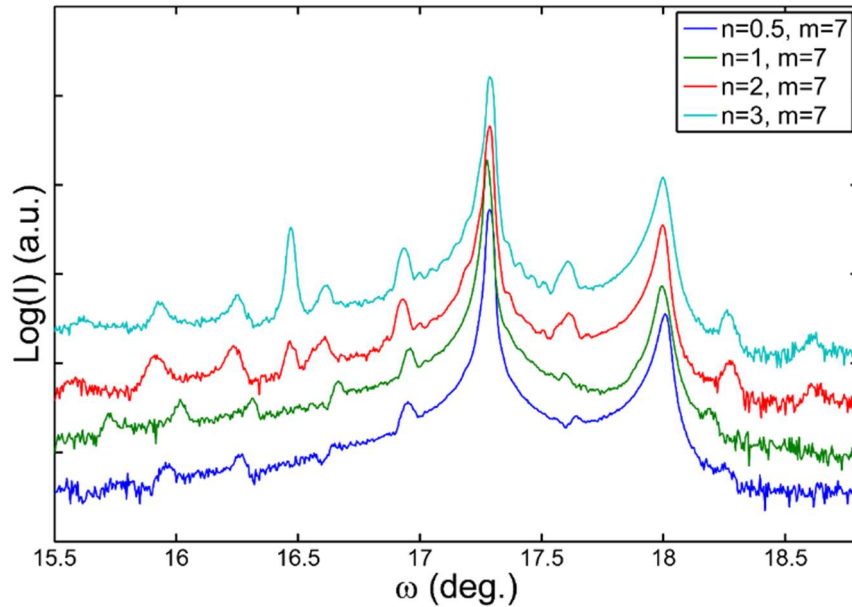


Figure 4-10. ω - 2θ scans of the (0002) reflection of samples grown at 550°C with nominal thickness of n -ML and total QW number (m) of 7.

4.7. Transmission electron microscopy

The formation of MQWs were investigated by cross-sectional transmission electron microscopy (TEM) measurements. As is shown in Figure 4-11(a) and Figure 4-11(b), for samples with nominal InN thickness of 1 ML and 3 MLs, the formation of atomically abrupt quantum wells were clearly seen. The quantum wells appeared to be continuous and the GaN spacer layers were ~14-nm thick. For both samples, the apparent thickness did not exceed 2 MLs, which was consistent with the PL saturation behavior in Figure 4-9(a).

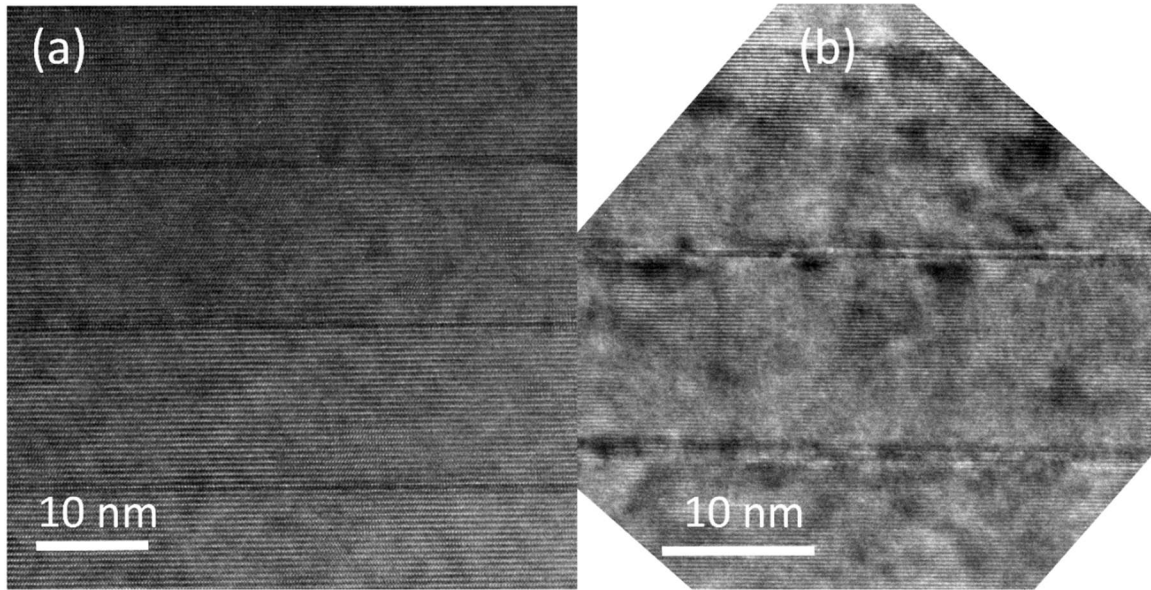


Figure 4-11. Cross-sectional high resolution TEM images of MQWs with nominal InN deposition of (a) 1 ML and (b) 3 MLs.

4.8. Theoretical calculation of band structures

The band gap of a 1- or 2-ML thick InGa_N quantum wells as a function of indium content was calculated using the eight-band **k.p** method and the results were plotted in Figure 4-12. A good match of experimental data, 3.27 eV and 2.92 eV for 1-ML and 2-ML thick QWs, respectively, was found for In content of 43%, and therefore the E-k dispersion of the In_{0.43}Ga_{0.57}N/GaN QWs were plotted in Figure 4-13. It should be noted that an In content of 0.43

is substantially larger than the values ≤ 0.33 obtained from TEM measurements.^{148–150,196} The reason for this discrepancy is not understood yet. In eight band **k.p** calculations the bulk band gap of InGaN is treated as an input parameter. In this work, the InGaN bulk band gap was calculated using a universal bowing parameter of 1.36 eV,²⁰⁷ which is known to cause band gap overestimation when the In content is low.²⁰⁷ Thus, it can be expected that the fitted In content would be lower if the InGaN bulk band gap was calculated more accurately. Further, the errors may be caused by the uncertainty in evaluating the strain effect on band gap. The strain has a large influence on the InGaN band structures. As an example, the comparison of the valence band structure between the strained and unstrained $\text{In}_{0.43}\text{Ga}_{0.57}\text{N}$ bulk is shown in Figure 4-14. However, there is still a lack of agreement on the values of deformation potentials and a large scattering of reported values can be found in the literature.^{144,179,208} Also, the deformation potential values are further complicated by the large compositional dependence.^{144,179}

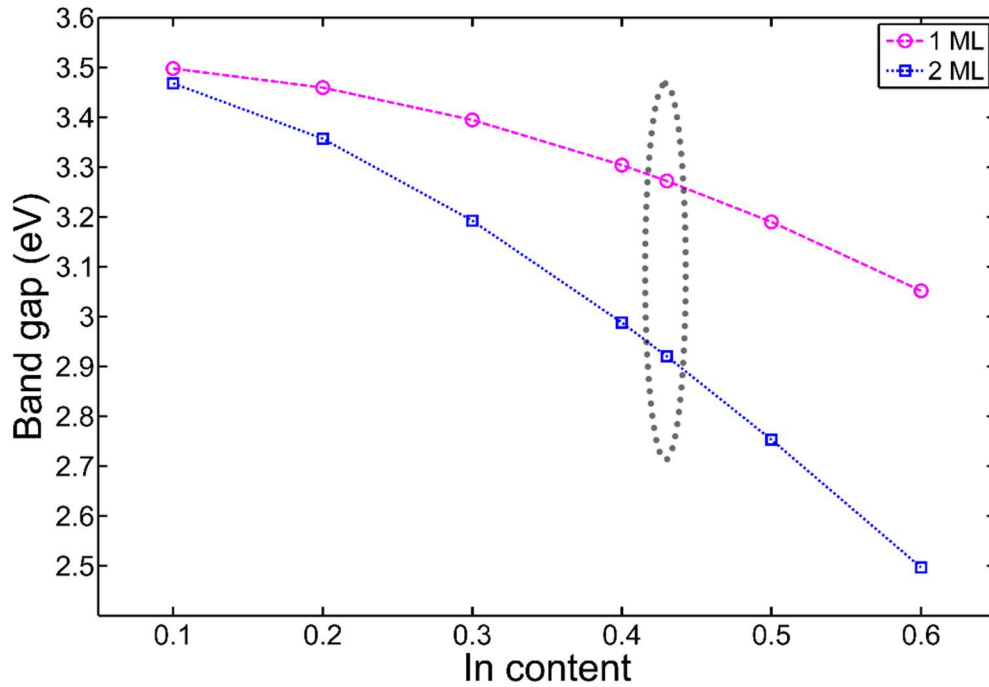


Figure 4-12. The band gap of 1-ML and 2-ML thick InGaN/GaN QWs as a function of In content.

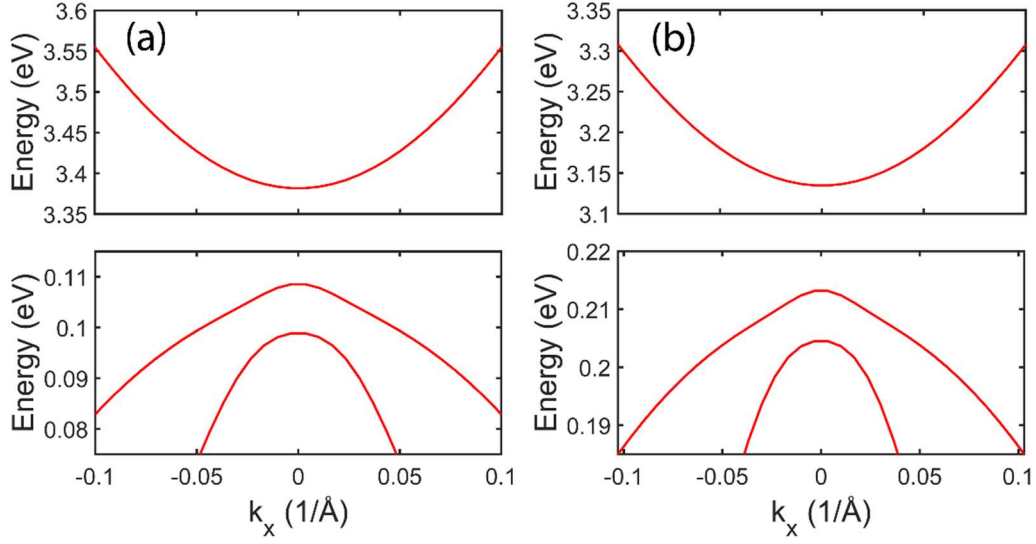


Figure 4-13. The energy dispersion of 1-ML (a) and 2-ML (b) thick $\text{In}_{0.43}\text{Ga}_{0.57}\text{N}/\text{GaN}$ QWs.

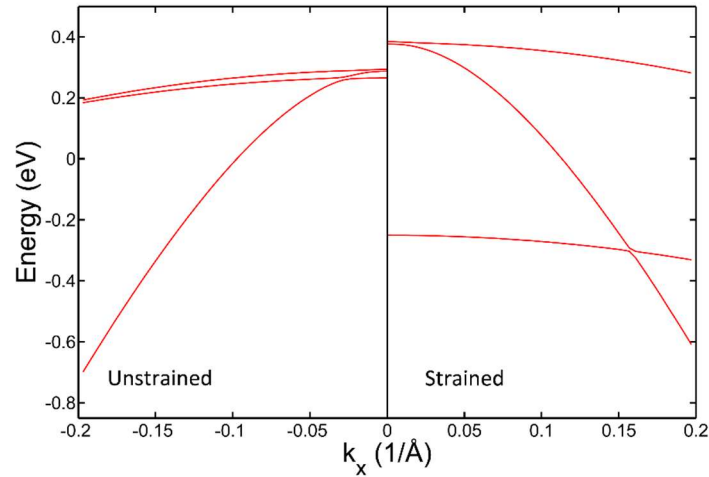


Figure 4-14. The comparison between the strained and unstrained valence band structure of $\text{In}_{0.43}\text{Ga}_{0.57}\text{N}$ bulk.

Due to the extremely small thickness, the band gap shrinks very slowly for the 1-ML-thick quantum wells. At In content of 43%, the band gap only reduced by 0.24 eV, whereas the bulk $\text{In}_{0.43}\text{Ga}_{0.57}\text{N}$ band gap was ~ 1.9 eV, corresponding to ~ 1.6 eV reduction in bulk band gap. Compared to the 1-ML thick QWs, the 2-ML thick QWs showed a much more pronounced quantum confinement. The band gap was smaller at all In contents and the energy difference

became larger when the indium content increased.

To gain further insights of the band edge states of 1- and 2-ML thick $\text{In}_{0.43}\text{Ga}_{0.57}\text{N}/\text{GaN}$ QWs, the probability densities of individual bands, here defined as $|F_n(\mathbf{r})|^2$, are shown in Figure 4-15 and Figure 4-16. Since in the Hamiltonian Eq. 2.35 the conduction band is only directly coupled to the $|Z\rangle$ valence band states at $\mathbf{k} = 0$, the conduction band edge of quantum wells was dominated by the $|1\rangle$ and $|5\rangle$ states (the $|S, \uparrow\rangle$ and $|S, \downarrow\rangle$ states), with a noticeable mixture of the $|4\rangle$ and $|8\rangle$ states (the $|Z, \uparrow\rangle$ and $|Z, \downarrow\rangle$ states). As shown in Figure 4-15(a), for the 1-ML thick QWs the quantum confinement was very weak, the possibility distribution extended in a region over ~ 6 nm in sharp contrast to the QW thickness of ~ 0.28 nm. Although showing a stronger confinement as in Figure 4-16, the electron band edge wavefunctions of the 2-ML thick QWs were still highly extended, distributed in a region ~ 4 nm wide.

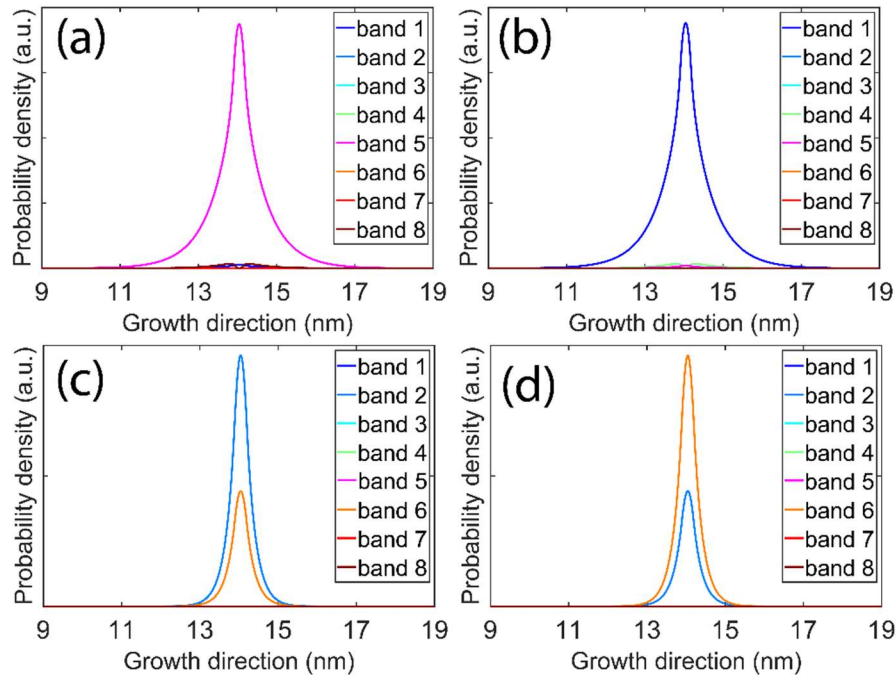


Figure 4-15. The probability densities of band edge states for 1-ML thick $\text{In}_{0.43}\text{Ga}_{0.57}\text{N}/\text{GaN}$ QWs. (a) and (b) are the two degenerate conduction band edge states. (c) and (d) are the two degenerate valence band edge states.

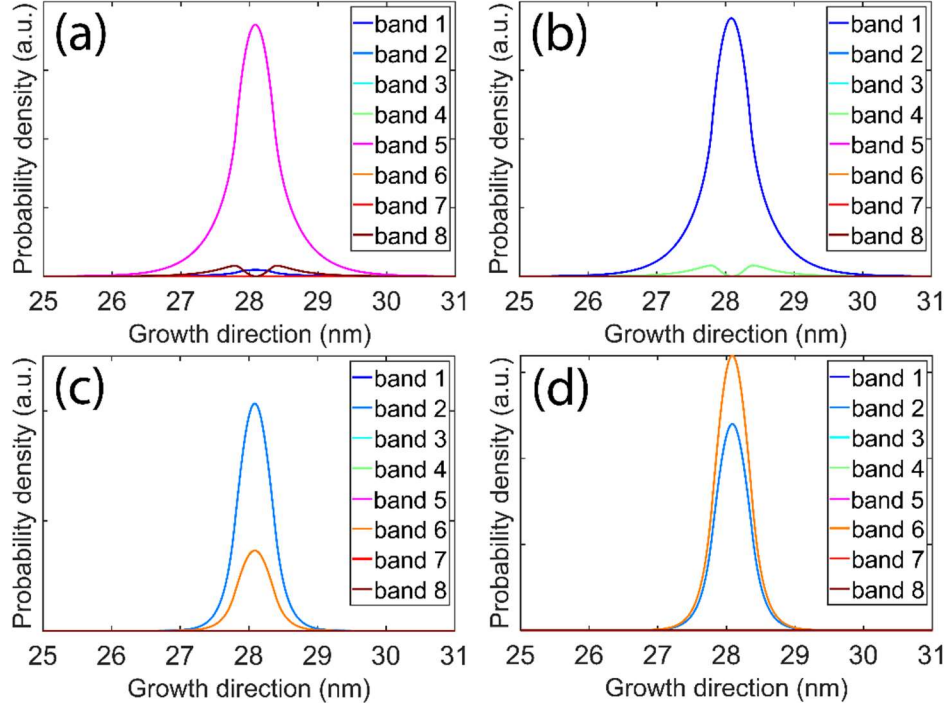


Figure 4-16. The probability densities of band edge states for 2-ML thick $\text{In}_{0.43}\text{Ga}_{0.57}\text{N}/\text{GaN}$ QWs. (a) and (b) are the two degenerate conduction band edge states. (c) and (d) are the two degenerate valence band edge states.

The top valence band at $\mathbf{k} = 0$ were pure $|2\rangle$ or $|6\rangle$ states. This was expected since in the $\mathbf{k}\cdot\mathbf{p}$ Hamiltonian Eq. 2.35 (see also Appendix A), the only non-zero entries in the second and sixth rows are the diagonal entries. Therefore, states $|2\rangle$ and $|6\rangle$ can be thought of as not interacting with other states at the zone center. Similar to the conduction band states, these valence band states were also highly extended compared to the QW thicknesses.

4.9. Discussions

A plausible growth mechanism is proposed to explain the insertion of the ultra-thin QWs based on a kinetic argument. It is well known that Ga is preferentially incorporated during the InGa N growth and indium incorporation is only possible when the Ga/N flux ratio is sufficiently small.¹²¹ For this reason, the Ga-rich growth condition during the GaN spacer growth was used to

completely prevent the In incorporation as well as to realize a high crystal quality. Therefore, it seems controversial that indium could still be incorporated into the 1 or 2-ML thick QWs during the initial GaN spacer growth as seen in Figure 4-11.

It is proposed that here the assumption of Ga-rich growth condition is momentarily invalid at the beginning of GaN capping stage. To capture the most essential features of the QW formation process, a simple growth scenario was considered first in Figure 4-17.

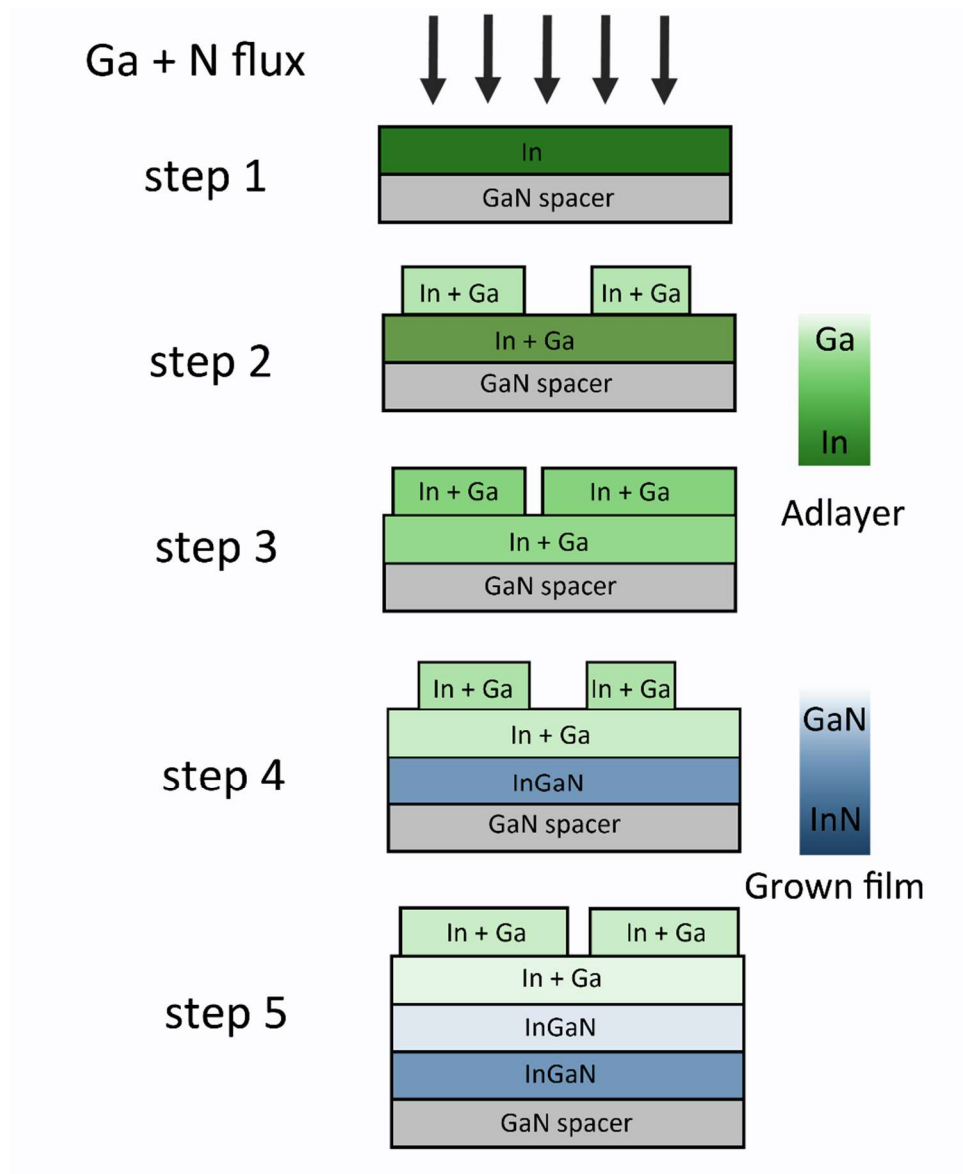


Figure 4-17. Schematic of the formation of the first two monolayers of InGaN film.

In Figure 4-17, it is assumed that a GaN surface is covered by exactly 1 ML of indium and the active nitrogen is impinging the surface prior to the GaN spacer growth. It is worth noting that InN film growth is prohibited at 550 °C due to low In-N binding energy and, thus, the 1 ML indium coverage remains in a liquid-like form. On the other hand, given the fact that at 550 °C the growth of bulk InGaN is possible, the film growth must be triggered by the introduction of Ga into the 1 ML indium. Once the Ga shutter is open (step 1), newly arrived Ga adatoms start to build the second metal adlayer. At the same time, similar to what is observed in MME InGaN growth,¹⁹² a diffusion process occurs so that the Ga atoms start to replace the indium atoms in the bottom adlayer (step 2) and, in the meantime, the (InGaN) film growth is triggered. The effective Ga flux reaching the growth front (the bottom metal adlayer) is limited by this diffusion process and is very small in the beginning of GaN capping. As a result, the growth at the beginning of the GaN capping can be effectively regarded as N-rich and the incorporation of indium atoms becomes possible.

As the growth continues, the diffusion process keeps reducing the indium concentration in the bottom adlayer (step 3) until it is fully solidified into an InGaN film (step 4). It should be pointed out that indium atoms in the InGaN film are still allowed to be replaced by the Ga atoms from the top liquid-like adlayers and, thus, the indium content in the InGaN film is further reduced. This second exchange mechanism is driven by the large difference between the In-N and Ga-N binding energy and is similar to what is observed in the study of AlN/GaN MQWs growth.¹⁹⁴ The knowledge of the exact indium concentration in this InGaN film requires detailed information about the kinetic processes of diffusion, film growth, and the second exchange mechanism. However, it is reasonable to expect that this film is Ga-rich since the In-N bonding is extremely unstable at the growth temperature of 550 °C.

Step 4 can be viewed as the initial growth condition for the second InGaN layer and the

growth process is similar to that of the first InGaN layer. Compared to the growth of the first InGaN layer, the surface before growth is covered by Ga-containing adlayers instead of a pure indium adlayer (see step 1) and, thus, it can be expected that the final indium content in the second InGaN layer is much smaller than that of the first InGaN layer (step 5). Moreover, as the GaN capping proceeds, the adlayer on the surface becomes more and more Ga-rich and eventually the indium incorporation becomes impossible.

This growth model may be supported by ref. 145, the only study that had been focusing on the effect of Ga/N ratio during GaN capping. It was found that abrupt QWs with apparent thickness less than 2 MLs were only formed when the Ga/N flux ratio was larger than unity. The N-rich growth of the GaN spacer leads to a widening of the QW thickness and smearing of the interfaces.

Variations to the growth model depicted in Figure 4-17 can be used to explain other growth scenarios. First of all, if in step 1 the surface is covered by two MLs of indium before growth, it can be expected that both the first and second InGaN layers are more indium-rich than the case depicted in Figure 4-17, since the Ga atoms have to diffuse through a thicker indium adlayer. This may explain the redshift of PL emission in Figure 4-9(a) when the nominal InN QW thickness became larger. Moreover, if the surface indium coverage is further increased, excess indium other than the 2-ML adlayers will grow into droplets and a large portion of surface still remains to be covered by 2-ML indium adlayers. This practically gives the same initial growth condition as the case with exactly 2-ML indium coverage and may explain why there is a saturation of PL energy when the nominal InN thickness is equal or larger than 2 MLs. Finally, as indicated by the “ $1+1/7$ ” RHEED pattern, the nominal InN QW growth could base on a InGaN surface instead of a GaN surface. This pre-existing InGaN layer should by intuition affect the QW structural property. However, the consistency of PL data suggests that the influence of this pre-existing InGaN was

very little. This may be explained by the instability of the surface InGa_N layer at 550 °C. As previously discussed, the non-capped InGa_N layer is subject to decomposition through losing nitrogen atoms and tends to segregate to pure GaN and indium adlayers. After the fairly long second growth interruption, it can be expected that prior to the GaN capping the InGa_N layer is segregated into indium-rich and indium-lean regions. The former is physically closer to a pure indium adlayer while the latter is closer to a GaN layer. Therefore, the overall effect of the pre-existing InGa_N layer is similar to a partial indium adlayer and thus brings little effect to the QW properties.

The kinetic argument discussed in Figure 4-17 qualitatively describes how the InGa_N quantum wells can be preserved. However, it should be expected that the final quantum well structure, i.e., thickness, indium content, and atomic ordering, should show a large dependence on the experimental conditions such as the nitrogen flux, metal flux, and substrate temperatures. On the other hand, the PL data in this work, as well as in other reported works, is relatively consistent. Especially, as is shown in Figure 4-9(b), QWs with nominal thickness ≥ 2 MLs gave a very small variation in emission peak positions.

This contradiction suggests that there should be an additional mechanism that regulates the structural properties of the QWs. One candidate mechanism is that a surface reconstruction with a $(\sqrt{3} \times \sqrt{3})R30^\circ$ or $(2\sqrt{3} \times 2\sqrt{3})R30^\circ$ symmetry was preserved. The corresponding indium content of 0.33 and 0.25 automatically explains the low indium content < 0.33 in TEM investigations.^{149,150,188} This argument is inferred by the “1×3” RHEED pattern that appeared during the InN deposition, as well as the “3×” ordering of indium atoms observed in the 1-ML thick QW samples by TEM.¹⁸⁸ However, the “1×3” RHEED pattern was generally not observed during the nominal InN QW growth in this study, especially for samples whose nominal InN QW

thickness is larger than 0.5 ML. Instead a “1+1/7” appeared before and during the InN QW deposition stage which was due to an indium incommensurate layer sitting on an InGa_N layer. What is more, the 2-ML thick QWs showed an even better PL emission consistency. If this also resulted from the ordering of indium atoms, how the $(\sqrt{3} \times \sqrt{3})R30^\circ$ or $(2\sqrt{3} \times 2\sqrt{3})R30^\circ$ surface reconstruction is frozen into the top monolayer of QWs during the continuous growth is not immediately clear. Furthermore, although the surface reconstruction showed a good stability as was discussed in the high temperature growth, more theoretical and experimental evidence is needed to show how this stability is maintained during GaN capping. As shown in Figure 3-13, the recently proposed $(2\sqrt{3} \times 2\sqrt{3})R30^\circ$ surface structure has a 2×2 nitrogen overlayer. The nitrogen atoms in the overlayer are located at the H3 sites instead of the T4 sites and thus are not consistent with the bulk wurtzite crystal structure. As a result, the GaN capping of the surface reconstruction would break the nitrogen bonding to the underlying metal layer and the stability of the surface structure could be broken.

The simulation of bulk InGa_N growth employing a combined method of Monte Carlo and ab initio calculations¹⁹⁵ suggested an alternative explanation of the chemical ordering of indium atoms. It is found that there is a strong tendency for low-In-content InGa_N bulk to be phase separated into pure GaN and In_{0.33}Ga_{0.67}N with an in-plane $(\sqrt{3} \times \sqrt{3})R30^\circ$ ordering of indium atoms. In this scenario, the chemical ordering of indium does not need a pre-existing surface reconstruction as a template.

Using this argument, a plausible growth process is described as follows: in the beginning of GaN capping, due to the temporary N-rich growth a substantial amount of indium can be frozen mainly into the first 1 or 2 MLs of bulk film, depending on the indium coverage from the nominal InN deposition and previous InN/GaN growth cycles. The indium incorporation after the second

ML should be negligibly small, mainly due to the thickness of indium adlayers being limited to ~ 2 MLs. Simultaneous to the indium incorporation, the indium atoms are self-assembled into grains with an in-plane $(\sqrt{3} \times \sqrt{3})R30^\circ$ symmetry. Since these grains have an equivalent In content of ~ 0.33 , the PL emission peaks are consistently located at ~ 390 nm and ~ 423 nm, corresponding to the QW thickness of 1 ML and 2 MLs.

4.10. Summary

To summarize, the growth of InN/GaN MQWs were investigated at a low growth temperature of 550°C . The growth process was characterized by the evolution of the RHEED intensity and patterns. It was found that there was a residual indium accumulation after each InN/GaN growth cycle which led to the formation of a “ $1+1/7$ ” RHEED pattern instead of a widely observed $(\sqrt{3} \times \sqrt{3})R30^\circ$ one, before and during the InN QW deposition stage. The insertion of a QW with sharp interfaces was confirmed by XRD and TEM investigations and the QW thickness was found to be no more than 2 MLs. The PL data also showed a similar self-regulating behavior that the redshift of PL emission with larger nominal InN deposition was situated at ~ 423 nm. The two distinct groups of emission peaks at ~ 390 nm and ~ 423 nm were due to the QWs with apparent thickness of 1 ML and 2 MLs respectively. Finally, a plausible growth model was discussed. The insertion of QWs was attributed to the momentary N-rich growth condition at the beginning of GaN capping stage.

Chapter 5: Conclusions and future work

5.1. Conclusions

This dissertation focused on the MBE growth of InN/GaN MQWs at two temperatures near the ends of allowed growth temperature window.

At the high growth temperature of 680 °C, the indium adsorption and desorption behavior and their relationship to the indium surface coverage were investigated by RHEED first to gain knowledge of growth process control. To gain further physical insights, the results on $(\sqrt{3} \times \sqrt{3})R30^\circ$ surfaces, which correspond to the real growth, were compared with the results obtained on GaN 1×1 surfaces. A dynamically stable In coverage up to 2 MLs before droplets formation was found on $(\sqrt{3} \times \sqrt{3})R30^\circ$ surfaces, which is similar to that on the GaN 1×1 surfaces. However, a new observation about the $(\sqrt{3} \times \sqrt{3})R30^\circ$ surfaces is that there does not exist a wide flux window in which exactly one monolayer of indium can be stabilized. Further, the desorption rate showed a different dependence on indium coverage. Although the desorption of the bottom indium adlayer is dramatically faster on a $(\sqrt{3} \times \sqrt{3})R30^\circ$ surface, once the bottom adlayer is completely covered by the top adlayer, the desorption rates become identical on both surfaces. These observations lead to the conclusion that only the bottom adlayer is influenced by the presence of the surface reconstructions, which is attributed to the weaker interaction between the $(\sqrt{3} \times \sqrt{3})R30^\circ$ surface and the applied indium layer.

With the knowledge of the indium coverage kinetics, MQW growth with various InN deposition strategies were designed and tested, and the growth processes was monitored by RHEED. A good correspondence between the growth phenomena and RHEED features was established, which shows that RHEED is an eligible in situ monitoring tool for the MQW growth during which many complex growth phenomena are present. The main result is that keeping the

integrity of the 2-ML indium adlayers, which requires a high In flux in the droplet accumulation regime, is the key to the quantum well formation with consistent structural properties. The insertion of the QWs was confirmed by XRD and PL measurements. The PL emission peaks at ~375 nm indicated the nominal QW thicknesses were 1 ML.

At the low growth temperature of 550 °C, the RHEED intensity analysis revealed that even for a very small nominal InN thickness of 0.5 ML, a certain portion of the In deposition was not incorporated in the QWs and the residual indium increased its size after each QW growth. Moreover, a “1+1/7” RHEED pattern appeared at the end of each InN/GaN bilayer growth, which is a new observation for MBE systems in the temperature range around 550 °C. Based on the relationship between its appearance and growth procedures, as well as RHEED pattern simulations, it can be concluded that this newly observed pattern is due to an incommensurate indium overlayer on an InGaN film formed at the end of each InN/GaN growth cycle.

MQWs with abrupt interfaces were directly observed by cross-sectional TEM measurements. For all MQWs, the apparent thickness was 1 or 2 MLs showing a self-regulating behavior. The PL emissions also showed a self-regulating behavior. The redshift of PL emission with increased nominal InN QW thickness saturated at a wavelength of ~423 nm, corresponding to a 2-ML apparent thickness. In addition, PL emission around 380 nm is attributed to MQWs with 1-ML apparent thickness. These observations suggest that the apparent InN quantum wells actually consist of an InGaN layer. The eight-band **k.p** calculations showed a good agreement with PL data when the In content was 43%. A growth model based on a kinetic argument was proposed to explain the formation of QWs. The preservation of indium atoms in the quantum well is attributed to a momentary N-rich growth condition at the beginning of the GaN capping process. The good consistency in PL data was tentatively attributed to phase separation behavior.

5.2. Future work

The InN/GaN MQW growth should be further investigated in the intermediate temperature range ($\sim 600^\circ\text{C}$ to 650°C) and the low temperature range ($\sim 450^\circ\text{C}$ to 500°C). The intermediate temperature range is interesting because of the balance of overall material quality, i.e., good material quality is expected not only for the 1- or 2-ML thick QWs but also for the barrier materials such as GaN and AlGaIn. The low temperature range is interesting for the possibility of more indium incorporation. Both the In content and the QW thickness should be increased since in this temperature range the bulk InN decomposition is not pronounced.

The influence of the Ga/N flux ratio should be investigated at fixed temperatures to test the proposed growth mechanism for QW preservation based on a kinetic argument. One ideal method for this investigation is to conduct cross-sectional TEM and CL measurements on a sample with a series of QWs grown under various Ga/N flux ratios. In particular, the in-plane atomic ordering for 2-ML thick QWs should be analyzed, which is important to understand the consistency of the saturated PL emissions.

The energy structure of the MQWs with the $(\sqrt{3}\times\sqrt{3})R30^\circ$ and the $(2\sqrt{3}\times 2\sqrt{3})R30^\circ$ chemical ordering should be investigated based on first principle calculations to gain further insight for the origins of PL data as well as for the growth mechanisms. In this work the energy structure of InGaIn/GaN quantum wells were only investigated using the semi-empirical **k.p** method and the chemical ordering effect could not be implemented.

References

1. J. Wu, W. Walukiewicz, W. Shan, K. M. Yu, J. W. Ager, S. X. Li, E. E. Haller, H. Lu, and W. J. Schaff, “*Temperature Dependence of the Fundamental Band Gap of InN.*” J. Appl. Phys., 94, 4457–4460, (2003).
2. S. Nakamura, and T. Mukai, “*High-Quality InGaN Films Grown on GaN Films.*” Jpn. J. Appl. Phys., 31, L1457–L1459, (1992).
3. H. Amano, M. Kito, K. Hiramatsu, and I. Akasaki, “*P-Type Conduction in Mg-Doped GaN Treated with Low-Energy Electron Beam Irradiation (LEEBI).*” Jpn. J. Appl. Phys., 28, L2112–L2114, (1989).
4. S. Nakamura, T. Mukai, M. Senoh, and N. Iwasa, “*Thermal Annealing Effects on P-Type Mg-Doped GaN Films.*” Jpn. J. Appl. Phys., 31, L139–L142, (1992).
5. S. Nakamura, N. Iwasa, M. Senoh, and T. Mukai, “*Hole Compensation Mechanism of P-Type GaN Films.*” Jpn. J. Appl. Phys., 31, 1258–1266, (1992).
6. S. Nakamura, M. Senoh, and T. Mukai, “*P-GaN/N-InGaN/N-GaN Double-Heterostructure Blue-Light-Emitting Diodes.*” Jpn. J. Appl. Phys., 32, L8–L11, (1993).
7. S. Nakamura, M. Senoh, S. Nagahama, N. Iwasa, T. Yamada, T. Matsushita, H. Kiyoku, and Y. Sugimoto, “*InGaN-Based Multi-Quantum-Well-Structure Laser Diodes.*” Jpn. J. Appl. Phys., 35, L74–L76, (1996).
8. U. K. Mishra, Shen Likun, T. E. Kazior, and Yi-Feng Wu, “*GaN-Based RF Power Devices and Amplifiers.*” Proc. IEEE, 96, 287–305, (2008).
9. M. Asif Khan, A. Bhattarai, J. N. Kuznia, and D. T. Olson, “*High Electron Mobility Transistor Based on a GaN-Al x Ga 1–x N Heterojunction.*” Appl. Phys. Lett., 63, 1214–1215, (1993).
10. D. Maier, M. Alomari, N. Grandjean, J.-F. Carlin, M.-A. Dufort-Poisson, C. Dua, S. Delage, and E. Kohn, “*InAlN/GaN HEMTs for Operation in the 1000 °C Regime: A First Experiment.*” IEEE Electron Device Lett., 33, 985–987, (2012).
11. S. J. Pearton, F. Ren, A. P. Zhang, and K. P. Lee, “*Fabrication and Performance of GaN Electronic Devices.*” Mater. Sci. Eng. R Reports, 30, 55–212, (2000).
12. S. W. Kaun, M. H. Wong, U. K. Mishra, and J. S. Speck, “*Molecular Beam Epitaxy for High-Performance Ga-Face GaN Electron Devices.*” Semicond. Sci. Technol., 28, 074001, (2013).
13. J. Wang, P. Mulligan, L. Brillson, and L. R. Cao, “*Review of Using Gallium Nitride for Ionizing Radiation Detection.*” Appl. Phys. Rev., 2, 031102, (2015).

14. P. J. Sellin, and J. Vaitkus, “*New Materials for Radiation Hard Semiconductor Detectors.*” Nucl. Instruments Methods Phys. Res. Sect. A Accel. Spectrometers, Detect. Assoc. Equip., 557, 479–489, (2006).
15. E. A. Burgemeister, W. von Muench, and E. Pettenpaul, “*Thermal Conductivity and Electrical Properties of 6 H Silicon Carbide.*” J. Appl. Phys., 50, 5790–5794, (1979).
16. E. L. Kern, D. W. Hamill, H. W. Deem, and H. D. Sheets, “*Thermal properties of β -silicon carbide from 20 to 2000 °C.*” In *Silicon Carbide–1968*; Elsevier, 1969; pp S25–S32.
17. T. P. Chow, “*High-Voltage SiC and GaN Power Devices.*” Microelectron. Eng., 83, 112–122, (2006).
18. J. Wu, “*When Group-III Nitrides Go Infrared: New Properties and Perspectives.*” J. Appl. Phys., 106, 011101, (2009).
19. H. Köck, C. A. Chapin, C. Ostermaier, O. Häberlen, and D. G. Senesky, “*Emerging GaN-Based HEMTs for Mechanical Sensing within Harsh Environments;*” Senesky, D. G., Dekate, S., Eds.; 2014; Vol. 9113, p 91130D.
20. S. Vittoz, L. Rufer, G. Rehder, R. Srnanek, and J. Kovac, “*Study of Built-in Stress Distribution in AlGaIn/GaN/AlN Heterostructure Based Cantilevers for Mechanical Sensing in Harsh Environments.*” In *2011 4th IEEE International Workshop on Advances in Sensors and Interfaces (IWASI)*; IEEE, 2011; pp 17–20.
21. J. Vaitkus, W. Cunningham, E. Gaubas, M. Rahman, S. Sakai, K. M. Smith, and T. Wang, “*Semi-Insulating GaN and Its Evaluation for α Particle Detection.*” Nucl. Instruments Methods Phys. Res. Sect. A Accel. Spectrometers, Detect. Assoc. Equip., 509, 60–64, (2003).
22. T. P. White, S. Shetty, M. E. Ware, H. A. Mantooth, and G. J. Salamo, “*AlGaIn/GaN Micro-Hall Effect Devices for Simultaneous Current and Temperature Measurements From Line Currents.*” IEEE Sens. J., 18, 2944–2951, (2018).
23. F. Bernardini, V. Fiorentini, and D. Vanderbilt, “*Spontaneous Polarization and Piezoelectric Constants of III-V Nitrides.*” Phys. Rev. B, 56, R10024–R10027, (1997).
24. E. T. Yu, X. Z. Dang, P. M. Asbeck, S. S. Lau, and G. J. Sullivan, “*Spontaneous and Piezoelectric Polarization Effects in III–V Nitride Heterostructures.*” J. Vac. Sci. Technol. B Microelectron. Nanom. Struct., 17, 1742, (1999).
25. O. Ambacher, R. Dimitrov, M. Stutzmann, B. E. Foutz, M. J. Murphy, J. A. Smart, J. R. Shealy, N. G. Weimann, K. Chu, M. Chumbes, B. Green, A. J. Sierakowski, W. J. Schaff, and L. F. Eastman, “*Role of Spontaneous and Piezoelectric Polarization Induced Effects in Group-III Nitride Based Heterostructures and Devices.*” Phys. status solidi, 216, 381–389, (1999).

26. O. Ambacher, J. Smart, J. R. Shealy, N. G. Weimann, K. Chu, M. Murphy, W. J. Schaff, L. F. Eastman, R. Dimitrov, L. Wittmer, M. Stutzmann, W. Rieger and J. Hilsenbeck, “*Two-Dimensional Electron Gases Induced by Spontaneous and Piezoelectric Polarization Charges in N- and Ga-Face AlGa_N/Ga_N Heterostructures.*” J. Appl. Phys., 85, 3222–3233, (1999).
27. J. Wu, W. Walukiewicz, K. M. Yu, J. W. Ager III, E. E. Haller, H. Lu, and W. J. Schaff, “*Narrow Bandgap Group III-Nitride Alloys.*” Phys. status solidi, 240, 412–416, (2003).
28. F. Yun, M. A. Reshchikov, L. He, T. King, H. Morkoç, S. W. Novak, and L. Wei, “*Energy Band Bowing Parameter in Al_xGa_{1-x}N Alloys.*” J. Appl. Phys., 92, 4837–4839, (2002).
29. I. Vurgaftman, and J. R. Meyer, “*Electron Bandstructure Parameters.*” In *Nitride Semiconductor Devices: Principles and Simulation*; Wiley-VCH Verlag GmbH & Co. KGaA: Weinheim, Germany; pp 13–48.
30. F. Bernardini, “*Spontaneous and Piezoelectric Polarization: Basic Theory vs. Practical Recipes.*” In *Nitride Semiconductor Devices: Principles and Simulation*; Wiley-VCH Verlag GmbH & Co. KGaA: Weinheim, Germany; pp 49–68.
31. A. Zoroddu, F. Bernardini, P. Ruggerone, and V. Fiorentini, “*First-Principles Prediction of Structure, Energetics, Formation Enthalpy, Elastic Constants, Polarization, and Piezoelectric Constants of AlN, GaN, and InN: Comparison of Local and Gradient-Corrected Density-Functional Theory.*” Phys. Rev. B, 64, 045208, (2001).
32. J. P. Ibbetson, P. T. Fini, K. D. Ness, S. P. DenBaars, J. S. Speck, and U. K. Mishra, “*Polarization Effects, Surface States, and the Source of Electrons in AlGa_N/Ga_N Heterostructure Field Effect Transistors.*” Appl. Phys. Lett., 77, 250–252, (2000).
33. D. Sizov, R. Bhat, and C. E. Zah, “*Gallium Indium Nitride-Based Green Lasers.*” J. Light. Technol., 30, 679–699, (2012).
34. S. Li, M. Ware, J. Wu, P. Minor, Z. Wang, Z. Wu, Y. Jiang, and G. J. Salamo, “*Polarization Induced P_n-Junction without Dopant in Graded AlGa_N Coherently Strained on Ga_N.*” Appl. Phys. Lett., 101, 122103, (2012).
35. S. Li, M. E. Ware, V. P. Kunets, M. Hawkridge, P. Minor, J. Wu, and G. J. Salamo, “*Polarization Induced Doping in Graded AlGa_N Films.*” Phys. status solidi, 8, 2182–2184, (2011).
36. S. Li, M. E. Ware, J. Wu, V. P. Kunets, M. Hawkridge, P. Minor, Z. Wang, Z. Wu, Y. Jiang, and G. J. Salamo, “*Polarization Doping: Reservoir Effects of the Substrate in AlGa_N Graded Layers.*” J. Appl. Phys., 112, 053711, (2012).
37. D. Jena, S. Heikman, J. S. Speck, A. Gossard, U. K. Mishra, A. Link, and O. Ambacher, “*Magnetotransport Properties of a Polarization-Doped Three-Dimensional Electron Slab*

- in Graded AlGa_N.*” Phys. Rev. B, 67, 153306, (2003).
38. D. Jena, S. Heikman, D. Green, D. Buttari, R. Coffie, H. Xing, S. Keller, S. DenBaars, J. S. Speck, U. K. Mishra, and I. Smorchkova, “*Realization of Wide Electron Slabs by Polarization Bulk Doping in Graded III–V Nitride Semiconductor Alloys.*” Appl. Phys. Lett., 81, 4395–4397, (2002).
 39. L. Zhang, K. Ding, J. C. Yan, J. X. Wang, Y. P. Zeng, T. B. Wei, Y. Y. Li, B. J. Sun, R. F. Duan, and J. M. Li, “*Three-Dimensional Hole Gas Induced by Polarization in (0001)-Oriented Metal-Face III-Nitride Structure.*” Appl. Phys. Lett., 97, 062103, (2010).
 40. Y. Enatsu, C. Gupta, S. Keller, S. Nakamura, and U. K. Mishra, “*P–n Junction Diodes with Polarization Induced P-Type Graded In_xGa_{1–x}N Layer.*” Semicond. Sci. Technol., 32, 105013, (2017).
 41. S. D. Carnevale, T. F. Kent, P. J. Phillips, M. J. Mills, S. Rajan, and R. C. Myers, “*Polarization-Induced Pn Diodes in Wide-Band-Gap Nanowires with Ultraviolet Electroluminescence.*” Nano Lett., 12, 915–920, (2012).
 42. Y. Enatsu, C. Gupta, M. Laurent, S. Keller, S. Nakamura, and U. K. Mishra, “*Polarization Induced Three-Dimensional Hole Gas in Compositionally Graded In_xGa_{1–x}N Layer.*” Appl. Phys. Express, 9, 075502, (2016).
 43. J. Simon, V. Protasenko, C. Lian, H. Xing, and D. Jena, “*Polarization-Induced Hole Doping in Wide-Band-Gap Uniaxial Semiconductor Heterostructures.*” Science, 327, 60–64, (2010).
 44. B. Jogai, “*Influence of Surface States on the Two-Dimensional Electron Gas in AlGa_N/Ga_N Heterojunction Field-Effect Transistors.*” J. Appl. Phys., 93, 1631–1635, (2003).
 45. H. Okumura, B. M. McSkimming, T. Huault, C. Chaix, and J. S. Speck, “*Growth Diagram of N-Face Ga_N (0001 $\bar{1}$) Grown at High Rate by Plasma-Assisted Molecular Beam Epitaxy.*” Appl. Phys. Lett., 104, 012111, (2014).
 46. E. Monroy, E. Sarigiannidou, F. Fossard, N. Gogneau, E. Bellet-Amalric, J.-L. Rouvière, S. Monnoye, H. Mank, and B. Daudin, “*Growth Kinetics of N-Face Polarity Ga_N by Plasma-Assisted Molecular-Beam Epitaxy.*” Appl. Phys. Lett., 84, 3684–3686, (2004).
 47. G. Koblmüller, R. Averbeck, H. Riechert, and P. Pongratz, “*Direct Observation of Different Equilibrium Ga Adlayer Coverages and Their Desorption Kinetics on Ga_N (0001) and (000 $\bar{1}$) Surfaces.*” Phys. Rev. B, 69, 035325, (2004).
 48. B. L. VanMil, H. Guo, L. J. Holbert, K. Lee, C. H. Swartz, T. Liu, D. Korakakis, and T. H. Myers, “*High Temperature Limitations for Ga_N Growth by RF-Plasma Assisted Molecular Beam Epitaxy: Effects of Active Nitrogen Species, Surface Polarity, and Excess Ga-Overpressure.*” Phys. status solidi, 2, 2174–2177, (2005).

49. X. Wang, S.-B. Che, Y. Ishitani, and A. Yoshikawa, “*Effect of Epitaxial Temperature on N-Polar InN Films Grown by Molecular Beam Epitaxy.*” J. Appl. Phys., 99, 073512, (2006).
50. D. Zhuang, and J. H. Edgar, “*Wet Etching of GaN, AlN, and SiC: A Review.*” Mater. Sci. Eng. R Reports, 48, 1–46, (2005).
51. T. Palacios, F. Calle, M. Varela, C. Ballesteros, E. Monroy, F. B. Naranjo, M. A. Sánchez-García, E. Calleja, and E. Muñoz, “*Wet Etching of GaN Grown by Molecular Beam Epitaxy on Si(111).*” Semicond. Sci. Technol., 15, 996–1000, (2000).
52. A. Feduniewicz, C. Skierbiszewski, M. Siekacz, Z. R. Wasilewski, I. Sproule, S. Grzanka, R. Jakiela, J. Borysiuk, G. Kamler, E. Litwin-Staszewska, R. Czernecki, M. Boćkowski, and S. Porowski, “*Control of Mg Doping of GaN in RF-Plasma Molecular Beam Epitaxy.*” J. Cryst. Growth, 278, 443–448, (2005).
53. E. Sarigiannidou, E. Monroy, M. Hermann, T. Andreev, P. Holliger, S. Monnoye, H. Mank, B. Daudin, and M. Eickhoff, “*Phase Transition by Mg Doping of N-Face Polarity GaN.*” Phys. status solidi, 2, 2216–2219, (2005).
54. D. F. Storm, D. S. Katzer, D. J. Meyer, and S. C. Binari, “*Oxygen Incorporation in Homoepitaxial N-Polar GaN Grown by Radio Frequency-Plasma Assisted Molecular Beam Epitaxy: Mitigation and Modeling.*” J. Appl. Phys., 112, 013507, (2012).
55. M. Sumiya, K. Yoshimura, K. Ohtsuka, and S. Fuke, “*Dependence of Impurity Incorporation on the Polar Direction of GaN Film Growth.*” Appl. Phys. Lett., 76, 2098–2100, (2000).
56. A. J. Ptak, L. J. Holbert, L. Ting, C. H. Swartz, M. Moldovan, N. C. Giles, T. H. Myers, P. Van Lierde, C. Tian, R. A. Hockett, S. Mitha, A. E. Wickenden, D. D. Koleske, and R. L. Henry, “*Controlled Oxygen Doping of GaN Using Plasma Assisted Molecular-Beam Epitaxy.*” Appl. Phys. Lett., 79, 2740–2742, (2001).
57. T. K. Zywietz, J. Neugebauer, and M. Scheffler, “*The Adsorption of Oxygen at GaN Surfaces.*” Appl. Phys. Lett., 74, 1695–1697, (1999).
58. S. Keller, N. Fichtenbaum, F. Wu, G. Lee, S. P. DenBaars, J. S. Speck, and U. K. Mishra, “*Effect of the Nucleation Conditions on the Polarity of AlN and GaN Films Grown on C-Face 6H-SiC.*” Jpn. J. Appl. Phys., 45, L322–L325, (2006).
59. E. J. Tarsa, B. Heying, X. H. Wu, P. Fini, S. P. DenBaars, and J. S. Speck, “*Homoepitaxial Growth of GaN under Ga-Stable and N-Stable Conditions by Plasma-Assisted Molecular Beam Epitaxy.*” J. Appl. Phys., 82, 5472–5479, (1997).
60. M. H. Wong, Y. Pei, T. Palacios, L. Shen, A. Chakraborty, L. S. McCarthy, S. Keller, S. P. DenBaars, J. S. Speck, and U. K. Mishra, “*Low Nonalloyed Ohmic Contact Resistance to Nitride High Electron Mobility Transistors Using N-Face Growth.*” Appl. Phys. Lett., 91,

232103, (2007).

61. Man Hoi Wong, Yi Pei, Rongming Chu, S. Rajan, B. L. Swenson, D. F. Brown, S. Keller, S. P. DenBaars, J. S. Speck, and U. K. Mishra, “*N-Face Metal–Insulator–Semiconductor High-Electron-Mobility Transistors With AlN Back-Barrier.*” IEEE Electron Device Lett., 29, 1101–1104, (2008).
62. H. P. Maruska, and J. J. Tietjen, “*The Preparation and Properties of Vapor Deposited Single crystalline GaN.*” Appl. Phys. Lett., 15, 327–329, (1969).
63. M. Ilegems, and R. Dingle, “*Luminescence of Be- and Mg-doped GaN.*” J. Appl. Phys., 44, 4234–4235, (1973).
64. J. I. Pankove, M. T. Duffy, E. A. Miller, and J. E. Berkeyheiser, “*Luminescence of Insulating Be-Doped and Li-Doped GaN.*” J. Lumin., 8, 89–93, (1973).
65. O. Lagerstedt, and B. Monemar, “*Luminescence in Epitaxial GaN : Cd.*” J. Appl. Phys., 45, 2266–2272, (1974).
66. B. Monemar, O. Lagerstedt, and H. P. Gislason, “*Properties of Zn-doped VPE-grown GaN. I. Luminescence Data in Relation to Doping Conditions.*” J. Appl. Phys., 51, 625–639, (1980).
67. H. P. Maruska, W. C. Rhines, and D. A. Stevenson, “*Preparation of Mg-Doped GaN Diodes Exhibiting Violet Electroluminescence.*” Mater. Res. Bull., 7, 777–781, (1972).
68. J. I. Pankove, E. A. Miller, and J. E. Berkeyheiser, “*GaN Blue Light-Emitting Diodes.*” J. Lumin., 5, 84–86, (1972).
69. J. I. Pankove, E. A. Miller, and J. E. Berkeyheiser, “*GaN Electroluminescent Diodes.*” R.C.A. Rev., 32, 383, (1971).
70. H. P. Maruska, D. A. Stevenson, and J. I. Pankove, “*Violet Luminescence of Mg-doped GaN.*” Appl. Phys. Lett., 22, 303–305, (1973).
71. H. P. Maruska, and D. A. Stevenson, “*Mechanism of Light Production in Metal-Insulator-Semiconductor Diodes; GaN:Mg Violet Light-Emitting Diodes.*” Solid. State. Electron., 17, 1171–1179, (1974).
72. S. Nakamura, “*Nobel Lecture: Background Story of the Invention of Efficient Blue InGaN Light Emitting Diodes.*” Rev. Mod. Phys., 87, 1139–1151, (2015).
73. S. Yoshida, S. Misawa, and S. Gonda, “*Improvements on the Electrical and Luminescent Properties of Reactive Molecular Beam Epitaxially Grown GaN Films by Using AlN-coated Sapphire Substrates.*” Appl. Phys. Lett., 42, 427–429, (1983).

74. H. Amano, N. Sawaki, I. Akasaki, and Y. Toyoda, “*Metalorganic Vapor Phase Epitaxial Growth of a High Quality GaN Film Using an AlN Buffer Layer.*” Appl. Phys. Lett., 48, 353–355, (1986).
75. S. Nakamura, Y. Harada, and M. Seno, “*Novel Metalorganic Chemical Vapor Deposition System for GaN Growth.*” Appl. Phys. Lett., 58, 2021–2023, (1991).
76. S. Nakamura, “*GaN Growth Using GaN Buffer Layer.*” Jpn. J. Appl. Phys., 30, L1705–L1707, (1991).
77. S. Nakamura, T. Mukai, and M. Senoh, “*Candela-class High-brightness InGaN/AlGaN Double-heterostructure Blue-light-emitting Diodes.*” Appl. Phys. Lett., 64, 1687–1689, (1994).
78. S. Nakamura, M. Senoh, S. Nagahama, N. Iwasa, T. Yamada, T. Matsushita, H. Kiyoku, Y. Sugimoto, T. Kozaki, H. Umemoto, and M. Sano, “*InGaN/GaN/AlGaN-Based Laser Diodes with Modulation-Doped Strained-Layer Superlattices Grown on an Epitaxially Laterally Overgrown GaN Substrate.*” Appl. Phys. Lett., 72, 211–213, (1998).
79. H. Gotoh, T. Suga, H. Suzuki, and M. Kimata, “*Low Temperature Growth of Gallium Nitride.*” Jpn. J. Appl. Phys., 20, L545–L548, (1981).
80. R. Singh, R. J. Molnar, M. S. Ünlü, and T. D. Moustakas, “*Intensity Dependence of Photoluminescence in GaN Thin Films.*” Appl. Phys. Lett., 64, 336–338, (1994).
81. R. J. Molnar, and T. D. Moustakas, “*Growth of Gallium Nitride by Electron-cyclotron Resonance Plasma-assisted Molecular-beam Epitaxy: The Role of Charged Species.*” J. Appl. Phys., 76, 4587–4595, (1994).
82. A. Ishizaka, and Y. Murata, “*Crystal Growth Model for Molecular Beam Epitaxy: Role of Kinks on Crystal Growth.*” J. Phys. Condens. Matter, 6, L693–L698, (1994).
83. W. K. Burton, N. Cabrera, and F. C. Frank, “*The Growth of Crystals and the Equilibrium Structure of Their Surfaces.*” Philos. Trans. R. Soc. A Math. Phys. Eng. Sci., 243, 299–358, (1951).
84. C. Skierbiszewski, H. Turski, G. Muziol, M. Siekacz, M. Sawicka, G. Cywiński, Z. R. Wasilewski, and S. Porowski, “*Nitride-Based Laser Diodes Grown by Plasma-Assisted Molecular Beam Epitaxy.*” J. Phys. D. Appl. Phys., 47, 073001, (2014).
85. J. Neugebauer, T. K. Zywietz, M. Scheffler, J. E. Northrup, H. Chen, and R. M. Feenstra, “*Adatom Kinetics On and Below the Surface: The Existence of a New Diffusion Channel.*” Phys. Rev. Lett., 90, 056101, (2003).
86. C. Skierbiszewski, P. Wiśniewski, M. Siekacz, P. Perlin, A. Feduniewicz-Zmuda, G. Nowak, I. Grzegory, M. Leszczyński, and S. Porowski, “*60mW Continuous-Wave*

- Operation of InGaN Laser Diodes Made by Plasma-Assisted Molecular-Beam Epitaxy.*" Appl. Phys. Lett., 88, 221108, (2006).
87. M. E. Lin, B. Sverdlov, G. L. Zhou, and H. Morkoç, "A Comparative Study of GaN Epilayers Grown on Sapphire and SiC Substrates by Plasma-assisted Molecular-beam Epitaxy." Appl. Phys. Lett., 62, 3479–3481, (1993).
 88. T. D. Moustakas, and R. J. Molnar, "Growth and Doping of GaN Films by ECR-Assisted MBE." MRS Proc., 281, 753, (1992).
 89. B. Heying, R. Averbeck, L. F. Chen, E. Haus, H. Riechert, and J. S. Speck, "Control of GaN Surface Morphologies Using Plasma-Assisted Molecular Beam Epitaxy." J. Appl. Phys., 88, 1855–1860, (2000).
 90. B. Heying, I. Smorchkova, C. Poblenz, C. Elsass, P. Fini, S. Den Baars, U. Mishra, and J. S. Speck, "Optimization of the Surface Morphologies and Electron Mobilities in GaN Grown by Plasma-Assisted Molecular Beam Epitaxy." Appl. Phys. Lett., 77, 2885–2887, (2000).
 91. C. Adelmann, J. Brault, G. Mula, B. Daudin, L. Lymperakis, and J. Neugebauer, "Gallium Adsorption on (0001) GaN Surfaces." Phys. Rev. B, 67, 165419, (2003).
 92. G. Koblmüller, S. Fernández-Garrido, E. Calleja, and J. S. Speck, "In Situ Investigation of Growth Modes during Plasma-Assisted Molecular Beam Epitaxy of (0001) GaN." Appl. Phys. Lett., 91, 161904, (2007).
 93. G. Koblmüller, R. Averbeck, L. Geelhaar, H. Riechert, W. Höslér, and P. Pongratz, "Growth Diagram and Morphologies of AlN Thin Films Grown by Molecular Beam Epitaxy." J. Appl. Phys., 93, 9591–9596, (2003).
 94. C. S. Gallinat, G. Koblmüller, J. S. Brown, and J. S. Speck, "A Growth Diagram for Plasma-Assisted Molecular Beam Epitaxy of In-Face InN." J. Appl. Phys., 102, 064907, (2007).
 95. A. L. Corrión, F. Wu, and J. S. Speck, "Growth Regimes during Homoepitaxial Growth of GaN by Ammonia Molecular Beam Epitaxy." J. Appl. Phys., 112, 054903, (2012).
 96. M. J. Manfra, K. W. Baldwin, a. M. Sargent, K. W. West, R. J. Molnar, and J. Caissie, "Electron Mobility Exceeding $160000\text{cm}^2/\text{Vs}$ in AlGaIn/GaN Heterostructures Grown by Molecular-Beam Epitaxy." Appl. Phys. Lett., 85, 5394–5396, (2004).
 97. C. Skierbiszewski, Z. R. Wasilewski, M. Siekacz, A. Feduniewicz, P. Perlin, P. Wisniewski, J. Borysiuk, I. Grzegory, M. Leszczynski, T. Suski, and S. Porowski, "Blue-Violet InGaN Laser Diodes Grown on Bulk GaN Substrates by Plasma-Assisted Molecular-Beam Epitaxy." Appl. Phys. Lett., 86, 011114, (2005).
 98. T. L. Tansley, and C. P. Foley, "Optical Band Gap of Indium Nitride." J. Appl. Phys., 59,

- 3241–3244, (1986).
99. W. Z. Shen, L. F. Jiang, H. F. Yang, F. Y. Meng, H. Ogawa, and Q. X. Guo, “*Bandtail Characteristics in InN Thin Films.*” Appl. Phys. Lett., 80, 2063–2065, (2002).
 100. Q. Guo, and A. Yoshida, “*Temperature Dependence of Band Gap Change in InN and AlN.*” Jpn. J. Appl. Phys., 33, 2453–2456, (1994).
 101. C. S. Gallinat, G. Koblmüller, J. S. Brown, S. Bernardis, J. S. Speck, G. D. Chern, E. D. Readinger, H. Shen, and M. Wraback, “*In-Polar InN Grown by Plasma-Assisted Molecular Beam Epitaxy.*” Appl. Phys. Lett., 89, 032109, (2006).
 102. J. Wu, W. Walukiewicz, K. M. Yu, J. W. Ager, E. E. Haller, H. Lu, W. J. Schaff, Y. Saito, and Y. Nanishi, “*Unusual Properties of the Fundamental Band Gap of InN.*” Appl. Phys. Lett., 80, 3967–3969, (2002).
 103. H. Lu, W. J. Schaff, J. Hwang, H. Wu, G. Koley, and L. F. Eastman, “*Effect of an AlN Buffer Layer on the Epitaxial Growth of InN by Molecular-Beam Epitaxy.*” Appl. Phys. Lett., 79, 1489–1491, (2001).
 104. Y. Nanishi, Y. Saito, and T. Yamaguchi, “*RF-Molecular Beam Epitaxy Growth and Properties of InN and Related Alloys.*” Jpn. J. Appl. Phys., 42, 2549–2559, (2003).
 105. E. Dimakis, E. Iliopoulos, K. Tsagaraki, T. Kehagias, P. Komninou, and A. Georgakilas, “*Heteroepitaxial Growth of In-Face InN on GaN (0001) by Plasma-Assisted Molecular-Beam Epitaxy.*” J. Appl. Phys., 97, 113520, (2005).
 106. A. Yamamoto, T. Tanaka, K. Koide, and A. Hashimoto, “*Improved Electrical Properties for Metalorganic Vapour Phase Epitaxial InN Films.*” Phys. status solidi, 194, 510–514, (2002).
 107. R. S. Q. Fareed, R. Jain, R. Gaska, M. S. Shur, J. Wu, W. Walukiewicz, and M. A. Khan, “*High Quality InN/GaN Heterostructures Grown by Migration Enhanced Metalorganic Chemical Vapor Deposition.*” Appl. Phys. Lett., 84, 1892–1894, (2004).
 108. A. G. Bhuiyan, K. Sugita, A. Hashimoto, and A. Yamamoto, “*InGaN Solar Cells: Present State of the Art and Important Challenges.*” IEEE J. Photovoltaics, 2, 276–293, (2012).
 109. A. G. Bhuiyan, A. Hashimoto, and A. Yamamoto, “*Indium Nitride (InN): A Review on Growth, Characterization, and Properties.*” J. Appl. Phys., 94, 2779–2808, (2003).
 110. S. J. Rosner, E. C. Carr, M. J. Ludowise, G. Girolami, and H. I. Erikson, “*Correlation of Cathodoluminescence Inhomogeneity with Microstructural Defects in Epitaxial GaN Grown by Metalorganic Chemical-Vapor Deposition.*” Appl. Phys. Lett., 70, 420–422, (1997).

111. T. Sugahara, H. Sato, M. Hao, Y. Naoi, S. Kurai, S. Tottori, K. Yamashita, K. Nishino, L. T. Romano, and S. Sakai, “*Direct Evidence That Dislocations Are Non-Radiative Recombination Centers in GaN.*” Jpn. J. Appl. Phys., 37, L398–L400, (1998).
112. S. J. Rosner, E. C. Carr, M. J. Ludowise, G. Girolami, and H. I. Erikson, “*Correlation of Cathodoluminescence Inhomogeneity with Microstructural Defects in Epitaxial GaN Grown by Metalorganic Chemical-Vapor Deposition.*” Appl. Phys. Lett., 70, 420–422, (1997).
113. T. Sugahara, H. Sato, M. Hao, Y. Naoi, S. Kurai, S. Tottori, K. Yamashita, K. Nishino, L. T. Romano, and S. Sakai, “*Direct Evidence That Dislocations Are Non-Radiative Recombination Centers in GaN.*” Jpn. J. Appl. Phys., 37, L398–L400, (1998).
114. J. M. Phillips, M. E. Coltrin, M. H. Crawford, A. J. Fischer, M. R. Krames, R. Mueller-Mach, G. O. Mueller, Y. Ohno, L. E. S. Rohwer, J. A. Simmons, and J. Y. Tsao, “*Research Challenges to Ultra-Efficient Inorganic Solid-State Lighting.*” Laser Photonics Rev., 1, 307–333, (2007).
115. S. Nakamura, “*Current Status and Future Prospects of InGaN-based Laser Diodes.*” JSAP Int., 1, 5–17, (2000).
116. S. Nakamura, “*The Roles of Structural Imperfections in InGaN-Based Blue Light-Emitting Diodes and Laser Diodes.*” Science, 281, 956–961, (1998).
117. J. J. Wierer, J. Y. Tsao, and D. S. Sizov, “*Comparison between Blue Lasers and Light-Emitting Diodes for Future Solid-State Lighting.*” Laser Photon. Rev., 7, 963–993, (2013).
118. O. H. Nam, K. H. Ha, J. S. Kwak, S. N. Lee, K. K. Choi, T. H. Chang, S. H. Chae, W. S. Lee, Y. J. Sung, H. S. Paek, J. H. Chae, T. Sakong, J. K. Son, H. Y. Ryu, Y. H. Kim, and Y. Park, “*Characteristics of GaN-Based Laser Diodes for Post-DVD Applications.*” phys. stat. sol., 201, 2717–2720, (2004).
119. X. Wang, S. Liu, N. Ma, L. Feng, G. Chen, F. Xu, N. Tang, S. Huang, K. J. Chen, S. Zhou, and B. Shen, “*High-Electron-Mobility InN Layers Grown by Boundary-Temperature-Controlled Epitaxy.*” Appl. Phys. Express, 5, 015502, (2012).
120. A. Wakahara, and A. Yoshida, “*Heteroepitaxial Growth of InN by Microwave-excited Metalorganic Vapor Phase Epitaxy.*” Appl. Phys. Lett., 54, 709–711, (1989).
121. C. Adelmann, R. Langer, G. Feuillet, and B. Daudin, “*Indium Incorporation during the Growth of InGaN by Molecular-Beam Epitaxy Studied by Reflection High-Energy Electron Diffraction Intensity Oscillations.*” Appl. Phys. Lett., 75, 3518–3520, (1999).
122. G. B. Stringfellow, “*Microstructures Produced during the Epitaxial Growth of InGaN Alloys.*” J. Cryst. Growth, 312, 735–749, (2010).

123. S. Figge, C. Tessarek, T. Aschenbrenner, and D. Hommel, “*InGaN Quantum Dot Growth in the Limits of Stranski-Krastanov and Spinodal Decomposition.*” *Phys. status solidi*, 248, 1765–1776, (2011).
124. A. Tabata, L. K. Teles, L. M. R. Scolfaro, J. R. Leite, A. Kharchenko, T. Frey, D. J. As, D. Schikora, K. Lischka, J. Furthmüller, and F. Bechstedt, “*Phase Separation Suppression in InGaN Epitaxial Layers Due to Biaxial Strain.*” *Appl. Phys. Lett.*, 80, 769–771, (2002).
125. I. Ho, and G. B. Stringfellow, “*Solid Phase Immiscibility in GaInN.*” *Appl. Phys. Lett.*, 69, 2701–2703, (1996).
126. K. Hiramatsu, Y. Kawaguchi, M. Shimizu, N. Sawaki, T. Zheleva, R. F. Davis, H. Tsuda, W. Taki, N. Kuwano, and K. Oki, “*The Composition Pulling Effect in MOVPE Grown InGaN on GaN and AlGaN and Its TEM Characterization.*” *MRS Internet J. Nitride Semicond. Res.*, 2, e6, (1997).
127. S. Pereira, M. R. Correia, E. Pereira, K. P. O’Donnell, C. Trager-Cowan, F. Sweeney, and E. Alves, “*Compositional pulling effects in $\text{In}_x\text{Ga}_{1-x}\text{N}/\text{GaN}$ layers: A combined depth-resolved cathodoluminescence and Rutherford backscattering/channeling study.*” *Phys. Rev. B*, 64, 205311, (2001).
128. M. Shimizu, Y. Kawaguchi, K. Hiramatsu, and N. Sawaki, “*MOVPE Growth of Thick Homogeneous InGaN Directly on Sapphire Substrate Using AlN Buffer Layer.*” *Solid. State. Electron.*, 41, 145–147, (1997).
129. Y. Kawaguchi, M. Shimizu, M. Yamaguchi, K. Hiramatsu, N. Sawaki, W. Taki, H. Tsuda, N. Kuwano, K. Oki, T. Zheleva, and R. Davis, “*The Formation of Crystalline Defects and Crystal Growth Mechanism in $\text{In}_x\text{Ga}_{1-x}\text{N}/\text{GaN}$ Heterostructure Grown by Metalorganic Vapor Phase Epitaxy.*” *J. Cryst. Growth*, 189–190, 24–28, (1998).
130. X. Kong, S. Albert, A. Bengoechea-Encabo, M. A. Sanchez-Garcia, E. Calleja, and A. Trampert, “*Lattice Pulling Effect and Strain Relaxation in Axial (In,Ga)N/GaN Nanowire Heterostructures Grown on GaN-Buffered Si(111) Substrate.*” *Phys. status solidi*, 212, 736–739, (2015).
131. D. Doppalapudi, S. N. Basu, and T. D. Moustakas, “*Phase Separation and Ordering in InGaN Alloys.*” *MRS Proc.*, 512, 431, (1998).
132. P. Ruterana, G. Nouet, W. Van der Stricht, I. Moerman, and L. Considine, “*Chemical Ordering in Wurtzite $\text{In}_x\text{Ga}_{1-x}\text{N}$ Layers Grown on (0001) Sapphire by Metalorganic Vapor Phase Epitaxy.*” *Appl. Phys. Lett.*, 72, 1742–1744, (1998).
133. M. K. Behbehani, E. L. Piner, S. X. Liu, N. A. El-Masry, and S. M. Bedair, “*Phase Separation and Ordering Coexisting in $\text{In}_x\text{Ga}_{1-x}\text{N}$ Grown by Metal Organic Chemical Vapor Deposition.*” *Appl. Phys. Lett.*, 75, 2202–2204, (1999).

134. Z. H. Wu, Y. Kawai, Y.-Y. Fang, C. Q. Chen, H. Kondo, M. Hori, Y. Honda, M. Yamaguchi, and H. Amano, “*Spontaneous Formation of Highly Regular Superlattice Structure in InGaN Epilayers Grown by Molecular Beam Epitaxy.*” Appl. Phys. Lett., 98, 141905, (2011).
135. I. J. Fritz, M. J. Hafich, J. F. Klem, and S. A. Casalnuovo, “*Barrier-Width Dependence of Emission in Triple-Quantum-Well Broadband Light-Emitting Diodes.*” Electron. Lett., 35, 171, (1999).
136. G. T. Liu, A. Stintz, E. A. Pease, T. C. Newell, K. J. Malloy, and L. F. Lester, “*1.58-Mm Lattice-Matched and Strained Digital Alloy AlGaInAs-InP Multiple-Quantum-Well Lasers.*” IEEE Photonics Technol. Lett., 12, 4–6, (2000).
137. A. Yoshikawa, S. B. Che, W. Yamaguchi, H. Saito, X. Q. Wang, Y. Ishitani, and E. S. Hwang, “*Proposal and Achievement of Novel Structure InN/GaN Multiple Quantum Wells Consisting of 1 ML and Fractional Monolayer InN Wells Inserted in GaN Matrix.*” Appl. Phys. Lett., 90, 073101, (2007).
138. A. Yoshikawa, S. B. Che, N. Hashimoto, H. Saito, Y. Ishitani, and X. Q. Wang, “*Fabrication and Characterization of Novel Monolayer InN Quantum Wells in a GaN Matrix.*” J. Vac. Sci. Technol. B Microelectron. Nanom. Struct., 26, 1551, (2008).
139. M. S. Miao, Q. M. Yan, and C. G. Van de Walle, “*Electronic Structure of a Single-Layer InN Quantum Well in a GaN Matrix.*” Appl. Phys. Lett., 102, 102103, (2013).
140. I. Gorczyca, T. Suski, N. E. Christensen, and A. Svane, “*Band Structure and Quantum Confined Stark Effect in InN/GaN Superlattices.*” Cryst. Growth Des., 12, 3521–3525, (2012).
141. I. Gorczyca, T. Suski, N. E. Christensen, and A. Svane, “*Hydrostatic Pressure and Strain Effects in Short Period InN/GaN Superlattices.*” Appl. Phys. Lett., 101, 092104, (2012).
142. L. Zhou, E. Dimakis, R. Hathwar, T. Aoki, D. J. Smith, T. D. Moustakas, S. M. Goodnick, and M. R. McCartney, “*Measurement and Effects of Polarization Fields on One-Monolayer-Thick InN/GaN Multiple Quantum Wells.*” Phys. Rev. B, 88, 125310, (2013).
143. A. Yuki, H. Watanabe, S.-B. Che, Y. Ishitani, and A. Yoshikawa, “*1-2 ML Thick InN-Based Quantum Wells with InGaN Barriers for Blue-Green Light Emitters.*” Phys. status solidi, 6, S417–S420, (2009).
144. M. S. Miao, Q. Yan, C. G. Van de Walle, W. K. Lou, L. L. Li, and K. Chang, “*Polarization-Driven Topological Insulator Transition in a GaN/InN/GaN Quantum Well.*” Phys. Rev. Lett., 109, 186803, (2012).
145. C. Chèze, M. Siekacz, F. Isa, B. Jenichen, F. Feix, J. Buller, T. Schulz, M. Albrecht, C. Skierbiszewski, R. Calarco, R. Calarco and H. Riechert, “*Investigation of Interface Abruptness and In Content in (In,Ga)N/GaN Superlattices.*” J. Appl. Phys., 120, 125307, (2016).

- (2016).
146. G. Staszczak, I. Gorczyca, T. Suski, X. Q. Wang, N. E. Christensen, A. Svane, E. Dimakis, and T. D. Moustakas, “*Photoluminescence and Pressure Effects in Short Period InN/NGaN Superlattices.*” J. Appl. Phys., 113, 123101, (2013).
 147. E. Dimakis, A. Y. Nikiforov, C. Thomidis, L. Zhou, D. J. Smith, J. Abell, C.-K. Kao, and T. D. Moustakas, “*Growth and Properties of Near-UV Light Emitting Diodes Based on InN/GaN Quantum Wells.*” Phys. status solidi, 205, 1070–1073, (2008).
 148. C. Chèze, F. Feix, M. Anikeeva, T. Schulz, M. Albrecht, H. Riechert, O. Brandt, and R. Calarco, “*In/GaN(0001)- $(2\sqrt{3} \times 2\sqrt{3})R30^\circ$ Adsorbate Structure as a Template for Embedded (In, Ga)N/GaN Monolayers and Short-Period Superlattices.*” Appl. Phys. Lett., 110, 072104, (2017).
 149. T. Suski, T. Schulz, M. Albrecht, X. Q. Wang, I. Gorczyca, K. Skrobias, N. E. Christensen, and A. Svane, “*The Discrepancies between Theory and Experiment in the Optical Emission of Monolayer In(Ga)N Quantum Wells Revisited by Transmission Electron Microscopy.*” Appl. Phys. Lett., 104, 182103, (2014).
 150. G. P. Dimitrakopoulos, I. G. Vasileiadis, C. Bazioti, J. Smalc-Koziorowska, S. Kret, E. Dimakis, N. Florini, T. Kehagias, T. Suski, T. Karakostas, T. Moustakas, and P. Komninou, “*Compositional and Strain Analysis of In(Ga)N/GaN Short Period Superlattices.*” J. Appl. Phys., 123, 024304, (2018).
 151. A. Yoshikawa, K. Kusakabe, N. Hashimoto, E.-S. Hwang, D. Imai, and T. Itoi, “*Systematic Study on Dynamic Atomic Layer Epitaxy of InN on/in +c-GaN Matrix and Fabrication of Fine-Structure InN/GaN Quantum Wells: Role of High Growth Temperature.*” J. Appl. Phys., 120, 225303, (2016).
 152. A. Yoshikawa, K. Kusakabe, N. Hashimoto, D. Imai, and E.-S. Hwang, “*Systematic Study on Dynamic Atomic Layer Epitaxy of InN on/in +c-GaN Matrix and Fabrication of Fine-Structure InN/GaN Quantum Wells: Impact of Excess In-Atoms at High Growth Temperature.*” J. Appl. Phys., 120, 235302, (2016).
 153. J. R. Arthur, “*Interaction of Ga and As 2 Molecular Beams with GaAs Surfaces.*” J. Appl. Phys., 39, 4032–4034, (1968).
 154. A. Y. Cho, “*Epitaxy by Periodic Annealing.*” Surf. Sci., 17, 494–503, (1969).
 155. A. Y. Cho, “*Morphology of Epitaxial Growth of GaAs by a Molecular Beam Method: The Observation of Surface Structures.*” J. Appl. Phys., 41, 2780–2786, (1970).
 156. T. Mimura, S. Hiyamizu, T. Fujii, and K. Nanbu, “*A New Field-Effect Transistor with Selectively Doped GaAs/n-Al x Ga 1- x As Heterojunctions.*” Jpn. J. Appl. Phys., 19, L225–L227, (1980).

157. W. V. McLevige, H. T. Yuan, W. M. Duncan, W. R. Frensley, F. H. Doerbeck, H. Morkoc, and T. J. Drummond, “*GaAs/AlGaAs Heterojunction Bipolar Transistors for Integrated Circuit Applications.*” IEEE Electron Device Lett., 3, 43–45, (1982).
158. J. Faist, F. Capasso, D. L. Sivco, C. Sirtori, A. L. Hutchinson, and A. Y. Cho, “*Quantum Cascade Laser.*” Science, 264, 553–556, (1994).
159. B. A. Wacaser, K. A. Dick, J. Johansson, M. T. Borgström, K. Deppert, and L. Samuelson, “*Preferential Interface Nucleation: An Expansion of the VLS Growth Mechanism for Nanowires.*” Adv. Mater., 21, 153–165, (2009).
160. P. Cheyssac, M. Sacilotti, and G. Patriarche, “*Vapor-Liquid-Solid Mechanisms: Challenges for Nanosized Quantum Cluster/Dot/Wire Materials.*” J. Appl. Phys., 100, 044315, (2006).
161. D. Leonard, M. Krishnamurthy, C. M. Reaves, S. P. Denbaars, and P. M. Petroff, “*Direct Formation of Quantum-sized Dots from Uniform Coherent Islands of InGaAs on GaAs Surfaces.*” Appl. Phys. Lett., 63, 3203–3205, (1993).
162. N. Koguchi, and K. Ishige, “*Growth of GaAs Epitaxial Microcrystals on an S-Terminated GaAs Substrate by Successive Irradiation of Ga and As Molecular Beams.*” Jpn. J. Appl. Phys., 32, 2052–2058, (1993).
163. H. L. Stormer, and D. C. Tsui, “*The Fractional Quantum Hall Effect.*” Proc. Natl. Acad. Sci., 84, 4696–4697, (1987).
164. H. L. Stormer, D. C. Tsui, and A. C. Gossard, “*The Fractional Quantum Hall Effect.*” Rev. Mod. Phys., 71, S298–S305, (1999).
165. B. A. Bernevig, T. L. Hughes, and S.-C. Zhang, “*Quantum Spin Hall Effect and Topological Phase Transition in HgTe Quantum Wells.*” Science (80-.), 314, 1757–1761, (2006).
166. M. König, S. Wiedmann, C. Brune, A. Roth, H. Buhmann, L. W. Molenkamp, X.-L. Qi, and S.-C. Zhang, “*Quantum Spin Hall Insulator State in HgTe Quantum Wells.*” Science (80-.), 318, 766–770, (2007).
167. M. A. Herman, and H. Sitter, “*Molecular Beam Epitaxy;*” Springer Series in Materials Science; Springer Berlin Heidelberg: Berlin, Heidelberg, 1996; Vol. 7, pp 3–5.
168. R. A. Kubiak, S. M. Newstead, and P. Sullivan, “*The Technology and Design of Molecular Beam Epitaxy Systems.*” In *Molecular Beam Epitaxy*; Elsevier, 1995; pp 1–113.
169. S. Franchi, “*Molecular Beam Epitaxy.*” In *Molecular Beam Epitaxy, Applications to Key Materials*; Elsevier, 2013; pp 1–46.
170. J. H. Neave, P. J. Dobson, B. A. Joyce, and J. Zhang, “*Reflection High-energy Electron Diffraction Oscillations from Vicinal Surfaces—a New Approach to Surface Diffusion*

- Measurements.*” Appl. Phys. Lett., 47, 100–102, (1985).
171. C. Poblenz, P. Waltereit, and J. S. Speck, “*Uniformity and Control of Surface Morphology during Growth of GaN by Molecular Beam Epitaxy.*” J. Vac. Sci. Technol. B Microelectron. Nanom. Struct., 23, 1379, (2005).
 172. M. Moseley, D. Billingsley, W. Henderson, E. Trybus, and W. A. Doolittle, “*Transient Atomic Behavior and Surface Kinetics of GaN.*” J. Appl. Phys., 106, 014905, (2009).
 173. S. L. Chuang, and C. S. Chang, “*K_p Method for Strained Wurtzite Semiconductors.*” Phys. Rev. B, 54, 2491–2504, (1996).
 174. E. O. Kane, “*Energy Band Structure in P-Type Germanium and Silicon.*” J. Phys. Chem. Solids, 1, 82–99, (1956).
 175. P. Löwdin, “*A Note on the Quantum-Mechanical Perturbation Theory.*” J. Chem. Phys., 19, 1396–1401, (1951).
 176. L. C. Lew Yan Voon, and M. Willatzen, “*Perturbation Theory – Kane Models.*” In *The k_p Method*; Springer Berlin Heidelberg: Berlin, Heidelberg, 2009; pp 55–77.
 177. S.-L. Chuang, *Physics of Optoelectronic Devices*, 1st edition, John Wiley & Sons: New York, 1995.
 178. M. Winkelkemper, A. Schliwa, and D. Bimberg, “*Interrelation of structural and electronic properties in In_xGa_{1-x}N/GaN quantum dots using an eight-band k_p model*” Phys. Rev. B, 74, 155322, (2006).
 179. Q. Yan, P. Rinke, M. Scheffler, and C. G. Van De Walle, “*Strain Effects in Group-III Nitrides: Deformation Potentials for AlN, GaN, and InN.*” Appl. Phys. Lett., 95, (2009).
 180. M. G. Burt, “*Fundamentals of Envelope Function Theory for Electronic States and Photonic Modes in Nanostructures.*” J. Phys. Condens. Matter, 11, 53–83, (1999).
 181. M. G. Burt, “*The Justification for Applying the Effective-Mass Approximation to Microstructures.*” J. Phys. Condens. Matter, 4, 6651–6690, (1992).
 182. M. G. Burt, “*An Exact Formulation of the Envelope Function Method for the Determination of Electronic States in Semiconductor Microstructures.*” Semicond. Sci. Technol., 2, 460–462, (1987).
 183. L. C. Lew Yan Voon, and M. Willatzen, “*Heterostructures: Basic Formalism.*” In *The k_p Method*; Springer Berlin Heidelberg: Berlin, Heidelberg, 2009; pp 273–362.
 184. F. Mireles, and S. E. Ulloa, “*Ordered Hamiltonian and matching conditions for heterojunctions with wurtzite symmetry: GaN/Al_xGa_{1-x}N quantum wells.*” Phys. Rev. B, 60,

- 13659–13667, (1999).
185. E. Monroy, B. Daudin, E. Bellet-Amalric, N. Gogneau, D. Jalabert, F. Enjalbert, J. Brault, J. Barjon, and L. S. Dang, “*Surfactant Effect of In for AlGa_N Growth by Plasma-Assisted Molecular Beam Epitaxy.*” J. Appl. Phys., 93, 1550–1556, (2003).
 186. C. Adelmann, J. Brault, D. Jalabert, P. Gentile, H. Mariette, G. Mula, and B. Daudin, “*Dynamically Stable Gallium Surface Coverages during Plasma-Assisted Molecular-Beam Epitaxy of (0001) GaN.*” J. Appl. Phys., 91, 9638, (2002).
 187. A. Yoshikawa, K. Kusakabe, N. Hashimoto, E.-S. Hwang, and T. Itoi, “*Dynamic Atomic Layer Epitaxy of InN on/in +c-GaN Matrix: Effect of ‘In+N’ Coverage and Capping Timing by GaN Layer on Effective InN Thickness.*” Appl. Phys. Lett., 108, 022108, (2016).
 188. L. Lymperakis, T. Schulz, C. Freysoldt, M. Anikeeva, Z. Chen, X. Zheng, B. Shen, C. Chèze, M. Siekacz, X. Q. Wang, M. Albrecht, and J. Neugebauer, “*Elastically Frustrated Rehybridization: Origin of Chemical Order and Compositional Limits in InGa_N Quantum Wells.*” Phys. Rev. Mater., 2, 011601, (2018).
 189. C. Li, Y. Maidaniuk, A. V. Kuchuk, S. Shetty, P. Ghosh, T. P. White, T. A. Morgan, X. Hu, Y. Wu, M. E. Ware, Y. I. Mazur, and G. J. Salamo, “*Kinetically Controlled Indium Surface Coverage Effects on PAMBE-Growth of InN/GaN(0001) Quantum Well Structures.*” J. Appl. Phys., 123, 195302, (2018).
 190. A. Das, S. Magalhães, Y. Kotsar, P. K. Kandaswamy, B. Gayral, K. Lorenz, E. Alves, P. Ruterana, and E. Monroy, “*Indium Kinetics during the Plasma-Assisted Molecular Beam Epitaxy of Semipolar (11–22) InGa_N Layers.*” Appl. Phys. Lett., 96, 181907, (2010).
 191. S. Choi, T.-H. Kim, S. Wolter, A. Brown, H. O. Everitt, M. Losurdo, and G. Bruno, “*Indium Adlayer Kinetics on the Gallium Nitride (0001) Surface: Monitoring Indium Segregation and Precursor-Mediated Adsorption.*” Phys. Rev. B, 77, 115435, (2008).
 192. M. Moseley, B. Gunning, J. Greenlee, J. Lowder, G. Namkoong, and W. Alan Doolittle, “*Observation and Control of the Surface Kinetics of InGa_N for the Elimination of Phase Separation.*” J. Appl. Phys., 112, 014909, (2012).
 193. H. Chen, R. M. Feenstra, J. E. Northrup, J. Neugebauer, and D. W. Greve, “*Indium Incorporation and Surface Segregation during InGa_N Growth by Molecular Beam Epitaxy: Experiment and Theory.*” MRS Internet J. Nitride Semicond. Res., 6, e11, (2001).
 194. A. V. Kuchuk, V. P. Kladko, T. L. Petrenko, V. P. Bryksa, A. E. Belyaev, Y. I. Mazur, M. E. Ware, E. A. DeCuir, and G. J. Salamo, “*Mechanism of Strain-Influenced Quantum Well Thickness Reduction in Ga_N/Al_N Short-Period Superlattices.*” Nanotechnology, 25, 245602, (2014).
 195. S. Lee, C. Freysoldt, and J. Neugebauer, “*Ordering phenomena and formation of*

- nanostructures in $\text{In}_x\text{Ga}_{1-x}\text{N}$ layers coherently grown on $\text{GaN}(0001)$.*” Phys. Rev. B, 90, 245301, (2014).
196. P. Wolny, M. Anikeeva, M. Sawicka, T. Schulz, T. Markurt, M. Albrecht, M. Siekacz, and C. Skierbiszewski, “*Dependence of Indium Content in Monolayer-Thick InGaN Quantum Wells on Growth Temperature in $\text{In}_x\text{Ga}_{1-x}\text{N}/\text{In}_{0.02}\text{Ga}_{0.98}\text{N}$ Superlattices.*” J. Appl. Phys., 124, 065701, (2018).
 197. M. Moseley, J. Lowder, D. Billingsley, and W. A. Doolittle, “*Control of Surface Adatom Kinetics for the Growth of High-Indium Content InGaN throughout the Miscibility Gap.*” Appl. Phys. Lett., 97, 191902, (2010).
 198. I.-S. Shin, K. Wang, T. Araki, E. Yoon, and Y. Nanishi, “*New Low-Temperature Growth Method for High-Quality Low-Temperature GaN Layer by Radio-Frequency Plasma-Assisted Molecular Beam Epitaxy.*” Appl. Phys. Express, 5, 125503, (2012).
 199. T. Araki, H. Umeda, T. Yamaguchi, T. Sakamoto, E. Yoon, and Y. Nanishi, “*RF-MBE Growth of InN/InGaN MQW Structures by DERI and Their Characterization.*” In *2010 22nd International Conference on Indium Phosphide and Related Materials (IPRM)*; IEEE, 2010; pp 1–4.
 200. A. R. Smith, “*Reconstructions of $\text{GaN}(0001)$ and $(000\bar{1})$ Surfaces: Ga-Rich Metallic Structures.*” J. Vac. Sci. Technol. B Microelectron. Nanom. Struct., 16, 2242, (1998).
 201. M. Ritter, W. Ranke, and W. Weiss, “*Growth and Structure of Ultrathin FeO Films on $\text{Pt}(111)$ Studied by STM and LEED.*” Phys. Rev. B, 57, 7240–7251, (1998).
 202. C. Friedrich, A. Biermann, V. Hoffmann, M. Kneissl, N. Esser, and P. Vogt, “*Preparation and Atomic Structure of Reconstructed (0001) InGaN Surfaces.*” J. Appl. Phys., 112, 033509, (2012).
 203. K. Kusakabe, N. Hashimoto, T. Itoi, K. Wang, D. Imai, and A. Yoshikawa, “*Growth Kinetics and Structural Perfection of $(\text{InN})_1/(\text{GaN})_{1-20}$ Short-Period Superlattices on $+c$ -GaN Template in Dynamic Atomic Layer Epitaxy.*” Appl. Phys. Lett., 108, 152107, (2016).
 204. H. Chen, R. M. Feenstra, J. E. Northrup, T. Zywietz, and J. Neugebauer, “*Spontaneous Formation of Indium-Rich Nanostructures on $\text{InGaN}(0001)$ Surfaces.*” Phys. Rev. Lett., 85, 1902–1905, (2000).
 205. H. Chen, R. M. Feenstra, J. E. Northrup, T. Zywietz, J. Neugebauer, and D. W. Greve, “*Surface Structures and Growth Kinetics of $\text{InGaN}(0001)$ Grown by Molecular Beam Epitaxy.*” J. Vac. Sci. Technol. B Microelectron. Nanom. Struct., 18, 2284, (2000).
 206. Di. Ma, X. Rong, X. Zheng, W. Wang, P. Wang, T. Schulz, M. Albrecht, S. Metzner, M. Müller, O. August, F. Bertram, J. Christen, P. Jin, M. Li, J. Zhang, X. Yang, F. Xu, Z. Qin, W. Ge, B. Shen, and X. Wang, “*Exciton Emission of Quasi-2D InGaN in GaN Matrix*

- Grown by Molecular Beam Epitaxy.*” Sci. Rep., 7, 46420, (2017).
207. P. G. Moses, and C. G. Van de Walle, “*Band Bowing and Band Alignment in InGaN Alloys.*” Appl. Phys. Lett., 96, 021908, (2010).
 208. I. Vurgaftman, and J. R. Meyer, “*Band Parameters for Nitrogen-Containing Semiconductors.*” J. Appl. Phys., 94, 3675–3696, (2003).
 209. A. D. Andreev, and E. P. O’Reilly, “*Theory of the Electronic Structure of GaN/AlN Hexagonal Quantum Dots.*” Phys. Rev. B, 62, 15851–15870, (2000).
 210. P. G. Moses, M. Miao, Q. Yan, and C. G. Van de Walle, “*Hybrid Functional Investigations of Band Gaps and Band Alignments for AlN, GaN, InN, and InGaN.*” J. Chem. Phys., 134, 084703, (2011).

Appendix A: Parameters for the eight-band k.p method

The eight-band **k.p** Hamiltonian is summarized in a matrix form

$$\begin{pmatrix} E_c & -\frac{\hat{k}_+ P_2}{\sqrt{2}} & \frac{\hat{k}_- P_2}{\sqrt{2}} & \hat{k}_z P_1 & 0 & 0 & 0 & 0 \\ -\frac{P_2 \hat{k}_-}{\sqrt{2}} & F & W & U & 0 & 0 & 0 & 0 \\ \frac{P_2 \hat{k}_+}{\sqrt{2}} & W^\dagger & G & V & 0 & 0 & 0 & \sqrt{2}\Delta_3 \\ P_1 \hat{k}_z & U^\dagger & V^\dagger & \Lambda & 0 & 0 & \sqrt{2}\Delta_3 & 0 \\ 0 & 0 & 0 & 0 & E_c & \frac{\hat{k}_- P_2}{\sqrt{2}} & -\frac{\hat{k}_+ P_2}{\sqrt{2}} & \hat{k}_z P_1 \\ 0 & 0 & 0 & 0 & \frac{P_2 \hat{k}_+}{\sqrt{2}} & F & W^\dagger & V \\ 0 & 0 & 0 & \sqrt{2}\Delta_3 & -\frac{P_2 \hat{k}_-}{\sqrt{2}} & W & G & U \\ 0 & 0 & \sqrt{2}\Delta_3 & 0 & P_1 \hat{k}_z & V^\dagger & U^\dagger & \Lambda \end{pmatrix}$$

where $\hat{k}_\pm = \hat{k}_x \pm i\hat{k}_y$. For quantum wells grown along the z directions

$$\begin{cases} \hat{k}_x = -i \frac{\partial}{\partial x} \rightarrow k_x \\ \hat{k}_y = -i \frac{\partial}{\partial y} \rightarrow k_y \\ \hat{k}_z = -i \frac{\partial}{\partial z} \end{cases}$$

The entries are defined as

$$\begin{aligned} E_c &= E_v + E_g + \Delta_1 + \Delta_2 + A_{cT}(k_x^2 + k_y^2) - \frac{\partial}{\partial z} A_{cZ} \frac{\partial}{\partial z} + AcS \\ F &= E_v + \Delta_1 + \Delta_2 + \frac{\hbar^2}{2m_0}(\tilde{A}_2 + \tilde{A}_4)k_x^2 + \frac{\hbar^2}{2m_0}(\tilde{A}_2 + \tilde{A}_4)k_y^2 - \frac{\hbar^2}{2m_0} \frac{\partial}{\partial z}(\tilde{A}_1 + \tilde{A}_3) \frac{\partial}{\partial z} + HS \\ G &= E_v + \Delta_1 - \Delta_2 + \frac{\hbar^2}{2m_0}(\tilde{A}_2 + \tilde{A}_4)k_x^2 + \frac{\hbar^2}{2m_0}(\tilde{A}_2 + \tilde{A}_4)k_y^2 - \frac{\hbar^2}{2m_0} \frac{\partial}{\partial z}(\tilde{A}_1 + \tilde{A}_3) \frac{\partial}{\partial z} + HS \end{aligned}$$

$$\begin{aligned}
\Lambda &= E_v + \frac{\hbar^2}{2m_0} \tilde{A}_2 k_x^2 + \frac{\hbar^2}{2m_0} \tilde{A}_2 k_y^2 - \frac{\hbar^2}{2m_0} \frac{\partial}{\partial z} \tilde{A}_1 \frac{\partial}{\partial z} + PS \\
W &= -\frac{\hbar^2}{2m_0} \tilde{A}_5 k_-^2; \quad W^\dagger = -\frac{\hbar^2}{2m_0} \tilde{A}_5 k_+^2 \\
U &= \frac{\hbar^2}{2m_0} \frac{ik_-}{\sqrt{2}} (N_2 \frac{\partial}{\partial z} + \frac{\partial}{\partial z} N'_2); \quad U^\dagger = \frac{\hbar^2}{2m_0} \frac{ik_+}{\sqrt{2}} (\frac{\partial}{\partial z} N_2 + N'_2 \frac{\partial}{\partial z}) \\
V &= \frac{\hbar^2}{2m_0} \frac{-ik_+}{\sqrt{2}} (N_2 \frac{\partial}{\partial z} + \frac{\partial}{\partial z} N'_2); \quad V^\dagger = \frac{\hbar^2}{2m_0} \frac{-ik_-}{\sqrt{2}} (\frac{\partial}{\partial z} N_2 + N'_2 \frac{\partial}{\partial z}) \\
N_2 &= 1 - \tilde{A}_1 - \tilde{A}_3 + \sqrt{2} \tilde{A}_6 \\
N'_2 &= -1 + \tilde{A}_1 + \tilde{A}_3 \\
\Delta_1 &= \Delta_{cr}; \quad \Delta_2 = \Delta_3 = \Delta_{so} / 3 \\
AcS &= a_{cz} \varepsilon_{zz} + a_{ct} (\varepsilon_{xx} + \varepsilon_{yy}) \\
PS &= D_1 \varepsilon_{zz} + D_2 (\varepsilon_{xx} + \varepsilon_{yy}) \\
QS &= D_3 \varepsilon_{zz} + D_4 (\varepsilon_{xx} + \varepsilon_{yy}) \\
HS &= PS + QS
\end{aligned}$$

where P_1 and P_2 are evaluated from the energy dispersion around $\mathbf{k} = 0$ ¹⁷³

$$\begin{aligned}
P_1^2 &= \frac{\hbar^2}{2m_0} \left(\frac{m_0}{m_e^z} - 1 \right) \frac{(E_g + \Delta_1 + \Delta_2)(E_g + 2\Delta_2) - 2\Delta_3^2}{E_g + 2\Delta_2} \\
P_2^2 &= \frac{\hbar^2}{2m_0} \left(\frac{m_0}{m_e^t} - 1 \right) \frac{E_g [(E_g + \Delta_1 + \Delta_2)(E_g + 2\Delta_2) - 2\Delta_3^2]}{(E_g + \Delta_1 + \Delta_2)(E_g + \Delta_2) - \Delta_3^2}
\end{aligned}$$

The 8×8 parameters \tilde{A}_m and the 6×6 parameters A_m are related by^{144,209}

$$\begin{aligned}
A_{cT} &= \frac{\hbar^2}{2m_0} \left(\frac{m_0}{m_e^t} - \frac{2m_0}{\hbar^2} \frac{P_2^2}{E_g} \right); \quad A_{cZ} = \frac{\hbar^2}{2m_0} \left(\frac{m_0}{m_e^z} - \frac{2m_0}{\hbar^2} \frac{P_1^2}{E_g} \right) \\
\tilde{A}_1 &= A_1 + \frac{2m_0}{\hbar^2} \frac{P_2^2}{E_g}; \quad \tilde{A}_2 = A_2 \\
\tilde{A}_3 &= A_3 - \frac{2m_0}{\hbar^2} \frac{P_2^2}{E_g}; \quad \tilde{A}_4 = A_4 + \frac{2m_0}{\hbar^2} \frac{P_1^2}{2E_g} \\
\tilde{A}_5 &= A_5 + \frac{2m_0}{\hbar^2} \frac{P_1^2}{2E_g}; \quad \tilde{A}_6 = A_6 + \frac{2m_0}{\hbar^2} \frac{P_1 P_2}{\sqrt{2} E_g}
\end{aligned}$$

Parameters used in calculation.^{144,207,208,210}

Parameters	GaN	InN
a (nm)	0.3189	0.3545
c (nm)	0.5186	0.5703
C_{13} (GPa)	106	92
C_{33} (GPa)	398	224
E_g (eV)	3.51	0.69
Valence Band offset (eV)	0	0.62
Δ_{cr} (eV)	0.01	0.04
Δ_{so} (eV)	0.017	0.005
m_e^t / m_0	0.2	0.07
m_e^z / m_0	0.2	0.07
A_1	-7.21	-8.21
A_2	-0.44	-0.68
A_3	6.68	7.57
A_4	-3.46	-5.23
A_5	-3.4	-5.11
A_6	-4.9	-5.96
$a_{cz} - D_1$ (eV)	-4.9	-3.5
$a_{ct} - D_2$ (eV)	-11.3	-3.5
D_1 (eV)	-3.7	-3.7
D_2 (eV)	4.5	4.5
D_3 (eV)	8.2	8.2
D_4 (eV)	-4.1	-4.1

Appendix B: Description of research for popular publication

Arranging atoms layer by layer

By Chen Li

Materials are merely combinations of different atoms, which are the smallest building blocks of our world unless you are a nuclear scientist. The ultimate dream for a scientist is being able to control atoms at will, through which awesome materials can be created.

Molecular beam epitaxy (MBE) is one of the most powerful tools to control atoms. It is able to put atoms down literally layer by layer and create hybrid materials that cannot be found in nature. In this particular research, we are trying to sandwich a single layer of pure indium atoms into a GaN crystal. By doing so it is expected that very bright green and red light emitters can be created. A good analogy of this task is embedding a layer of green bricks into a red brick wall. This job seems easy. Let's say the brick wall is ten layers high and we want the fifth layer to be green. We first need to build a four-layer high wall using red bricks, then put a single layer green bricks, and, finally build a five-layer high wall on top of the green brick layer.

In microscopic world things behave a little differently. First, the green bricks may fly away if the temperature is high. In other words, if the green brick layer is not covered by red bricks in time, it would eventually be gone. Secondly, even being covered immediately, these green bricks can still exchange position with red bricks in the neighboring layers. Therefore, two consequences may be expected. The first one is that we may never obtain a pure green brick layer. Instead, the fifth layer is always a mixture of green and red bricks and some green bricks are dispersed in the adjacent layers. The second one is that the final look is related to the way you cover the green layer. For example, if you can cover the green layer faster more green bricks can be preserved in the fifth layer.

If these walls are my product to be sold to customers, I would have a serious issue of quality control. Improving the quality consistency seems to require extreme attention during production, which is surely a painful thing. Fortunately, the final looks of the wall shows a self-regulating behavior. To be more specific, if there were initially more than two green brick layers, instead of exactly one, on the fourth red brick layer, the final look of the wall is going to be independent of how you cap it with red bricks.

For the real material growth, although the hope of inserting a pure indium layer into a GaN lattice needs to be given up, we can obtain a different structure, which emits blue light instead of green or red light, in a highly repeatable manner. This new structure has a thickness of two atomic layers in which the percentage of indium atoms is about 33%. If this new structure is used in mass production of blue light emitters, the easy growth process control due to the self-regulating behavior is going to improve the final product yield and thus reduce the cost.

Appendix C: Executive summary of newly created intellectual property

The following list of new intellectual property items were created in the course of this research project.

1. Developed a growth process monitoring technique based on RHEED for MBE growth of In-containing nitride materials.
2. The indium adsorption/desorption kinetics at high growth temperature corresponding to the real InN/GaN MQW growth scenario were understood.
3. The parameter space for successful InN/GaN multiple quantum well insertion was identified.

Appendix D: Potential patent and commercialization aspects of listed intellectual property items

D.1. Patentability of intellectual property

- 1) The growth process monitoring technique based on RHEED developed in this study is an incremental application of knowledge that is already well known to the science community. Therefore, it is not qualified for patent.
- 2) The understanding of the indium adsorption/desorption kinetics is an observation of physical phenomenon, which cannot be directly patented.
- 3) The identification of the parameter space for MBE growth of InN/GaN MQWs is a contribution to fundamental science, which cannot be directly patented.

D.2. Commercialization prospects

The study presented in this dissertation was intended to explore the possibility of using InN/GaN MQWs to replace highly commercialized InGaN random alloys. It was hoped that these digital alloys can outperform random InGaN alloys when used as green or red light emitters. However, this research showed that the self-regulated In content and quantum well thickness limit the usage of these MQWs in the blue to UV spectral region. Therefore, the InN/GaN MQWs cannot compete with traditional random InGaN materials and are not suitable for commercialization.

D.3. Possible prior disclosure of IP

The study of high temperature growth of InN/GaN MQWs has been published on a peer reviewed journal:

C. Li, Y. Maidaniuk, A. V. Kuchuk, S. Shetty, P. Ghosh, T. P. White, T. A. Morgan, X. Hu, Y. Wu, M. E. Ware, Y. I. Mazur, and G. J. Salamo, “*Kinetically controlled indium surface coverage effects on PAMBE-growth of InN/GaN(0001) quantum well structures*,” J. Appl. Phys., 123, 195302, (2018)

Appendix E: Broader impact of research

E.1. Applicability of research methods to other problems

The growth process monitoring technique developed in this research can be applied to general nitride MBE material growth. A special feature of nitride material growth is that sometimes it is necessary to maintain liquid-like adlayers and droplets on the growth front. A great deal of effort in this dissertation was devoted to associate the RHEED intensity transient features with the adsorption, desorption, and consumption of adlayers/droplets of one or more metal species. The new understanding widens the usability of RHEED as an in situ growth monitoring tool.

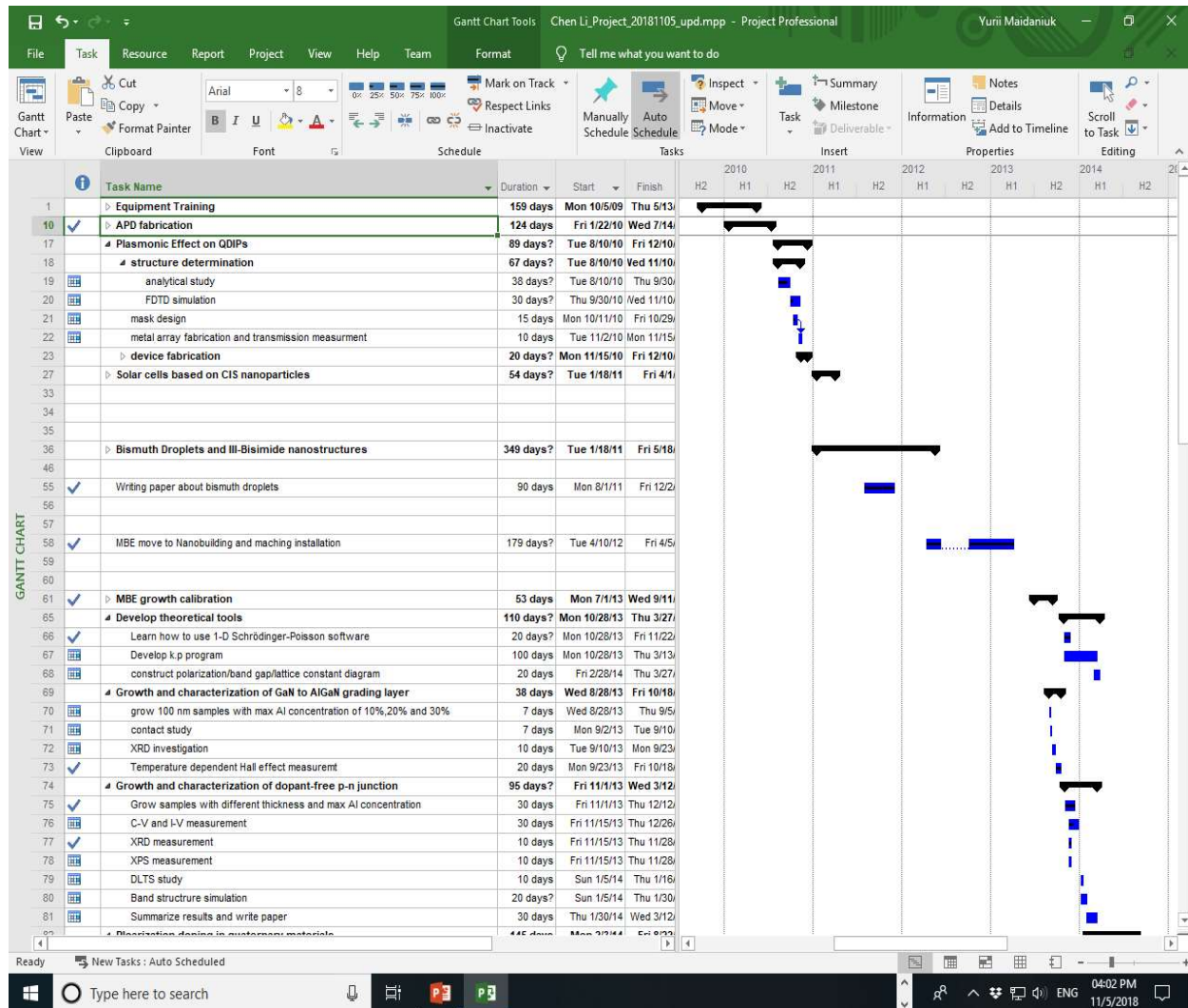
E.2. Impact of research results on U.S. and global society

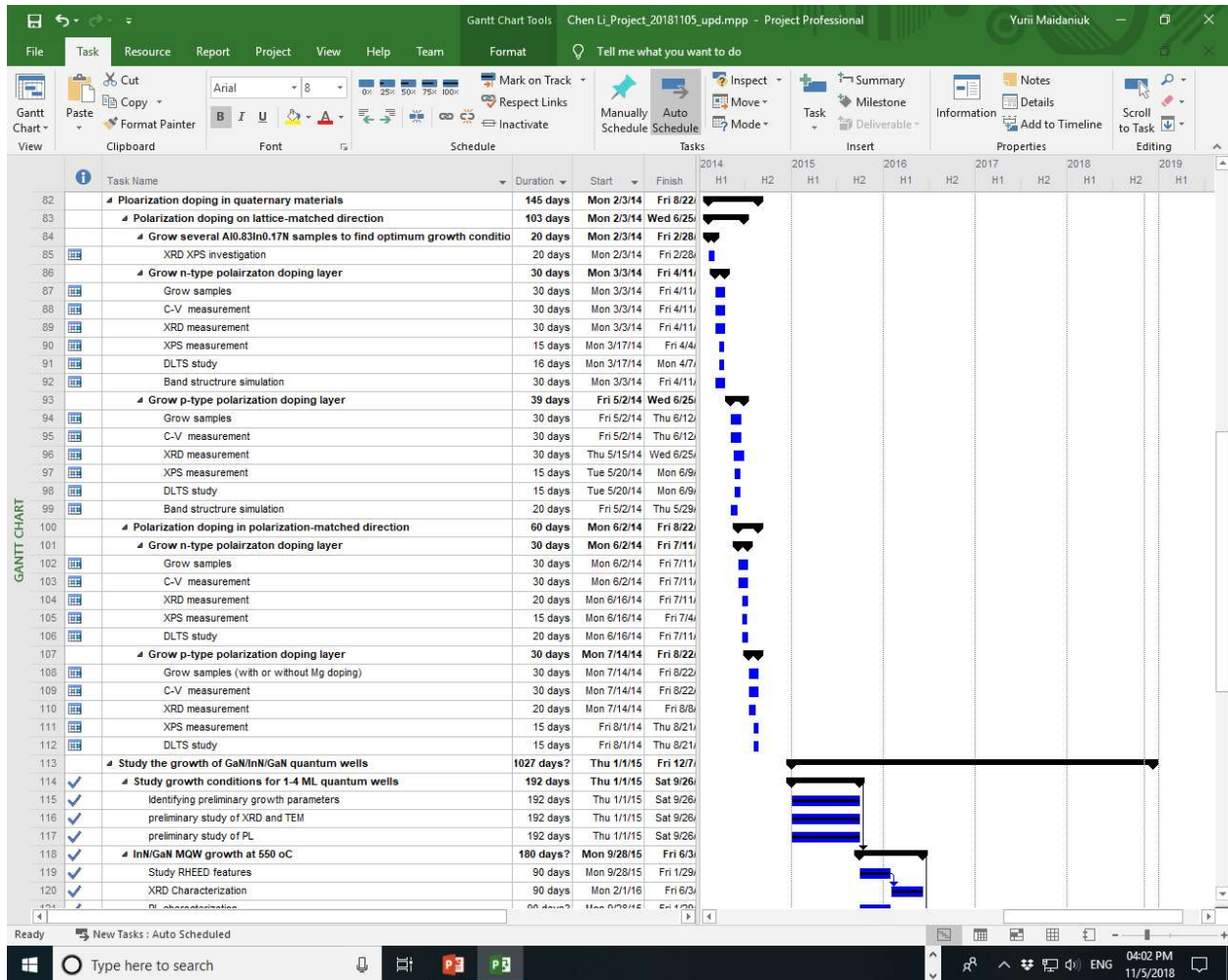
There is no immediate impact on the U.S. and global society. In a long term, the scientific understanding contributed in this research may lead to the improvement of InGaN material quality so that many long-awaited high performance InGaN-based devices, such as the high efficiency multijunction solar cells, can be one day created. These devices could lead to many new industries, which would benefit not only the U.S. but also the whole world.

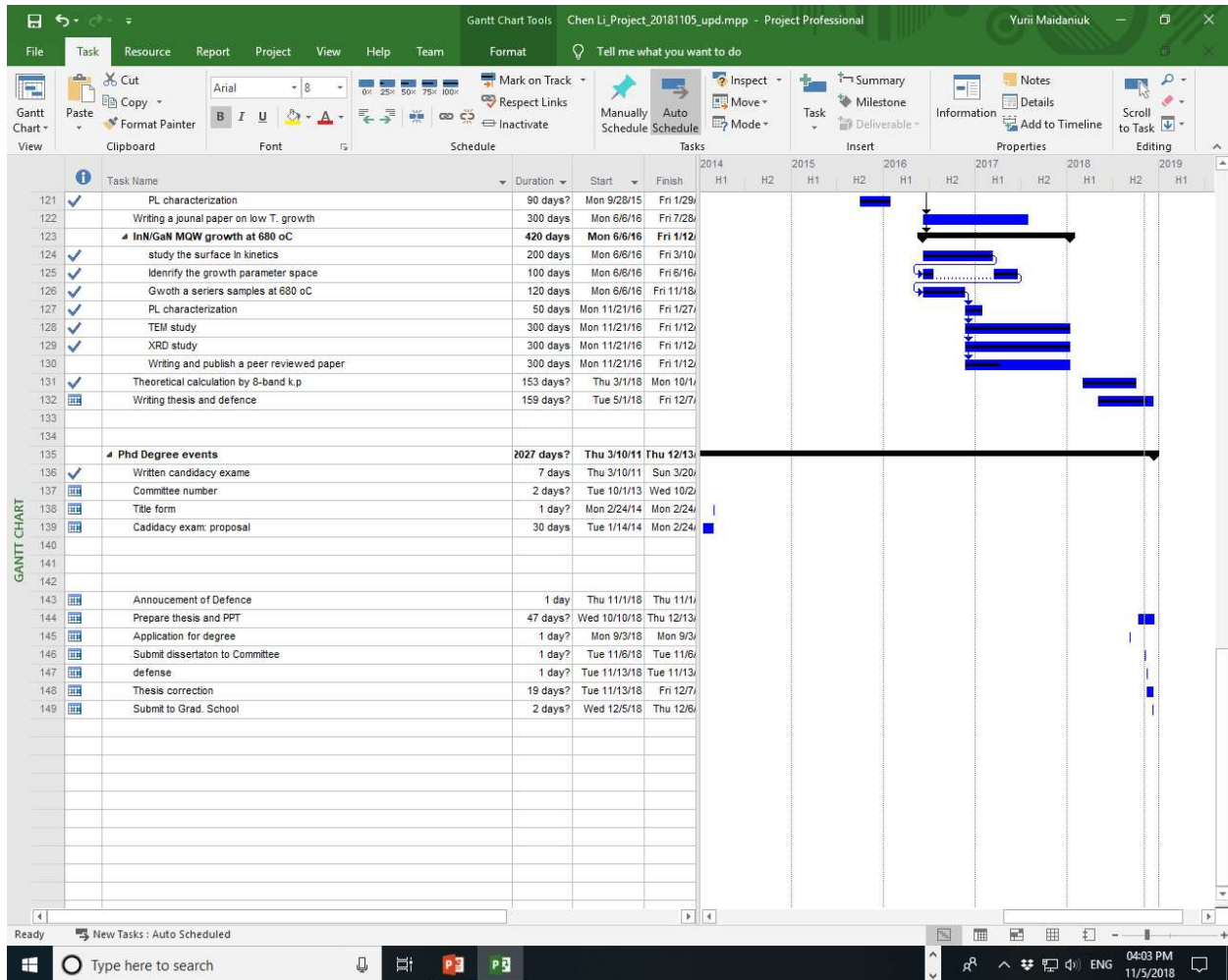
E.3. Impact of research results on the environment

The nitride semiconductors are well known for their chemical stability. They virtually do not react with any substance at normal environmental temperatures. Therefore, the waste of nitride materials would not be a concern for environment. Further, the band gap of InGaN materials covers the whole solar spectrum and, therefore, is especially suitable for high-efficiency solar energy harvesting. If the material quality can be improved in the future, it can be expected that the wide use of InGaN-based solar cells will greatly reduce the consumption of fossil fuel and improve the air quality.

Appendix F: Microsoft project for Ph.D. microEP degree plan







Appendix G: Identification of all software used in research and dissertation generation

Computer 1

Model No.: Dell XPS 8300

Serial No.: C55KHQ1

Location: Nano. 301

Owner: Chen Li

Software 1: Windows 10, purchased by Chen Li

Software 2: Microsoft office 2016, purchased by University of Arkansas site license

Software 3: Matlab R2014a, purchased by Chen Li

Software 4: Photoshop CS 5, purchased by Chen Li

Computer 2

Model No.: Lenovo Y 470

Serial No.: CB01121006

Location: Nano. 301

Owner: Chen Li

Software 1: Windows 10, purchased by Chen Li

Software 2: Microsoft office 2016, purchased by University of Arkansas site license

Software 3: Origin student 2018, purchased by Chen Li

Appendix H: All publications published, submitted, and planned

Journal papers:

1. **C. Li**, Y. Maidaniuk, A. V. Kuchuk, S. Shetty, P. Ghosh, T. P. White, T. A. Morgan, X. Hu, Y. Wu, M. E. Ware, Y. I. Mazur, and G. J. Salamo, “*Kinetically controlled indium surface coverage effects on PAMBE-growth of InN/GaN(0001) quantum well structures*,” J. Appl. Phys., 123, 195302, (2018).
2. **C. Li**, Z. Q. Zeng, D. S. Fan, Y. Hirono, J. Wu, T. A. Morgan, X. Hu, S. Q. Yu, Z. M. Wang, and G. J. Salamo, “*Bismuth nano-droplets for group-V based molecular-beam droplet epitaxy*,” Appl. Phys. Lett., 99, 243113, (2011).
3. P. K. Ghosh, M. Sarollahi, **C. Li**, T. White, D. T. Debu, Q. Yan, A. Kuchuk, R. Kumar, S. Shetty, G. J. Salamo, and M. E. Ware, “*High temperature capacitors using AlN grown by MBE as the dielectric*,” J. Vac. Sci. Technol. B, 36, 041202, (2018).
4. P. M. Lytvyn, A. V. Kuchuk, Y. I. Mazur, **C. Li**, M. E. Ware, Z. M. Wang, V. P. Kladko, A. E. Belyaev, and G. J. Salamo, “*Polarization Effects in Graded AlGa_N Nanolayers Revealed by Current-Sensing and Kelvin Probe Microscopy*,” ACS Appl. Mater. Interfaces, 10, 6755–6763, (2018).
5. A. V. Kuchuk, P. M. Lytvyn, **C. Li**, H. V. Stanchu, Y. I. Mazur, M. E. Ware, M. Benamara, R. Ratajczak, V. Dorogan, V. P. Kladko, A. E. Belyaev, and G. J. Salamo, “*Nanoscale Electrostructural Characterization of Compositionally Graded Al_xGa_{1-x}N Heterostructures on GaN/Sapphire (0001) Substrate*,” ACS Appl. Mater. Interfaces, 7, 23320–23327, (2015).
6. A. V. Kuchuk, H. V. Stanchu, **C. Li**, M. E. Ware, Y. I. Mazur, V. P. Kladko, A. E. Belyaev, and G. J. Salamo, “*Measuring the depth profiles of strain/composition in AlGa_N-graded layer by high-resolution x-ray diffraction*,” J. Appl. Phys., 116, 224302, (2014).
7. D. Fan, P. C. Grant, S.-Q. Yu, V. G. Dorogan, X. Hu, Z. Zeng, **C. Li**, M. E. Hawkrige, M. Benamara, Y. I. Mazur, G. J. Salamo, S. R. Johnson, and Z. M. Wang, “*MBE grown GaAsBi/GaAs double quantum well separate confinement heterostructures*,” J. Vac. Sci. Technol. B, Nanotechnol. Microelectron. Mater. Process. Meas. Phenom., 31, 03C105, (2013).
8. D. Fan, Z. Zeng, V. G. Dorogan, Y. Hirono, **C. Li**, Y. I. Mazur, S. Q. Yu, S. R. Johnson, Z. M. Wang, and G. J. Salamo, “*Bismuth surfactant mediated growth of InAs quantum dots by molecular beam epitaxy*,” J. Mater. Sci. Mater. Electron., 24, 1635–1639, (2013).
9. Z. Zeng, T. A. Morgan, D. Fan, **C. Li**, Y. Hirono, X. Hu, Y. Zhao, J. S. Lee, J. Wang, Z. M. Wang, S. Yu, M. E. Hawkrige, M. Benamara, and G. J. Salamo, “*Molecular beam epitaxial growth of Bi₂Te₃ and Sb₂Te₃ topological insulators on GaAs (111) substrates: a potential route to fabricate topological insulator p-n junction*,” AIP Adv., 3, 072112, (2013).

10. D. Fan, Z. Zeng, X. Hu, V. G. Dorogan, **C. Li**, M. Benamara, M. E. Hawkrige, Y. I. Mazur, S. Q. Yu, S. R. Johnson, Z. M. Wang, and G. J. Salamo, “*Molecular beam epitaxy growth of GaAsBi/GaAs/AlGaAs separate confinement heterostructures*,” Appl. Phys. Lett., 101, 181103, (2012).
11. L. Han, Y. Jiang, J.-S. Yu, W. Li, P. Hao, and **C. Li**, “Characterization of novel nonlinear optical polymeric film fabricated from dye doped PMMA,” in Proc. SPIE, 2007, 67221T.

Conferences:

1. **C. Li**, Z.Q. Zeng, D. S. Fan, Y. Hirono, J. Wu, T. A. Morgan, X. Hu, S. Q. Yu, Z. M. Wang and G. J. Salamo, “*Nanostructures induced by bismuth nano-droplets using molecular beam epitaxy*,” 4th International Workshop on Bismuth-Containing Semiconductors (4th BCS), Fayetteville, A.R., USA, Jul. 14-17(2013)
2. D. Fan, Z. Zeng, X. Hu, V. G. Dorogan, Y. Hirono, **C. Li**, P. C. Grant, M. Benamara, M. Hawkrige, Y. I. Mazur, S. Q. Yu, S. R. Johnson, Z. M. Wang and G. J. Salamo, “*High optical quality GaAsBi/GaAs/AlGaAs separate confinement heterostructures*,” 17th International Conference on Molecular Beam Epitaxy (MBE 2012), Nara, Japan, Sep. 23-28(2012)
3. D. Fan, Z. Zeng, X. Hu, V. G. Dorogan, Y. Hirono, **C. Li**, P. C. Grant, M. Benamara, M. E. Hawkrige, Y. I. Mazur, S. Q. Yu, S. R. Johnson, Z. M. Wang and G. J. Salamo, “*Molecular beam epitaxy growth of GaAsBi/GaAs/AlGaAs separate confinement heterostructures*,” 3rd International Workshop on Bismuth-Containing Semiconductors (3rd BCS), Victoria B.C., Canada, Jul.15-18(2012)
4. D. Fan, P. C. Grant, Z. Zeng, X. Hu, **C. Li**, V. G. Dorogan, M. E. Hawkrige, Y. I. Mazur, S. Q. Yu, S. R. Johnson, Z. M. Wang and G. J. Salamo, “*GaAsBi/GaAs multiple quantum wells grown by Molecular beam epitaxy*,” 29th North American Molecular Beam Epitaxy Conference (NAMBE), Atlanta, G.A., USA, Oct.14-17(2012)
5. Z. Zeng, **C. Li**, D. Fan, Y. Hirono, T. A. Morgan, X. Hu, J. Wang, J. S. Lee, Z. M. Wang, S. Q. Yu, A. Guo, and G. J. Salamo, “*Fabrication of Bi₂Te₃ nanodots by droplet epitaxy on GaAs substrates*,” APS(2012)
6. D. Fan, Z. Zeng, V. G. Dorogan, Y. Hirono, **C. Li**, Y. I. Mazur, Z. M. Wang, S. R. Johnson, S. Q. Yu, G. J. Salamo, “*Photoluminescence and surface morphology characterization of GaAsBi Grown on GaAs*,” 28th North American Molecular Beam Epitaxy Conference, San Diego(2011)
7. Z. Zeng, D. Fan, **C. Li**, Y. Hirono, T. A. Morgan, Z. M. Wang, S. Q. Yu, A. Guo, G. J. Salamo, “*Epitaxial Growth of High high-quality Bi₂Te₃ and Sb₂Te₃ thin films on GaAs(111)*,” MRS fall meeting, Boston(2011)
8. D. Fan, Z. Zeng, V. G. Dorogan, Y. Hirono, **C. Li**, Y. I. Mazur, Z. M. Wang, S. R. Johnson,

S. Q. Yu and G. J. Salamo, "*Bismuth surfactant mediated growth of InAs quantum dots by Molecular Beam Epitaxy*," MRS fall meeting, Boston(2011)

Appendix I: Publishing agreements/permissions

12/6/2018

RightsLink Printable License

AIP PUBLISHING LICENSE TERMS AND CONDITIONS

Dec 06, 2018

This Agreement between Chen Li ("You") and AIP Publishing ("AIP Publishing") consists of your license details and the terms and conditions provided by AIP Publishing and Copyright Clearance Center.

License Number	4483290201111
License date	Dec 06, 2018
Licensed Content Publisher	AIP Publishing
Licensed Content Publication	Journal of Applied Physics
Licensed Content Title	Kinetically controlled indium surface coverage effects on PAMBE-growth of InN/GaN(0001) quantum well structures
Licensed Content Author	Chen Li, Yuri Maidaniuk, Andrian V. Kuchuk, et al
Licensed Content Date	May 21, 2018
Licensed Content Volume	123
Licensed Content Issue	19
Type of Use	Thesis/Dissertation
Requestor type	Author (original article)
Format	Print and electronic
Portion	Excerpt (> 800 words)
Will you be translating?	No
Title of your thesis / dissertation	Growth and Behaviors of InN/GaN Multiple Quantum Wells by Plasma-Assisted Molecular Beam Epitaxy
Expected completion date	Dec 2018
Estimated size (number of pages)	100
Requestor Location	Chen Li 735 W Treadwell St., Apt 34 FAYETTEVILLE, AR 72701 United States Attn: Chen Li
Billing Type	Invoice
Billing Address	Chen Li 735 W Treadwell St., Apt 34 FAYETTEVILLE, AR 72701 United States Attn: Chen Li
Total	0.00 USD

Terms and Conditions

AIP Publishing -- Terms and Conditions: Permissions Uses

AIP Publishing hereby grants to you the non-exclusive right and license to use and/or distribute
<https://s100.copyright.com/AppDispatchServlet>

1/2

the Material according to the use specified in your order, on a one-time basis, for the specified term, with a maximum distribution equal to the number that you have ordered. Any links or other content accompanying the Material are not the subject of this license.

1. You agree to include the following copyright and permission notice with the reproduction of the Material: "Reprinted from [FULL CITATION], with the permission of AIP Publishing." For an article, the credit line and permission notice must be printed on the first page of the article or book chapter. For photographs, covers, or tables, the notice may appear with the Material, in a footnote, or in the reference list.
2. If you have licensed reuse of a figure, photograph, cover, or table, it is your responsibility to ensure that the material is original to AIP Publishing and does not contain the copyright of another entity, and that the copyright notice of the figure, photograph, cover, or table does not indicate that it was reprinted by AIP Publishing, with permission, from another source. Under no circumstances does AIP Publishing purport or intend to grant permission to reuse material to which it does not hold appropriate rights.
You may not alter or modify the Material in any manner. You may translate the Material into another language only if you have licensed translation rights. You may not use the Material for promotional purposes.
3. The foregoing license shall not take effect unless and until AIP Publishing or its agent, Copyright Clearance Center, receives the Payment in accordance with Copyright Clearance Center Billing and Payment Terms and Conditions, which are incorporated herein by reference.
4. AIP Publishing or Copyright Clearance Center may, within two business days of granting this license, revoke the license for any reason whatsoever, with a full refund payable to you. Should you violate the terms of this license at any time, AIP Publishing, or Copyright Clearance Center may revoke the license with no refund to you. Notice of such revocation will be made using the contact information provided by you. Failure to receive such notice will not nullify the revocation.
5. AIP Publishing makes no representations or warranties with respect to the Material. You agree to indemnify and hold harmless AIP Publishing, and their officers, directors, employees or agents from and against any and all claims arising out of your use of the Material other than as specifically authorized herein.
6. The permission granted herein is personal to you and is not transferable or assignable without the prior written permission of AIP Publishing. This license may not be amended except in a writing signed by the party to be charged.
7. If purchase orders, acknowledgments or check endorsements are issued on any forms containing terms and conditions which are inconsistent with these provisions, such inconsistent terms and conditions shall be of no force and effect. This document, including the CCC Billing and Payment Terms and Conditions, shall be the entire agreement between the parties relating to the subject matter hereof.

This Agreement shall be governed by and construed in accordance with the laws of the State of New York. Both parties hereby submit to the jurisdiction of the courts of New York County for purposes of resolving any disputes that may arise hereunder.

V1.2

Questions? customercare@copyright.com or +1-855-239-3415 (toll free in the US) or +1-978-646-2777.